

ISSN 2312-4334

MINISTRY OF EDUCATION AND SCIENCE OF UKRAINE

East European Journal of Physics

No 3. 2022

2022

East European Journal of Physics

EEJP is an international peer-reviewed journal devoted to experimental and theoretical research on the nuclear physics, cosmic rays and particles, high-energy physics, solid state physics, plasma physics, physics of charged particle beams, plasma electronics, radiation materials science, physics of thin films, condensed matter physics, functional materials and coatings, medical physics and physical technologies in an interdisciplinary context.

Published quarterly in hard copy and online by V.N. Karazin Kharkiv National University Publishing
ISSN 2312-4334 (Print), ISSN 2312-4539 (Online)

The editorial policy is to maintain the quality of published papers at the highest level by strict peer review.

Approved for publication by the Academic Council of the V.N. Karazin Kharkiv National University (August 29, 2022; Protocol no. 13).

EEJP registered by the order of Ministry of Education and Science of Ukraine No. 1643 of 28.12.2019, and included in the list of scientific professional editions of Ukraine (category "A", specialty: 104, 105), in which can be published results of dissertations for obtaining Ph.D. and Dr. Sci. degrees in physical and mathematical sciences.

The Journal is a part of the Web of Science Core Collection (ESCI) scientometric platform and indexed by SCOPUS.

Editor-in-Chief

☉ Azarenkov N.A., *Academician of NAS of Ukraine, Professor, V.N. Karazin Kharkiv National University, Kharkiv, Ukraine*

Deputy editor

☉ Girka I.O., *Corresponding Member of NAS of Ukraine, Professor, V.N. Karazin Kharkiv National University, Kharkiv, Ukraine*

Editorial Board

- ☉ Adamenko I.N., *Professor, V.N. Karazin Kharkiv National University, Ukraine*
- ☉ Antonov A.N., *D.Sc., Professor, Institute of Nuclear Research and Nuclear Energy, Sofia, Bulgaria*
- ☉ Barannik E.A., *D.Sc., Professor, V.N. Karazin Kharkiv National University, Ukraine*
- ☉ Beresnev V.M., *D.Sc., Professor, V.N. Karazin Kharkiv National University, Ukraine*
- ☉ Berezhnoy Yu.A., *D.Sc., Professor, V.N. Karazin Kharkiv National University, Ukraine*
- ☉ Bizyukov A.A., *D.Sc., Professor, V.N. Karazin Kharkiv National University, Ukraine*
- ☉ Bragina L.L., *D.Sc., Professor, STU "Kharkiv Polytechnic Institute", Ukraine*
- ☉ Broda B., *D.Sc., University of Lodz, Poland*
- ☉ Dragovich B.G., *D.Sc., University of Belgrade, Serbia*
- ☉ Duplij S.A., *D.Sc., Center for Information Technology (ZIV), Westfälische Wilhelms-Universität Münster, Münster, Germany*
- ☉ Garkusha I.E., *Corresponding Member of NAS of Ukraine, NSC Kharkiv Institute of Physics and Technology, Ukraine*
- ☉ Grekov D.L., *D.Sc., NSC Kharkiv Institute of Physics and Technology, Ukraine*
- ☉ Karnaukhov I.M., *Academician of NAS of Ukraine, NSC Kharkiv Institute of Physics and Technology, Ukraine*
- ☉ Korchin A.Yu., *D.Sc., NSC Kharkiv Institute of Physics and Technology, Ukraine*
- ☉ Lazurik V.T., *D.Sc., Professor, V.N. Karazin Kharkiv National University, Ukraine*
- ☉ Mel'nik V.N., *D.Sc., Institute of Radio Astronomy, Kharkiv, Ukraine*
- ☉ Merenkov N.P., *D.Sc., NSC Kharkiv Institute of Physics and Technology, Ukraine*
- ☉ Neklyudov I.M., *Academician of NAS of Ukraine, NSC Kharkiv Institute of Physics and Technology, Ukraine*
- ☉ Noterdaeme J.-M., *D.Sc., Max Planck Institute for Plasma Physics, Garching, Germany*
- ☉ Nurmagambetov A.Yu., *D.Sc., Professor, NSC Kharkiv Institute of Physics and Technology, Ukraine*
- ☉ Ostrikov K.N., *D.Sc., Plasma Nanoscience Centre Australia, Clayton, Australia*
- ☉ Peletminsky S.V., *Academician of NAS of Ukraine, NSC Kharkiv Institute of Physics and Technology, Ukraine*
- ☉ Pilipenko N.N., *D.Sc. in Technical Sciences, NSC Kharkiv Institute of Physics and Technology, Ukraine*
- ☉ Radinschi I., *D.Sc., Gheorghe Asachi Technical University, Iasi, Romania*
- ☉ Slyusarenko Yu.V., *Academician of NAS of Ukraine, NSC Kharkiv Institute of Physics and Technology, Ukraine*
- ☉ Smolyakov A.I., *University of Saskatchewan, Saskatoon, Canada*
- ☉ Shul'ga N.F., *Academician of NAS of Ukraine, NSC Kharkiv Institute of Physics and Technology, Ukraine*
- ☉ Tkachenko V.I., *D.Sc., NSC Kharkiv Institute of Physics and Technology, Ukraine*
- ☉ Yegorov M.O., *D.Sc., NSC Kharkiv Institute of Physics and Technology, Ukraine*

Executive Secretary

☉ Hirnyk S.A., *Ph.D., V.N. Karazin Kharkiv National University, Kharkiv, Ukraine*

Editorial office

Department of Physics and Technologies, V.N. Karazin Kharkiv National University
Kurchatov av., 31, office 402, Kharkiv, 61108, Ukraine

Tel: +38-057-335-18-33,

E-mail: eejp@karazin.ua,

Web-pages: <http://periodicals.karazin.ua/eejp> (Open Journal System)

Certificate of State registration No.20644-10464P, 21.02.2014

Східно-європейський фізичний журнал

Східно-європейський фізичний журнал – міжнародний рецензований журнал, присвячений експериментальним і теоретичним дослідженням ядерної фізики, космічних променів і частинок, фізики високих енергій, фізики твердого тіла, фізики плазми, фізики пучків заряджених частинок, плазмової електроніки, радіаційного матеріалознавства, фізики тонких плівок, фізики конденсованої речовини, функціональних матеріалів та покриттів, медичної фізики та фізичних технологій у міждисциплінарному контексті.

Видається щоквартально в друкованому вигляді та в Інтернеті видавництвом Харківського національного університету імені В.Н. Каразіна

ISSN 2312-4334 (Друкована версія), ISSN 2312-4539 (Онлайн)

Редакційна політика полягає у підтримуванні якості опублікованих статей на найвищому рівні шляхом суворої експертної оцінки. Схвалено до друку Вченою радою Харківський національний університет імені В.Н. Каразіна (29.08.2022 р.; Протокол № 13).

Східно-європейський фізичний журнал зареєстровано наказом Міністерства освіти і науки України № 1643 від 28.12.2019 та включено до Переліку наукових фахових видань України (категорія «А», спеціальність: 104, 105), у яких може публікуватися результати дисертацій на здобуття ступенів кандидата та доктора фізико-математичних наук.

Журнал є частиною наукометричної платформи Web of Science Core Collection (ESCI) і індексується SCOPUS.

Головний редактор

Азаренков Н.А., академік НАН України, професор, Харківський національний університет імені В.Н. Каразіна, Харків, Україна

Заступник редактора

Гірка І.О., член-кореспондент НАН України, професор, Харківський національний університет імені В.Н. Каразіна, Харків, Україна

Editorial Board

Адаменко І.Н., професор, Харківський національний університет імені В.Н. Каразіна, Україна

Антонов А.Н., д.ф.-м.н., професор, Інститут ядерних досліджень та ядерної енергії, Софія, Болгарія

Баранник Є.А., д.ф.-м.н., професор, Харківський національний університет імені В.Н. Каразіна, Україна

Береснев В.М., д.ф.-м.н., професор, Харківський національний університет імені В.Н. Каразіна, Україна

Бережной Ю.А., д.ф.-м.н., професор, Харківський національний університет імені В.Н. Каразіна, Україна

Бізюков А.А., д.ф.-м.н., професор, Харківський національний університет імені В.Н. Каразіна, Україна

Брагіна Л.Л., д.ф.-м.н., професор, ДТУ «Харківський політехнічний інститут», Україна

Брода Б., д.ф.-м.н., Лодзинський університет, Польща

Драгович Б.Г., д.ф.-м.н., Белградський університет, Сербія

Дуплій С.А., д.ф.-м.н., Центр інформаційних технологій (ZIV), Університет Мюнстера, Мюнстер, Німеччина

Гаркуша І.Є., член-кореспондент НАН України, ННЦ Харківський фізико-технічний інститут, Україна

Греков Д.Л., д.ф.-м.н., ННЦ Харківський фізико-технічний інститут, Україна

Карнаухов І.М., академік НАН України, ННЦ Харківський фізико-технічний інститут, Україна

Корчин А.Ю., д.ф.-м.н., ННЦ Харківський фізико-технічний інститут, Україна

Лазурик В.Т., д.ф.-м.н., професор, Харківський національний університет імені В.Н. Каразіна, Україна

Мельник В.Н., д.ф.-м.н., Інститут радіоастрономії, Харків, Україна

Меренков Н.П., д.ф.-м.н., ННЦ Харківський фізико-технічний інститут, Україна

Неклюдов І.М., академік НАН України, ННЦ Харківський фізико-технічний інститут, Україна

Нотердам Ж.-М., доктор наук, Інститут фізики плазми Макса Планка, Гархінг, Німеччина

Нурмагамбетов А.Ю., д.ф.-м.н., професор, ННЦ Харківський фізико-технічний інститут, Україна

Остріков К.Н., д.ф.-м.н., Центр нанонауки плазми, Австралія, Клейтон, Австралія

Пелетмінський С.В., академік НАН України, ННЦ Харківський фізико-технічний інститут, Україна

Пилипенко Н.Н., д.т.н. технічних наук, ННЦ Харківський фізико-технічний інститут, Україна

Радінський І., д.ф.-м.н., Технічний університет Георга Асачі, Ясси, Румунія

Слюсаренко Ю.В., академік НАН України, ННЦ Харківський фізико-технічний інститут, Україна

Смоляков А.І., Саскачеванський університет, Саскатун, Канада

Шульга Н.Ф., академік НАН України, ННЦ Харківський фізико-технічний інститут, Україна

Ткаченко В.І., д.ф.-м.н., ННЦ Харківський фізико-технічний інститут, Україна

Єгоров О.М., д.ф.-м.н., ННЦ Харківський фізико-технічний інститут, Україна

Відповідальний секретар

Гірник С.А., к. ф.-м.н., Харківський національний університет імені В.Н. Каразіна, Харків, Україна

Редакція

Науково-навчальний інститут «ФТФ», Харківський національний університет імені В.Н. Каразіна

пр. Курчатова, 31, офіс 402, Харків, 61108, Україна

Тел: +38-057-335-18-33,

Електронна пошта: eejp@karazin.ua,

Веб-сторінка: <http://periodicals.karazin.ua/eejp> (система журналів з відкритим доступом)

Свідоцтво про державну реєстрацію №20644-10464П від 21.02.2014р.

© Харківський національний університет імені В.Н. Каразіна, 2022

ORIGINAL ARTICLES

- On the Mechanisms of Formation of Density Cavities under Instability of Intense Langmuir Oscillations in a Plasma** 6
Volodymyr M. Kuklin
Про механізми формування каверн щільності при нестійкості інтенсивних ленгмюрівських коливань у плазмі
Володимир М. Куклін
- Superradiation of Mobile Oscillators** 14
Eugen V. Poklonskiy, Stanislav O. Totkal
Надвипромінювання рухомих осциляторів
Євгеній В. Поклонський, Станіслав О. Тоткал
- 7.379 % Power Conversion Efficiency of a Numerically Simulated Solid-State Dye-Sensitized Solar Cell with Copper (I) Thiocyanate as a Hole Conductor** 19
Eli Danladi, Muhammad Kashif, Thomas O. Daniel, Christopher U. Achem, Matthew Alpha, Michael Gyan
7,379 % ефективність перетворення потужності чисельно змодельованого твердотільного сенсбілізованого барвником сонячного елемента з тіоціанатом міді (I) як дірковим провідником
Елі Данладі, Мухаммад Кашиф, Томас О. Даніель, Кристофер У. Ачем, Метью Альфа, Майкл Г'ян
- The Study of Electronic States of Ni and ScI Molecules with Screened Kratzer Potential** 32
Etido P. Inyang, Effiong O. Obisung
Дослідження електронних станів молекул Ni і ScI з екранованим потенціалом Кратцера
Етідо П. Ін'янг, Ефйонг О. Обісунг
- Entangled Coherent States in Teleportation** 39
Shivani A. Kumar, Shefali Kanwar, Pramila Shukla
Заплутані когерентні стани в телепортації
Шивані А. Кумар, Шефалі Канвар, Праміла Шукла
- Pressure of Electromagnetic Radiation on a Thin Linear Vibrator in a Waveguide** 45
Mykola G. Kokodii, Victor O. Katrich, Sergey L. Berdnik, Mykhail V. Nesterenko, Vyacheslav O. Maslov, Ivan O. Priz
Тиск електромагнітного випромінювання на тонкий лінійний вібратор в хвилеводі
Микола Г. Кокодій, Віктор О. Катрич, Сергій Л. Бердник, Михайло В. Нестеренко, В'ячеслав О. Маслов, Іван О. Приз
- Comprehensive Assessment of Biological Substrates of Professional Sick Person Group by Chemometric and Nuclear Physical Methods** 53
Maryna F. Kozhevnikova, Volodymyr V. Levenets, Oleksandr P. Omelnyk, Andriy O. Shchur
Комплексна оцінка біологічних субстратів групи профхворих хемометричним та ядерно-фізичним методами
Марина Ф. Кожевнікова, Володимир В. Левенець, Олександр Р. Омельник, Андрій О. Щур
- Manufacturing Features and Characteristics of Uranium Dioxide Pellets for Subcritical Assembly Fuel Rods** 59
Igor A. Chernov, Anton V. Kushym, Volodymyr R. Tatarinov, Dmytro V. Kutniy
Особливості виготовлення і характеристики паливних таблеток із діоксиду урану для стрижневих твєлів підкритичної збірки
Ігор О. Чернов, Антон В. Куштим, Володимир Р. Татарінов, Дмитро В. Кутній
- Enhanced Performance of CuIn_{1-x}G_xSe₂ Solar Cell Through Optimization of Absorber and Buffer Layer Properties Using SCAPS-1D** 67
Godwin J. Ibeh, Celine O. Lawani, Jayeola O. Emmanuel, Peter O. Oyedare, Eli Danladi, Olumide O. Ige
Покращена продуктивність сонячної батареї CuIn_{1-x}G_xSe₂ завдяки оптимізації властивостей абсорбера та буферного шару за допомогою SCAPS-1D
Годвін Дж. Ібе, Селін О. Лавані, Джаєола О. Еммануель, Пітер О. Ойедаре, Елі Данладі, Олуміде О. Іге
- Slow Surface Eigenmodes Directed by the Mu-Negative Metamaterial Slab** 77
Viktor K. Galaydych, Oleksandr E. Sporov, Volodymyr P. Olefir, Mykola O. Azarenkov
Повільні поверхневі власні моди, що поширюються вздовж шару мю-негативного метаматеріалу
Віктор К. Галайдич, Олександр Є. Споров, Володимир П. Олєфір, Микола О. Азаренков
- Effect of Na Doping on Some Physical Properties of Chemically Sprayed CZTS Thin Films** 84
Noura J. Mahdi, Nabeel A. Bakr
Вплив легування Na на деякі фізичні властивості тонких плівок CZTS з хімічним напиленням
Нура Дж. Махді, Набіль А. Бакар
- Structural, Electrical and Optical Properties of Graphite Films are Drawn with Pencils of Different Hardness** 91
Serhii I. Kuryshchuk, Taras T. Kovalyuk, Ivan P. Kozziarskiy, Mykhailo M. Solovan
Структурні, електричні і оптичні властивості плівок графіту нарисованих олівцями різної твердості
Сергій І. Куришчук, Тарас Т. Ковалюк, Іван П. Козярський, Михайло М. Солован

- Bianchi Type V Tsallis Holographic Dark Energy Model with Hybrid Expansion Law** 97
Manash Pratim Das, Chandra Rekha Mahanta
Голографічна модель темної енергії біанчі типу V Tsallis з гібридним законом розширення
Манаши Пратім Дас, Чандра Рекха Маханта
- Non-Relativistic Study of Mass Spectra, and Thermal Properties of a Quarkonium System with Eckart-Hellmann Potential** 104
Etido P. Inyang, Effiong O. Obisung, Eddy S. William, Ituen B. Okon
Нерелятивістське дослідження мас-спектрів і теплових властивостей кварконієвої системи з потенціалом Екарта-Гельмана
Етідо П. Ін'янґ, Еффіонґ О. Обісунґ, Едді С. Вільям, Ітуен Б. Окон
- Multiple Docking of Fluorescent Dyes to Fibrillar Insulin** 115
Uliana Tarabara, Olga Zhytniakivska, Kateryna Vus, Valeriya Trusova, Galyna Gorbenko
Багатохромоморфний докінґ флуоресцентних барвників з фібрилярним інсуліном
Уліана Тарабара, Ольга Житняківська, Катерина Вус, Валерія Трусова, Галина Горбенко
- Calculation of the Absorbed Dose by a Borosilicate Glass Matrix and its Simulated Irradiation** 121
Volodymyr Morgunov, Serhii Sayenko, Volodymyr Shkuropatenko, Yevhenii Svitlychnyi, Olena Bereznyak, Serhii Lytovchenko, Volodymyr Chyshkala
Розрахунок поглиненої дози матрицею боросилікатного скла та її модельне опромінювання
Володимир В. Моргунов, Сергій Ю. Саєнко, Володимир А. Шкуропатенко, Євгеній О. Світличний, Олена П. Березняк, Сергій В. Литовченко, Володимир О. Чижкала
- Effects of Gravitational Field of a Topological Defect on Statistical Properties of Heavy Quark-Antiquark Systems** 129
André Aimé Atangana Likéné, Ali Zarma, Dieudonné Nga Ongodo, Jean Marie Ema'a Ema'a, Patrice Ele Abiama, Germain Hubert Ben-Bolie
Вплив гравітаційного поля на топологічний дефект на статистичні властивості важких кварк-антикваркових систем
Андре Аїме Атангана Лікене, Алі Зарма, Дьєдонне Нга Онґодо, Жан Марі Ема'а Ема'а, Патріс Еле Абіам, Жермен Юбер Бен-Болі
- Molecular Docking of Monomethine Cyanine Dyes to Lysozyme Amyloid Fibrils** 142
Olga Zhytniakivska, Uliana Tarabara, Atanas Kurutos, Kateryna Vus, Valeriya Trusova, Galyna Gorbenko
Молекулярний докінґ монометинових ціанінових барвників з амлоїдними фібрилами лізоциму
Ольга Житняківська, Уліана Тарабара, Атанас Курутос, Катерина Вус, Валерія Трусова, Галина Горбенко
- Sample Preparation for the Effective Accumulation and Detection of the Beta-Active Rn-222 Decay Products** 149
Gennadiy Onyshchenko, Ivan Yakymenko, Oleksandr Shchus, Anatoliy Lokha
Підготування проб для ефективного накопичення та реєстрації бета-активних продуктів розпаду Rn-222
Геннадій Онищенко, Іван Якименко, Олександр Щусь, Анатолій Лоха

ON THE MECHANISMS OF FORMATION OF DENSITY CAVITIES UNDER INSTABILITY OF INTENSE LANGMUIR OSCILLATIONS IN A PLASMA[†]

 Volodymyr M. Kuklin

V.N. Karazin Kharkiv National University, Kharkiv, Ukraine

Svobody Sq. 4, Kharkiv, Ukraine, 61022

E-mail: kuklinvm1@gmail.com

Received May 25, 2022; revised June 10, 2022; accepted June 20, 2022

The paper considers the instability of intense Langmuir oscillations in nonisothermal (Zakharov's model) and cold (Silin's model) 1D plasma. The main attention is paid to the formation of plasma density caverns in the hydrodynamic and hybrid (electrons are described hydrodynamically, ions are described by model particles) representations. In the hydrodynamic representation, with a small number of spectrum modes, large-scale plasma density caverns are observed, which rapidly deepen. This process is supported by the appearance of small-scale perturbations, and phase synchronization of the Langmuir waves of the instability spectrum is observed. This phase synchronization of the spectrum modes is quite capable of fulfilling the role that was previously proposed to be given exclusively to the effect of extrusion of particles from the cavity by the field. In hybrid models, in the region of consideration, ions are described by model particles, the number of which in the one-dimensional case $10^4 \div 5 \cdot 10^4$ (which in the three-dimensional case corresponds to the number of particles $10^{12} \div 10^{14}$). The initial spectrum of perturbations is very wide and rather intense, which leads to an explosive growth of perturbations in the Zakharov model and a rapid development of instability in the Silin model. In this case, in the developed instability regime, the formation of many small-scale plasma density caverns is observed. It is the presence of this small-scale modulation due to the Fermi effect that quickly forms the normal distribution of ions over velocities. In this case, the effect of particle heating due to Landau damping loses its primacy. It is shown that the caverns practically do not change their position; phase changes for the spectral components of the plasma density were not observed. Only individual small-scale caverns demonstrate dynamics similar to the development of caverns in the hydrodynamic representation.

Keywords: intense Langmuir oscillations, description models by Zakharov and Silin, small-scale slow-moving plasma density caverns, phase synchronization.

PACS: 52.35. ± g, 52.65. ± y

1. INTRODUCTION

The traditional idea of the dynamics of the development of instability of intense Langmuir oscillations (the wavelength of which was assumed to be very significant, actually infinite) was associated by many authors of publications on this topic with the idea expressed in [1] about the formation of deepening plasma density caverns filled with the field of the short-wavelength Langmuir spectrum of instability. Indeed, during the development of the instability process, one could see how the spectrum of instability was enriched with short-wavelength Langmuir oscillations. It could also be assumed that the caverns deepened as a result of phase locking of the modes of the short-wavelength spectrum of Langmuir waves. However, this synchronization mechanism itself was practically not discussed. For the reason for the deepening of the plasma density caverns was considered the process of plasma extrusion by the short-wavelength field of the Langmuir spectrum of instability.

In addition, it was assumed that, as a result of the development of instability, particle flows were formed, which took away the energy of the field due to Landau damping. Field and numerical experiments confirmed the appearance of a noticeable inhomogeneity of the plasma due to this instability and demonstrated the transfer of energy from the field to plasma particles, to a greater extent to electrons. The quasi-hydrodynamic description of the process of instability of intense Langmuir oscillations prevailing in many publications under conditions of a relatively narrow spectrum of initial perturbations demonstrated the appearance of individual rapidly deepening plasma density caverns. Moreover, as noted in [1–4], already in the three-dimensional case, the emerging regime with peaking (rapid growth of the short-wavelength Langmuir spectrum with deepening of the caverns) was even called the collapse of Langmuir waves (although the Debye screening limited the minimum size of the bottom of the caverns). Due to the difficulties in numerical simulation of quasi-hydrodynamic models of plasma description [5], they turned to the so-called hybrid description models, where electrons were still represented hydrodynamically as a continuous medium, and ions in a discrete form as particles. According to the opinion expressed by V. E. Zakharov and his colleagues (see [3]), direct modeling of the phenomena of formation of cavities in such problems by the particle method is “the most consistent.” It is clear that the number of modeling particles remained much less than the real number of ions in in two-dimensional and even more so in three-dimensional cases, although in the one-dimensional case, which is of academic interest, the number of modeling particles per unit length was already acceptable.

The use of hybrid models immediately showed the difference between the hydrodynamic description of all plasma particles and the hybrid description, where ions were represented by particles. The discrete description of ions actually

[†] Cite as: V.M. Kuklin, East Eur. J. Phys. 3, 6 (2022), <https://doi.org/10.26565/2312-4334-2022-3-01>

© V.M. Kuklin, 2022

sharply enhanced the short-wavelength spectrum of initial perturbations and, most importantly, advanced this initial spectrum into the region of perturbations up to the Debye radius of the ions.

This circumstance changed the conditions for the development of instability of intense Langmuir oscillations to such an extent that the picture of the process became different. As is known [2], in the Zakharov model for a nonisothermal plasma, where the electron thermal energy density exceeded the field energy density, the growth rate of perturbations only increased with decreasing scale. In the Silin model of a cold plasma, where the field energy density was higher than the thermal energy density of the plasma, the increment of such instability was significant for perturbations whose scale was comparable to the amplitude of electron oscillations in the field of intense Langmuir oscillations [6, 7]. In these two cases, with a large number of particles describing ions, the perturbation spectrum rapidly increased in the short-wavelength region, forming many small density caverns [8]. Moreover, in the Zakharov model, the growth of the instability spectrum occurred in an explosive manner.

In the hybrid model of Zakharov's nonisothermal plasma, the processes of formation of small-scale cavities immediately dominated, and it was impossible to observe the formation of sharpening regimes - the deepening of only a few large cavities, which was typical for the hydrodynamic description precisely because of the absence of a relatively intense short-wavelength disturbance spectrum in the initial conditions. For it is precisely the discreteness of the description of ions that generated such a wide initial spectrum in the short-wavelength region for the case of a hybrid description.

In Silin's cold plasma model, a decrease in the amplitude of intense Langmuir oscillations shifted the maximum growth rate to the short-wavelength region of the initial spectrum of perturbations with a noticeable amplitude, which arose due to the discreteness of the description of ions. However, this delay in the development of short-wave disturbances allowed the formation of several large-scale caverns. However, their refinement then occurred, and the depth of small-scale caverns turned out to be noticeably greater than in the case of nonisothermal plasma.

These processes of plasma density modulation could no longer be explained only by the displacement of plasma particles from the resulting caverns by the high-frequency Langmuir field, so one should return to consideration of phenomena of phase synchronization of waves of unstable spectra.

The presence of a significant small-scale modulation of the plasma field and density obviously led to the scattering of ions by inhomogeneities and their rapid thermalization. Not only was the transfer of energy from the field to the ions important, but also the formation of a normal energy distribution of the ions, which made it possible to speak about the temperature of the ions. In addition, "tails" appeared - groups of energetic ions, and in cold plasma the energy of such "tails" turned out to be comparable with the energy of ions within the formed normal distribution. It is clear that the role of Landau damping during ion thermalization in hybrid regimes could hardly be dominant; rather, the Fermi scattering mechanism on inhomogeneities manifested itself here [7, 9].

So, the appearance of large-scale deepening density caverns in plasma with instability of intense Langmuir oscillations in the case of describing ions by particles (or, what is the same, in the presence of a sufficiently significant and wide initial short-wavelength spectrum) apparently practically does not occur. Only at the initial stage of instability in a cold plasma can one see such structures that, after grinding, disappear among the mass of small-scale cavities. Therefore, in the presence of a wide intense initial spectrum, it is often impossible to observe peaking regimes in a few large caverns. As it turned out, Landau damping could hardly be considered the cause of ion thermalization.

The aim of this work is a detailed consideration of the process of formation of the spatial modulation of the plasma density. In addition, we will discuss the role of phase synchronization of Langmuir waves of an unstable spectrum in the formation of spatial structures - plasma density caverns. Let us also consider the conditions for the formation of large-scale deepening density caverns.

2. DESCRIPTION MODELS OF V.E. ZAKHAROV AND V.P. SILIN

Let us discuss hydrodynamical and hybrid models of Zakharov and Silin (hybrid models: electrons are represented by quasi-hydrodynamic equations, and ions are represented by particles), descriptions of the instability of intense Langmuir oscillations in plasma. These models make it possible to see the formation of the Maxwellian velocity distribution of ions and evaluate the efficiency of their heating [7, 9]. However, below we dwell on the consideration of the dynamics of plasma stratification - on the formation of its density caverns.

Let us first consider the case of parametric instability of an external long-wavelength Langmuir field of high intensity for a cold plasma, that is, under conditions when the energy density of the field exceeds the density of the thermal energy of the medium $W / n_0 T_e = |E|^2 / 4\pi n_0 T_e > 1$. The particles are in the field of an external wave, the length of which, for the sake of simplicity of calculations, is set equal to infinity, oscillating with the ion speed is $u_{0\alpha} = -(e_\alpha |E_0| / m_\alpha \omega_0) \cos \Phi$. The components of the field strength of the external wave are determined as follows

$$E_0 = -i \cdot \left[|E_0| \exp(i\omega_0 t + i\phi) - |E_0| \exp(-i\omega_0 t - i\phi) \right] / 2. \quad (1)$$

For complex slowly varying components E_n, \bar{E}_n , respectively, of the HF electric field, LF electric field of the excited short-wavelength instability spectrum, and also for the ion charge density $v_{i,n} = en_{i,n}$, the following system of equations can be written [9].

Silin's hydrodynamic model ($W / n_0 T_e = |E|^2 / 4\pi n_0 T_e > 1$).

$$\frac{\partial E_n}{\partial t} - i \frac{\omega_{pe}^2 - \omega_0^2}{2\omega_0} E_n + \theta \cdot \frac{n^6}{n_M^6} \cdot E_n - \frac{4\pi\omega_{pe} v_{in}}{k_0 n} J_1(a_n) \cdot \exp(i\phi) -$$

$$- i \frac{\omega_0}{2en_0} \sum_m v_{in-m} \cdot \left[E_{-m}^* \cdot J_2(a_{n-m}) \exp[2i\phi] + E_m \cdot J_0(a_{n-m}) \right] = 0, \quad (2)$$

$$\frac{\partial^2 v_{in}}{\partial t^2} = -\Omega_i^2 \left\{ v_{in} \left[1 - J_0^2(a_n) + \frac{2}{3} J_2^2(a_n) \right] + \frac{ik_0 n}{8\pi} J_1(a_n) \left[E_n \cdot e^{-i\phi} - E_{-n}^* \cdot e^{i\phi} \right] + \right.$$

$$\left. + \frac{n^2 k_0^2}{64\pi^2 en_0} \sum_m J_0(a_n) \cdot E_{n-m} \cdot E_{-m}^* + \frac{nk_0^2}{64\pi^2 en_0} J_2(a_n) \cdot \sum_m (n-m) \left[E_{n-m} \cdot E_m \cdot e^{-2i\phi} + E_{m-n}^* \cdot E_{-m}^* \cdot e^{2i\phi} \right] \right\}, \quad (3)$$

$$\frac{\partial E_0}{\partial t} - i\Delta E_0 = -\frac{\omega_0}{2en_0} \sum_m v_{i,-m} \cdot \left[E_{-m}^* \cdot J_2(a_m) \exp[2i\phi] + E_m \cdot J_0(a_m) \right]. \quad (4)$$

Hybrid Silin model ($W / n_0 T_e = |E|^2 / 4\pi n_0 T_e > 1$).

$$\frac{\partial E_n}{\partial t} - i \frac{\omega_{pe}^2 - \omega_0^2}{2\omega_0} E_n + \theta \cdot \frac{n^6}{n_M^6} \cdot E_n - \frac{4\pi\omega_{pe} v_{in}}{k_0 n} J_1(a_n) \cdot \exp(i\phi) -$$

$$- i \frac{\omega_0}{2en_0} \sum_m v_{in-m} \cdot \left[E_{-m}^* \cdot J_2(a_{n-m}) \exp[2i\phi] + E_m \cdot J_0(a_{n-m}) \right] = 0, \quad (5)$$

$$\frac{\partial E_0}{\partial t} - i\Delta E_0 = -\frac{\omega_0}{2en_0} \sum_m v_{i,-m} \cdot \left[E_{-m}^* \cdot J_2(a_m) \exp[2i\phi] + E_m \cdot J_0(a_m) \right]. \quad (6)$$

When describing ions by particles, one can use the equations of motion

$$\frac{d^2 x_s}{dt^2} = \frac{e}{M} \sum_n \bar{E}_n \cdot \exp\{ik_0 n x_s\}. \quad (7)$$

where is the intensity of the slowly changing electric field

$$\bar{E}_n = \left(-\frac{4\pi i}{k_0 n} \right) v_{in} \left[1 - J_0^2(a_n) + \frac{2}{3} J_2^2(a_n) \right] + \frac{1}{2} J_1(a_n) \left[E_n \cdot e^{-i\phi} - E_{-n}^* \cdot e^{i\phi} \right] -$$

$$- \frac{ink_0}{16\pi en_0} J_0(a_n) \sum_m E_{n-m} \cdot E_{-m}^* -$$

$$- \frac{ik_0}{16\pi en_0} J_2(a_n) \cdot \sum_m (n-m) \left[E_{n-m} \cdot E_m \cdot e^{-2i\phi} + E_{m-n}^* \cdot E_{-m}^* \cdot e^{2i\phi} \right]. \quad (8)$$

Here, the arguments of the Bessel functions $a_n = nek_0 E_0 / m_e \omega_0^2$, $\Phi = \omega_0 t + \phi$, and $v_{i,n} = en_{i,n}$, $v_{i,n} = en_0 \frac{k_0}{2\pi} \int_{-\pi/k_0}^{\pi/k_0} \exp(-ink_0 x_s(x_0, t)) dx_{s0}$ are the components of the ion charge density, the HF field of the spectrum $E = \exp\{-i\omega_0 t\} \cdot \sum_n E_n \cdot \exp\{ink_0 x\}$, and the term $\theta \cdot (n / n_M)^6 E_n$ models the damping of the HF modes of the spectrum by electrons, with $n_M = 20$, $\Delta = (\omega_{pe}^2 - \omega_0^2) / 2\omega_0$. In addition, a dispersion term can be added to (2) and (5), which is proportional to $\beta = k_0^2 v_{Te}^2 / 2\omega_0$, $v_{Te}^2 = T_e / m_e$, x_s – the coordinate of the s-th particle simulating the ion. The expressions proportional to $J_0(a_n)$, correspond to slow motions, and the expressions proportional to $J_{\pm 2}(a_n)$, are determined by the contribution to the nonlinearity of the second harmonic, n_0 is the unperturbed plasma density, T_e is the electron temperature, and the ions are assumed to be cold at the initial moment.

Zakharov's hydrodynamic model (supersonic regime) under conditions ([2], see also [7,9]) $W / n_0 T_e = |E|^2 / 4\pi n_0 T_e < 1$.

$$\frac{\partial E_n}{\partial t} - i \frac{\omega_{pe}^2 - \omega_0^2 + k_0^2 n^2 v_{Te}^2}{2\omega_0} E_n + \theta \cdot \frac{n^6}{n_M^6} \cdot E_n - i \frac{\omega_0}{2n_0} \cdot \left[n_{in} E_0 + \sum_{m \neq 0} n_{in-m} E_m \right] = 0, \quad (9)$$

$$\frac{\partial^2 n_{i,n}}{\partial t^2} = -\frac{k_0^2 n^2}{16\pi M} \left[E_n E_0^* + E_0 E_{-n}^* + \sum_{m \neq 0, n} E_{n-m} E_{-m}^* \right]. \quad (10)$$

$$\frac{\partial E_0}{\partial t} - i \frac{\omega_0}{2n_0} \cdot \sum_m n_{i,-m} E_m = 0. \tag{11}$$

Hybrid model of Zakharov under conditions $W / n_0 T_e = |E|^2 / 4\pi n_0 T_e < 1$.

$$\frac{\partial E_n}{\partial t} - i \frac{\omega_{pe}^2 - \omega_0^2 + k_0^2 n^2 v_{Te}^2}{2\omega_0} E_n + \theta \cdot \frac{n^6}{n_M^6} \cdot E_n - i \frac{\omega_0}{2n_0} \cdot \left[n_n E_0 + \sum_{m \neq 0} n_{n-m} E_m \right] = 0, \tag{12}$$

$$\frac{\partial E_0}{\partial t} - i \frac{\omega_0}{2n_0} \cdot \sum_m n_{i,-m} E_m = 0. \tag{13}$$

When describing ions by particles, one can use the equations of motion,

$$\frac{d^2 x_s}{dt^2} = \frac{e}{M} \sum_n \bar{E}_n \cdot \exp\{ik_0 n x_s\}, \tag{14}$$

where is the intensity of the slowly changing electric field

$$\bar{E}_n = -ik_0 n \tilde{\phi}_n = \frac{-ik_0 n n_{i,n} T}{en_0} + \frac{-ik_0 n e}{4m\omega_p^2} \left[E_n E_0^* + E_0 E_{-n}^* + \sum_{m \neq 0, n} E_{n-m} E_{-m}^* \right]. \tag{15}$$

In this case, the ion density perturbations are $n_{in} = n_0 \cdot \frac{k_0}{2\pi} \int_{-\pi/k_0}^{\pi/k_0} \exp[-ink_0 \cdot x_s(x_0, t)] \cdot dx_{s0}$, where the term $\theta \cdot E_n \cdot n^6/n_M^6$ in the equations (9) and (12) models the damping of the HF modes of the spectrum on electrons, and HF field spectrum $E = \exp\{-i\omega_0 t\} \cdot \sum_n E_n \cdot \exp\{ink_0 x\}$.

It is important to note that for the equations of the hydrodynamic model (2)–(4) and the hybrid model (5)–(8) of Silin, taking into account the representation $J_1(a_n) \approx a_n/2$, $J_0(a_n) \approx 1$, $J_2(a_n) \approx a_n^2/8$, coincide with those obtained for the nonisothermal plasma of the hydrodynamic model (7)–(9) and the hybrid model of Zakharov (10)–(13), respectively, up to the detuning value and taking into account the replacements $E_0 \rightarrow iE_0$ and $E_0^* \rightarrow iE_0^*$.

From the results of the linear theory [2] (see also [7,9]), it follows that in the Zakharov model, the correction to the frequency normalized to the Langmuir frequency can be written as

$$\left(\delta'\right)^2 = \frac{\left(\Delta'\right)^2}{2} \pm \sqrt{\frac{\left(\Delta'\right)^4}{4} + B\left(\Delta'\right)^2}, \tag{16}$$

Where $B = \frac{1}{2} \frac{m_e}{M} \frac{|E_0|^2}{4\pi n_0 T_e}$. The increment (imaginary part $\delta' = \Omega / \omega_{pe}$) increases with the growth of the wave number of perturbations, reaching its maximum value at large values of the wave number. That is, the growth rate of plasma density perturbations even increases with a decrease in their scale. In Silin's model, at detuning values $\Delta' = (m_e 2M)^{1/3} J_1^{2/3}(a_{n_m})$, the relative increment reaches the values

$$\delta' = \pm \frac{i}{\sqrt[3]{2}} \left(\Delta'\right)^{1/3} = \pm \frac{i}{\sqrt[3]{2}} \left(\frac{m_e}{M}\right)^{1/3} J_1^{2/3}(a_n). \tag{17}$$

Here $a_n = n(e k_0 E_0 / m_e \omega_0^2)$ and $k_m = k_0 n_m$. At $a_{n_m} = 1.84$, $\delta'_{\max} = \pm 0.44i \left(\frac{m_e}{M}\right)^{1/3}$. As the instability develops, the amplitude of the Langmuir wave decreases, and the increment maximum shifts to the short-wavelength region [7, 9].

It is useful to note that the values of the perturbation increments in the case of parametric instability in the Zakharov model increase as their scale decreases. Moreover, in the Zakharov model, a decrease in the amplitude of the pump field leads to a decrease in the increments in the entire region of instability. In the Silin model, such a pump depletion process shifts the growth rate maximum to shorter wavelengths without decreasing its value (17). Thus, the process of energy movement to the short-wavelength part of the spectrum in the two models is largely determined by the linear mechanisms of the growth of perturbations.

3. FORMATION OF CAVITIES IN SYSTEMS WITH A SMALL NUMBER OF SPECTRUM MODES AND PARTICLES SIMULATING IONS

In the case of a small number of spectrum modes in Zakharov's hydrodynamic model, several large-scale density caverns are formed, which then deepen. This can be explained by the form of the initial spectrum, which is more clearly represented by relatively long-wavelength perturbations that form the initial scale of the cavity. Since the growth rate of

short-wave disturbances is larger, even under conditions of their small initial amplitude they grow rapidly and this leads to their phase synchronization (which will be discussed below) under the action of the field of intense Langmuir oscillations and deepening of the resulting cavity (that is, to the formation in some degree of aggravation). The process of formation of deepening density caverns in Silin's hydrodynamic model develops in a similar way.

As the amplitude of the pump wave decreases, the increment maximum shifts towards larger wavenumbers without changing its value. In addition, the pump wave contributes to phase synchronization of the growing modes of the spectrum, thereby forming the spatial structure of the cavity. The distance between spatial modes (there are only 40 of them here) in the spectrum is inversely proportional to the size of the region under consideration; therefore, only a few caverns form in this region (this can be seen from the position of the spectrum maximum at the beginning of the process). The gradual connection to the formation of cavities of synchronized short-wavelength modes of the spectrum leads to the implementation of the peaking mode and to the deepening of the caverns (see Fig. 1).

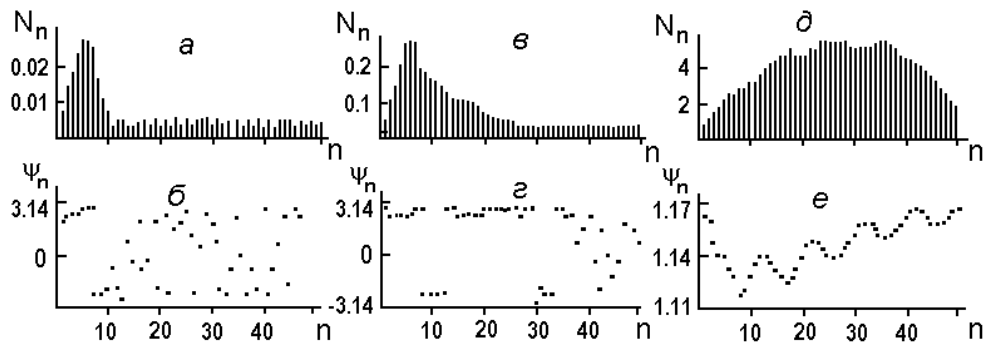


Figure 1. The process of formation of a wave packet of Langmuir waves during instability [10]. One can see phase synchronization (lower figures) and broadening of the spectrum $N_n = N_n \exp(i\Psi_n)$, $E_n = 4\pi e N_n / 2k_0 n$, where for time points $\tau = 4$; $\tau = 7$; $\tau = 8$

In hybrid models, the presence of a large number of particles simulating ions leads to noticeable amplitudes of the initial wide short-wavelength spectrum. Since the increments in the models of non-isothermal Zakharov plasma only increase with moving to the short-wavelength region, it is not surprising that the process acquires an explosive character (see, for example, [8]). It is clear that refinement of the spatial density structure occurs already at the initial stage of the instability process. The appearance of larger-scale deepening caverns is difficult in this case (see Fig. 2).

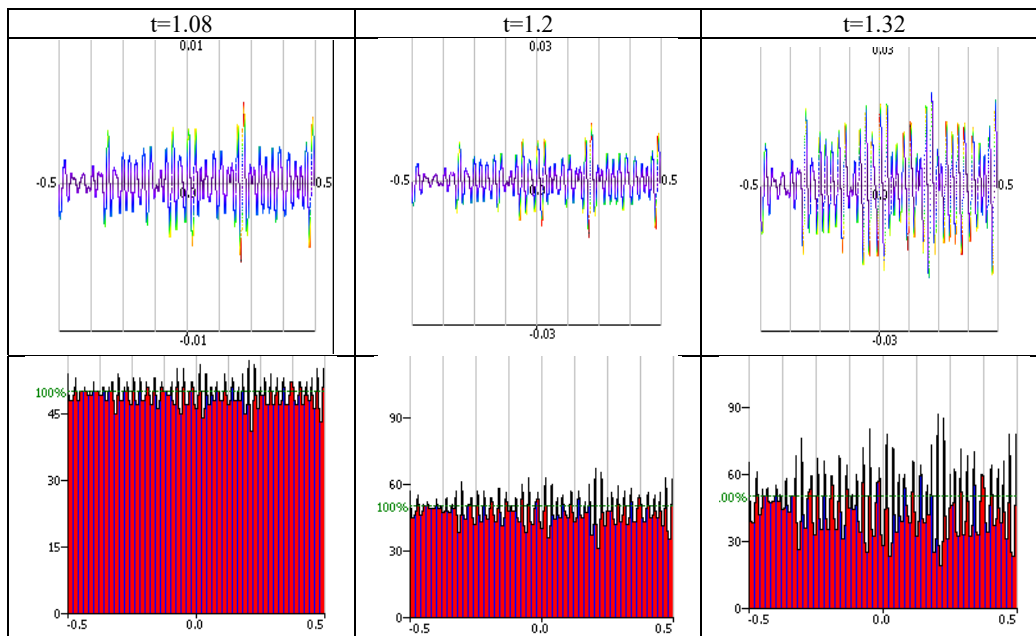


Figure 2. Phase plane (velocity, coordinate) and plasma density at different times for Zakharov's hybrid model. The number of spectrum modes is 201, the number of particles simulating ions is 10,000 [11]

In a cold plasma described by Silin's models, the process of motion of perturbations along the spectrum also develops rapidly at the initial stage of instability. In the Silin hybrid model, with a small number of modes and model particles, one can see the formation of a large-scale deepening cavity and its destruction due to the intersection of particle trajectories [5]. In the nonlinear regime, with a larger number of modes and particles, the caverns are reduced throughout the entire volume of the plasma. Moreover, the scale of even deep caverns remains very small (see Fig. 3).

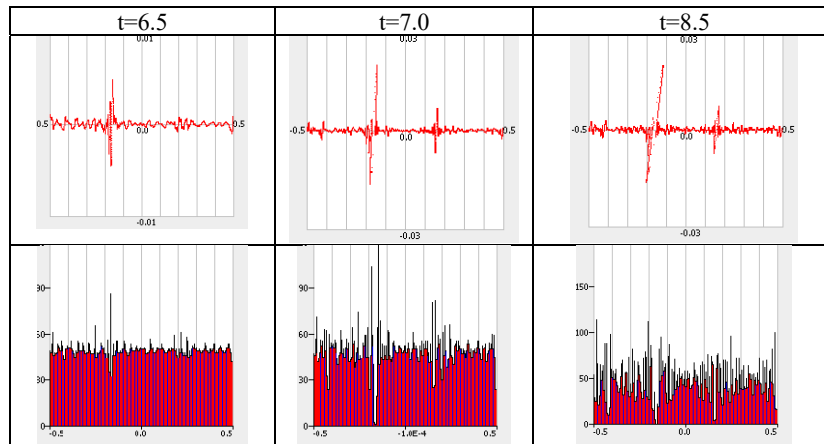


Figure 3. Phase plane (velocity, coordinate) and plasma density at different times for Silin's hybrid model. The number of spectrum modes is 201, the number of particles simulating ions is 10,000 [11]

4. FORMATION OF SPATIAL PLASMA DENSITY DISTRIBUTIONS IN SYSTEMS WITH A LARGE NUMBER OF PARTICLES SIMULATING IONS

Generally speaking, it remains unclear whether the emerging caverns move in space. In other words, do the phases of the amplitudes of charge density and ion density varying slowly with time $v_{in} = en_{in}$ and n_{in} . In addition to explaining their dynamics, this circumstance, as shown below, affects the process of synchronization of the Langmuir spectrum of instability. In the calculations, only the obvious condition $n_{i,-n} = (n_{i,n})^*$ was assumed to be satisfied. However, as shown by model calculations for a large number of spectrum modes (the number of which is 1001) and a large number of particles simulating ions, equal to 50,000, phase changes for the spectral components of the plasma density were not noticed. The caverns practically did not change their position, changing only their amplitude (see Fig. 4).

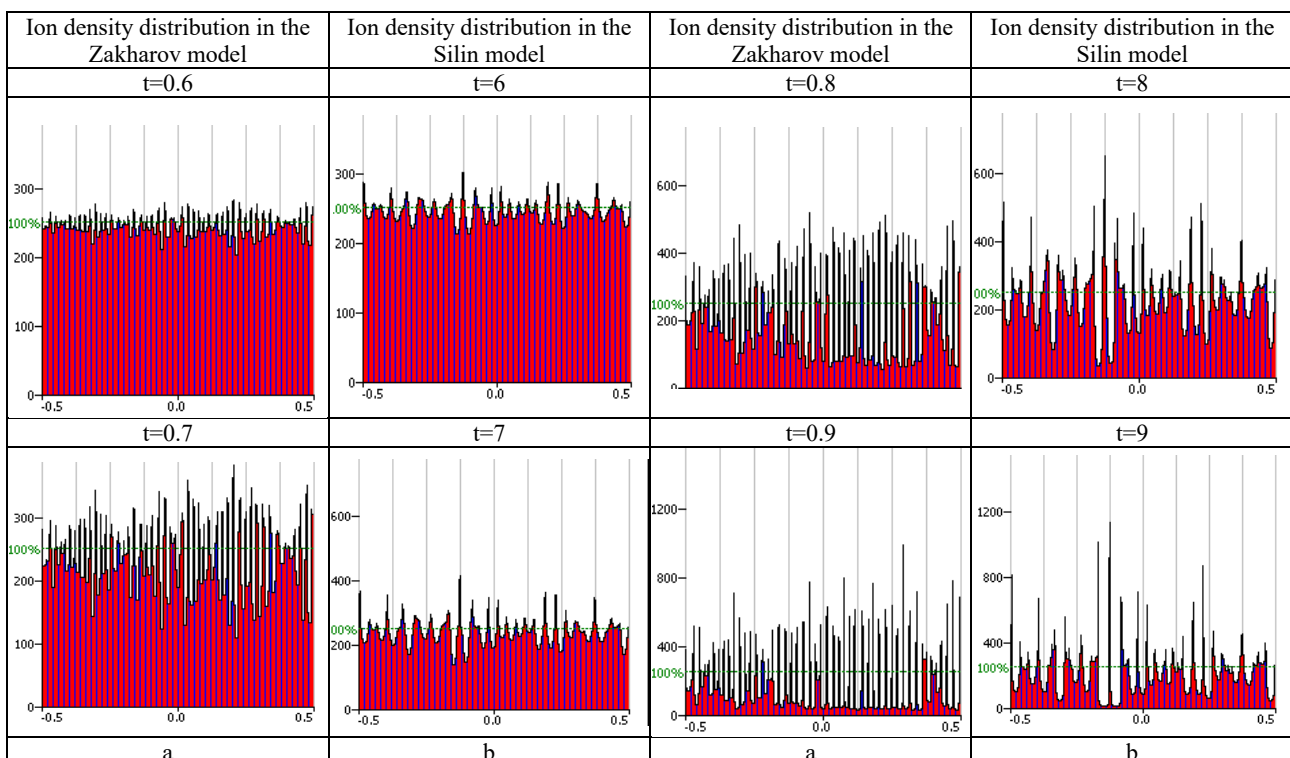


Figure 4. Plasma ion density distribution in the Zakharov (a) and Silin (b) models, the number of particles simulating ions is 50000, the number of spectra modes is 1001. Absorption in the system is 0.05. [11]

5. PHASE SYNCHRONIZATION MECHANISMS IN THE ZAKHAROV AND SILIN MODELS

The process of phase synchronization of short-wavelength Langmuir waves of the instability spectrum $E_n = |E_n| \cdot \exp\{i\varphi_n\}$ can be illustrated as follows. From equations (7), (10) at the initial stage of instability in the Zakharov model, one can obtain a simple equation for the phase of an individual mode of the RF Langmuir spectrum

$$\frac{\partial \varphi_n}{\partial t} - \Delta_z = R_z \cdot \text{Cos}\{\phi - \varphi_n\} \tag{18}$$

where $\Delta_z = \frac{\omega_{pe}^2 - \omega_0^2 + k^2 n^2 v_{Te}^2}{2\omega_0}$ and $R_z = \frac{\omega_0 n_m E_0}{2n_0 E_n}$. Obviously, in the absence of changes in the position of the caverns, and at a significant value of $R_z \propto E_0 / E_n \gg 1$, the phases of the RF spectrum modes are able to synchronize.

Accordingly, equations (2), (5) in the initial stage of instability for the phases of the RF modes of the Langmuir spectrum $E_n = |E_n| \cdot \exp\{i\varphi_n\}$ can be written as

$$\frac{\partial \varphi_n}{\partial t} - \Delta_s = R_s \cdot \text{Sin}\{\phi - \varphi_n\}, \tag{19}$$

where $\Delta_s = \frac{\omega_{pe}^2 - \omega_0^2}{2\omega_0}$, $R_s = \frac{4\pi\omega_{pe} v_{in}}{k_0 n E_n} J_1(a_n) \propto J_1(a_n) / E_n$, and $J_1(a_n) / E_n \gg 1$ for rapidly growing modes of the HF spectrum allows the phases of the spectrum to be synchronized.

Despite the development of small-scale modulation of the plasma density in the Zakharov and Silin models, the nature of the formation of cavities, even on small scales, is largely associated with mode locking. This process is illustrated in Fig. 5, which shows the formation of small-scale caverns.

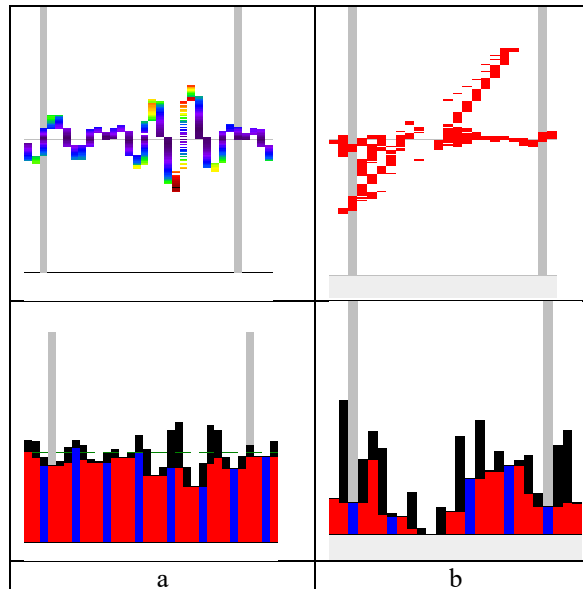


Figure 5. Formation of small-scale plasma ion density caverns in the Zakharov (a) Silin (b) hybrid models. The upper fragments illustrate the phase (velocity and coordinate of particles) space near the caverns, the lower fragments illustrate the particle density distribution [11]

In Zakharov's model for a nonisothermal plasma, expression (13) is valid for the components of the low-frequency field strength, and expression (8) is valid for Silin's cold plasma model. It is important to note that the right-hand sides of these expressions contain terms, the number of which is significant for wide spectra of short-wave disturbances in hybrid models. Therefore, the RF pressure is very high in this case, especially in the Silin model for cold plasma. Perhaps this is why the formation of the small-scale cavity shown in Fig. 5b demonstrates such a dynamic character. In addition, the particle extrusion mode is implemented here, which expands the cavity. It is also possible to switch to the mode of intersection of particle trajectories, which destroys the cavity, as can be seen in [5].

6. CONCLUSION

The paper considers the instability of intense Langmuir oscillations in nonisothermal (Zakharov's model) and cold (Silin's model) 1D plasma. The main attention is paid to the formation of plasma density caverns in the hydrodynamic and hybrid (electrons are described hydrodynamically, ions are described by model particles) representations.

In the hydrodynamic representation, with a small number of spectrum modes, large-scale plasma density caverns are formed, which rapidly deepen. This process is supported by the appearance of small-scale perturbations, and phase synchronization of the Langmuir waves of the instability spectrum is observed (Section 5). This phase synchronization of the spectrum modes is quite capable of fulfilling the role that was previously proposed to be given exclusively to the effect of extrusion of particles from the cavity by the field.

In hybrid models, where ions in the region of consideration are described by model particles, the number of which in the one-dimensional case $10^4 \div 5 \cdot 10^4$ (which in the three-dimensional case corresponds to the number of particles $10^{12} \div 10^{14}$)

the initial spectrum of perturbations is very wide and rather intense, which leads to an explosive growth of perturbations in the Zakharov model [8] and a rapid development of instability in Silin's model. In this case, in the developed instability regime, the formation of many small-scale plasma density caverns is observed. It is important to note that the caverns practically do not change their position; phase changes for the spectral components of the plasma density were not observed. It is the presence of this small-scale modulation due to the Fermi effect that rapidly forms the normal velocity distribution of ions [7]. In this case, the effect of particle heating due to Landau damping loses its primacy [9]. Only individual small-scale caverns demonstrate dynamics (see Fig. 5) similar to the development of caverns in the hydrodynamic representation.

Thus, the notions that plasma density caverns, which form during the instability of intense Langmuir oscillations, first appear on a large scale and only then deepen due to the extrusion of particles by the HF field or due to the development of energy motion along the spectrum are only partly true. In fact, when describing ions by particles due to the wide initial spectrum (due to the discreteness of the ionic component), many small-scale cavities immediately appear and the appearance of large deepening cavities becomes unlikely.

Acknowledgements

Author is sincerely grateful to Krzysztof Pawlowski and Jarosław Korbicz for constructive discussion in CFT PAN (Warszawa).

ORCID IDs

©Volodymyr M. Kuklin, <https://orcid.org/0000-0002-0310-1582>

REFERENCES

- [1] V.E. Zakharov, "Collapse of Langmuir waves", Soviet Physics JETP, **35**(5), 908 (1972), <https://www-thphys.physics.ox.ac.uk/people/AlexanderSchekochihin/notes/PlasmaClassics/zakharov72.pdf>
- [2] E.A. Kuznetsov, "On the averaged description of Langmuir waves in plasma," Sov. Plasma Phys. The science. **2**(2), 327 (1976).
- [3] A.I. Dyachenko, et al "Two-dimensional Langmuir collapse and two-dimensional Langmuir cavitons", JETP Letters. Science, **44**, 504 (1986).
- [4] A.Y. Wong, and P.Y. Cheung, Phys. Rev. Lett. **52**(14), 1222 (1984), <https://doi.org/10.1103/PhysRevLett.52.1222>
- [5] V.V. Chernousenko, V.M. Kuklin, and I.P. Panchenko, *The structure in nonequilibrium media. In book: The integrability and kinetic equations for solitons*, (Nauk. Dumka, Kyiv, 1990), pp. 472.
- [6] V.P. Silin, "Parametric resonance in plasma", ZhETF, **48**, 1679 (1965).
- [7] A.V. Kirichok, V.M. Kuklin, A.V. Pryimak, and A.G. Zagorodny, "Ion heating, burnout of the HF field and ion sound generation with the development of modulation instability of an intensive Langmuir wave in a plasma", Physics of Plasmas, **22**, 092118 (2015), <https://doi.org/10.1063/1.4931058>
- [8] K.L. Clark, G.L. Payne, and D.R. Nicholson, "A hybrid Zakharov particle simulation of ionospheric heating", Phys. Fluids B Plasma Phys. **4**(3), 708 (1992), <https://doi.org/10.1063/1.860269>
- [9] V.M. Kuklin, *Selected chapters (theoretical physics)*, (V.N. Karazin KhNU, Kharkiv, 2021), pp. 244.
- [10] V.M. Kuklin, and S.M. Sevidov, "On the nonlinear theory of stability of intense oscillations of cold plasma", Sov. Plasma Phys. **14**(10), 1180 (1988).
- [11] O.V. Pryimak, PhD Dissertation, "Mathematical models for describing the processes of modulation instabilities of an intense wave field", Karazin Kharkiv University, 2020.

ПРО МЕХАНІЗМИ ФОРМУВАННЯ КАВЕРН ЩІЛЬНОСТІ ПРИ НЕСТІЙКОСТІ ІНТЕНСИВНИХ ЛЕНГМЮРІВСЬКИХ КОЛИВАНЬ У ПЛАЗМІ

В.М. Куклін

*Харківський національний університет імені В.Н. Каразіна, Харків, Україна
пл. Свободи 4, Харків, Україна, 61022*

У роботі розглянуто нестійкість інтенсивних ленгмюрівських коливань у неізотермічній (модель Захарова) та холодній (модель Силіна) 1D плазми. Основна увага приділена процесу формування каверн щільності плазми у гідродинамічному та у гібридному (електрони описані гідродинамічно, іони – модельними частинками) представленнях. У гідродинамічному поданні при невеликій кількості мод спектру спостерігаються великомасштабні каверни щільності плазми, які швидко поглиблюються. Цей процес підтримується появою дрібномасштабних обурень, причому спостерігається синхронізація фаз ленгмюрівських хвиль спектра нестійкості. Ця синхронізація фаз мод спектру цілком здатна виконати ту роль, яку раніше пропонували віддати виключно ефекту видавлювання полем частинок з каверни. У гібридних моделях у області розгляду іони описані модельними частинками, число яких у одновимірному випадку $10^4 \div 5 \cdot 10^4$ (що у тривимірному випадку відповідає числу частинок $10^{12} \div 10^{14}$). Початковий спектр обурень дуже широкий і досить інтенсивний, що призводить до вибухового зростання збурень у моделі Захарова та швидкого розвитку нестійкості у моделі Силіна. При цьому в розвиненому режимі нестійкості спостерігається формування безлічі дрібномасштабних каверн щільності плазми. Саме наявність цієї дрібномасштабної модуляції за рахунок ефекту Фермі швидко формує нормальний розподіл іонів за швидкостями. В цьому випадку ефект нагрівання частинок за рахунок згасання Ландау втрачає першість. Показано, що каверни мало змінюють свого становища, фазові зміни для спектральних компонентів щільності плазми помічені не були. Тільки окремі дрібномасштабні каверни демонструють динаміку, подібну до розвитку каверн у гідродинамічному представленні.

Ключові слова: інтенсивні ленгмюрівські коливання, моделі опису Захарова та Силіна, дрібномасштабні малорухливі каверни щільності плазми, синхронізація фаз.

SUPERRADIATION OF MOBILE OSCILLATORS[†]

 **Eugen V. Poklonskiy***,  **Stanislav O. Totkal**

*V.N. Karazin Kharkiv National University, Kharkiv, Ukraine
Svobody Sq. 4, Kharkiv, Ukraine, 61022*

**Corresponding Author: evpoklonsky@karazin.ua*

Received May 25, 2022; accepted July 24, 2022

The paper considers the development of the process of superradiance of radiating oscillators interacting with each other by means of an electromagnetic field. The interaction of oscillators occurs both with the nearest neighbors and with all other oscillators in the system. In this case, the possibility of longitudinal motion of oscillators along the system, due to the action of the Lorentz force, is taken into account. It is shown that, regardless of the motion of the oscillators, for example, due to their different masses, the maximum attainable amplitude of the generation field changes little. However, the radiation efficiency depends on how this field is distributed in the longitudinal direction. In the case of a shift of the field maximum towards the ends of the system, the radiation efficiency can noticeably increase. In addition, the direction of the phase velocity of the external initiating field is important, which accelerates the process of phase synchronization of the oscillators. This can also affect the ejection of particles outside the initial region, and here the total number of ejected particles and their speed turn out to be important. It is discussed how the density of oscillators and the size of the region occupied by oscillators will change.

Keywords: Superradiance of moving oscillators, shift of the field maximum in the volume, change in the density of oscillators.

PACS: 03.65.Sq

Interest in the processes of generation of oscillations in superradiance regimes began with the well-known work of R.N. Dicke [1]. Superradiance is usually realized in open systems, when high-frequency energy is removed from the system. To a certain extent, this energy output can be equivalent to dissipative processes of a distributed type.

Previously, dissipative regimes of excitation or generation of an electromagnetic wave in open waveguide resonator systems such as a traveling wave lamp traditionally corresponded to the case of the interaction of the waveguide electromagnetic field with emitter particles, most often with moving beam electrons (see, for example, [2]). Since the system is open, the field leaves the waveguide, which for short systems is equivalent to losses or dissipative processes of a distributed type. The field damping decrement in such a waveguide or resonator without emitters or oscillators for such generation or amplification modes may be greater than the development increment of the generation process in the presence of these active elements [3–5]. In particular, one could consider the case of the interaction of a system of fixed oscillators with the field of an open resonator. In this case, the oscillators did not interact directly with each other, but only through the resonator field common to the system. The superradiance regime (see, for example, [1, 6, 7]), on the contrary, ensured precisely the interaction of oscillators with each other both with their nearest neighbours and with all other oscillators in the system. Moreover, due to sufficiently large distances between the particles, the interaction between them occurs only due to their own electromagnetic fields. The mechanism of phase synchronization of the radiation of such oscillators was discussed in [8–10].

Attempts to discover the similarity between dissipative instability regimes and superradiance in open systems began to be undertaken in [11, 12]. It is remarkable that the systems of equations describing the interaction of electron beams rotating in a magnetic field with the fields of a waveguide at cyclotron resonances, when simplified, were reduced to the descriptions of the interaction of oscillators considered in the above papers [13]. This circumstance indicated the existence of a common phase synchronization mechanism for all these cases. A detailed comparison was made of the dissipative mode of field generation in an open system, a resonator, with the superradiance mode in the same resonator uniformly filled with immobile excited oscillators. The analysis showed that the increments of the processes and the maximum achievable amplitudes of the field of these two regimes practically coincide [14].

If this resonator is filled with an active medium, a dissipative excitation regime is also possible, in which quantum oscillators interact only with the resonator field, and there is no direct interaction between them. The regime of superradiance in the same resonator, when quantum oscillators interact only with each other, is also discussed. It is important to note that at a relatively low density of oscillators, their wave functions do not overlap [15]; therefore, they can affect each other only by their own radiation fields. And here the increments of the processes and the maximum achievable amplitudes of the field of these two regimes practically coincide [16].

In this paper, we consider the behavior of a system of oscillators similar to the case studied earlier [14], but we take into account the possibility of longitudinal motion of oscillators along the resonator due to the action of the Lorentz force. We will be interested in how the maximum achievable amplitude of the generation field will change, how this field will be distributed in the longitudinal direction, how the density of oscillators and the size of the region occupied by oscillators will change.

[†] *Cite as:* E.V. Poklonskiy, and S.O. Totkal, East Eur. J. Phys. 3, 14 (2022), <https://doi.org/10.26565/2312-4334-2022-3-02>

© E.V. Poklonskiy, S.O. Totkal, 2022

SYSTEM OF EQUATIONS TAKING INTO ACCOUNT THE MOTION OF OSCILLATORS

The paper [14] gives equations for slowly changing the amplitude of oscillators and their total field in the case when the oscillators are stationary. Let us consider a system of oscillators [14], but take into account that the electric field $E_x(z, t)$, which arises when the oscillators oscillate, leads to the appearance of a magnetic field $H_y(z, t)$. (All designations correspond to [14]). As a result, the Lorentz force F_z acts on the oscillator, moving the oscillators along the longitudinal axis of the system:

$$\frac{\partial E_x}{\partial z} = -\frac{1}{c} \frac{\partial H_y}{\partial t} = \frac{i\omega}{c} H_y, \quad H_y = \frac{c}{i\omega} \frac{\partial E_x}{\partial z}, \quad F_z = -e \frac{v_x}{c} H_y. \quad (1)$$

The electric field of the oscillator (electron) at a point is equal to

$$E_x = 2\pi \cdot e \cdot A \cdot \omega \cdot c^{-1} \cdot e^{-i\omega t} \left(e^{ik(z-z_0)} \cdot \theta(z-z_0) + e^{-ik(z-z_0)} \cdot \theta(z_0-z) \right) = 2\pi \cdot e \cdot A \cdot \omega \cdot c^{-1} \cdot e^{-i\omega t} \cdot e^{ik|z-z_0|}.$$

Therefore, the magnetic field of this oscillator is

$$H_y = \frac{c}{i\omega} \frac{\partial E_x}{\partial z} = 2\pi \cdot e \cdot A \cdot \omega \cdot c^{-1} \cdot e^{-i\omega t} \left(e^{ik(z-z_0)} \cdot \theta(z-z_0) - e^{-ik(z-z_0)} \cdot \theta(z_0-z) \right),$$

and for the system of oscillators, we obtain the magnetic field of the system

$$H_y(z, t) = \frac{2\pi \cdot e \cdot \omega \cdot M}{c} \cdot e^{-i\omega t} \cdot \frac{1}{N} \sum_{s=1}^N A_s \left(e^{ik(z-z_s)} \cdot \theta(z-z_s) - e^{-ik(z-z_s)} \cdot \theta(z_s-z) \right),$$

and the force acting on the oscillator at the point

$$F_{z_j} = -\pi \cdot e^2 \cdot k^2 \cdot M \cdot \operatorname{Re} \left[A_j^* \cdot \frac{1}{N} \sum_{s=1}^N A_s \left(e^{ik(z_j-z_s)} \cdot \theta(z_j-z_s) - e^{-ik(z_j-z_s)} \cdot \theta(z_s-z_j) \right) \right] \quad (2)$$

In contrast to [14], the coordinates of the oscillators change. The equations of motion of oscillators under the action of force (2) have the form

$$\frac{dv_{z_j}}{dt} = -\frac{\pi \cdot e^2 \cdot k^2 \cdot M}{m_1} \operatorname{Re} \left[A_j^* \cdot \frac{1}{N} \sum_{s=1}^N A_s \left(e^{ik(z_j-z_s)} \cdot \theta(z_j-z_s) - e^{-ik(z_j-z_s)} \cdot \theta(z_s-z_j) \right) \right], \quad (3)$$

$$\frac{dz_j}{dt} = v_{z_j}, \quad (4)$$

Equation (3-4), together with the equation for changing the amplitude of the oscillator ([14], equation (19)) constitutes our system of equations.

In dimensionless form, the system takes the form

$$\frac{dA_j}{d\tau} = \frac{i\alpha}{2} \cdot |A_j|^2 A_j - \frac{1}{N} \sum_{s=1}^N A_s \cdot e^{i2\pi|Z_j-Z_s|} - E_0 \cdot e^{2\pi i Z_j} = \frac{i\alpha}{2} \cdot |A_j|^2 A_j - \frac{1}{2} E(Z_j, \tau) - E_0 \cdot e^{2\pi i Z_j}, \quad (5)$$

$$\frac{dV_{Z_j}}{d\tau} = -\beta \cdot \frac{4\alpha}{3} \cdot \operatorname{Re} \left(A_j^* \cdot \frac{1}{N} \sum_{s=1}^N A_s \cdot e^{i2\pi|Z_j-Z_s|} \cdot \operatorname{sign}(Z_j - Z_s) \right), \quad (6)$$

$$\frac{dZ_j}{d\tau} = \frac{1}{2\pi} V_{Z_j}, \quad (7)$$

here $\gamma = \gamma_0^2 / \delta_D = \pi e^2 M / mc$; $E = eE / m\omega\gamma a_0$, $A = A / a_0$; $k_0 z = 2\pi Z$; $\tau = \gamma t$; $\gamma_0^2 = \pi e^2 n_0 / m = \omega_{pe}^2 / 4$, $\alpha = 3k_0^2 a_0^2 \omega / 4\gamma$, $\beta = m / m_1$, $M = b \cdot n_0$, b - is the length of the considered space in the longitudinal direction, n_0 is the density of particles per unit volume, m, m_1 - are the masses of the electron and the oscillator, respectively, E_0 is the amplitude of the external field traveling in the positive direction of the Z axis.

The intensity of the electric field of oscillator radiation in dimensionless units is written by the expression

$$E_x(Z, \tau) = \frac{2}{N} \sum_{s=1}^N A_s \exp\{i2\pi|Z-Z_s|\}. \quad (7)$$

RESULTS OF NUMERICAL CALCULATIONS

In the article [14], the calculations were carried out with the number of particles $N=3600$ in the case of motionless oscillators. For system (5-8) similar calculations were carried out ($\beta=0$, fixed oscillators) at $N=3600$, $N=10000$, $N=20000$. The results practically did not differ, therefore, all further calculations were carried out at $N=10000$.

The following options are selected. The number of particles $N=10000$, $\alpha=1$, the amplitude of the additional external field that initiates the superradiance process, $E_0=0.02$. At the initial moment of time, the oscillators are uniformly distributed along the system, their velocities are equal to zero $V_j(0) = 0$, the amplitude modules of the oscillators are equal to unity $|A_j(0)|=1$, their phases ψ_j have random values in the range $(-\pi, \pi)$, additional external field that initiates the process of superradiance $E_0=0.02$.

The parameter β (the ratio of the mass of the charge to the mass of the oscillator) took the values 0, 0.1, 0.5, 1. Larger values of the parameter β correspond to lighter and more mobile oscillators.

Figure 1(a,b,c,d) shows the time dependence of the modulus of the maximum value of the field in the system and the field at the edges of the system ($Z=0$ and $Z=1$) and for different values of the parameter β .

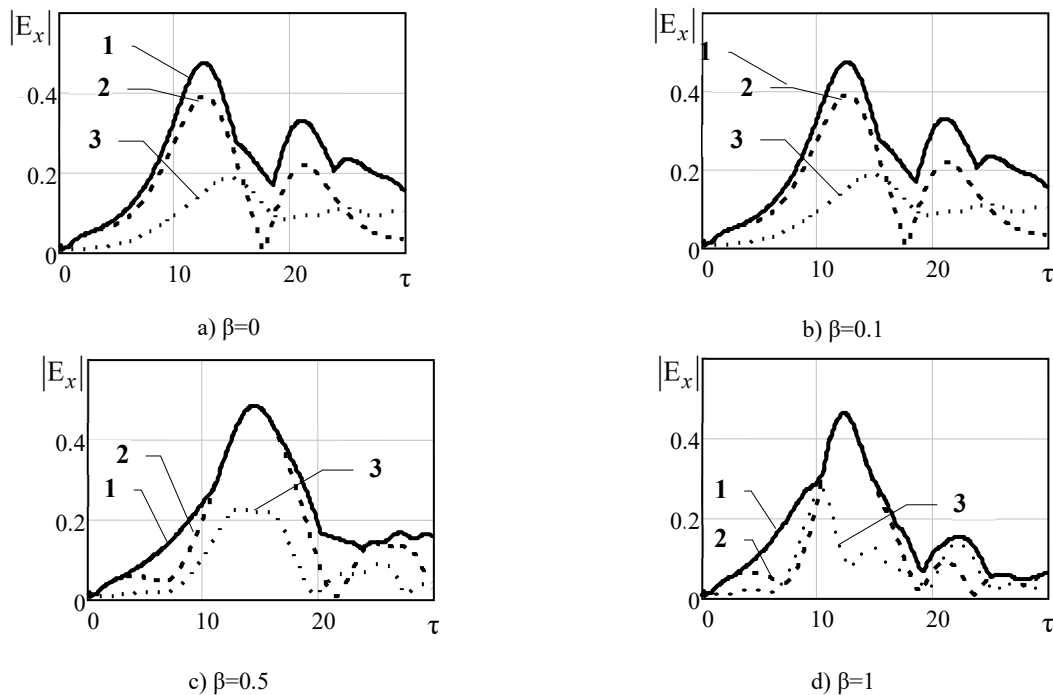


Figure 1. Dependence of the field modulus in different parts of the system on time τ
 $1 - \max|E_x|, 2 - |E_x(Z=1)|, 3 - |E_x(Z=0)|$

As can be seen from these figures, taking into account the motion of oscillators does not affect the maximum field strength in the system. At $\beta=0$ (the oscillators are immobile) and at $\beta=0.1$ (massive and slow-moving oscillators), the field maximum is observed inside the system, which was observed in [14]. But at $\beta=0.5$ and $\beta=1$, the field maximum is observed at the end at the end of the system ($Z=1$).

Since the energy output from the system is determined by the value of the field at the ends, in the case when the maximum amplitude is reached at the end, the radiation efficiency is the highest. The change in efficiency can be estimated from the ratio of the squares of the field amplitude at the end to the corresponding value at the maximum. At $\beta=0$ and $\beta=0.1$ this ratio is equal to 0.66, at $\beta=0.5$ and $\beta=1$ this ratio is obviously equal to 1.

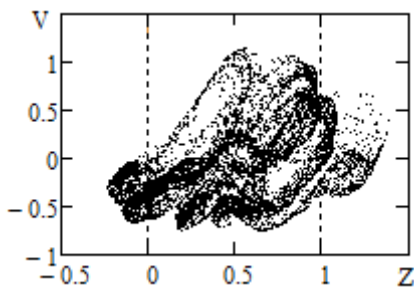


Figure 2. Distribution in space of velocities V of oscillators at $\beta=1$ at the moment $\tau=12$.

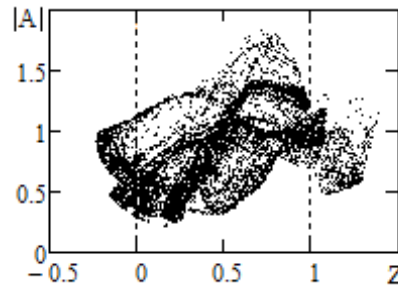


Figure 3. Oscillator amplitude distribution $|A|$ in space at $\beta=1$ at the moment $\tau=12$.

Figures 2 and 3 show the spatial distribution of velocities and amplitude modules for all particles at $\beta=1$ at the moment of reaching the field maximum $\tau=12$.

As can be seen from the figures, the particles exit from both ends, and particles fly out to a greater distance in the direction of the external field (the wave vector of the external field is oriented in the direction of the Z axis) from the end of the system ($Z>1$), where the field is maximum, and the particles emitted at the beginning of the system ($Z<0$), are located more compactly. By the time the field reaches its maximum, $\tau=12$, the coordinate $Z<0$ for 15% of the particles and $Z>1$ for 10% of the particles. Those. a larger number of particles flew out through the beginning of the system against the external field. There is an expansion of the area occupied by oscillators and its shift.

Figures 4 and 5 show the time dynamics of particle expansion.

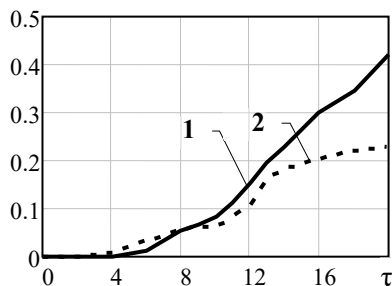


Figure 4. Time dependence of the fraction of particles emitted through the ends of the system, 1- departure through the beginning of the system ($Z<0$), 2- departure through the end of the system ($Z>1$)

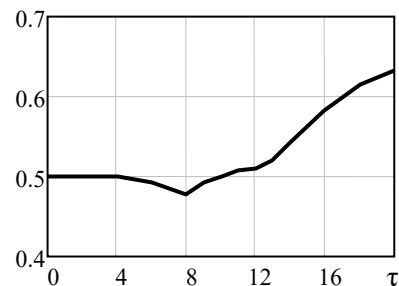


Figure 5. Time dependence of the fraction of particles in the first half of the system ($Z<0.5$).

It follows from the figures that up to the moment $\tau=8$, the fraction of particles in the first half of the system decreases (Fig. 5) and a greater number of particles leave through the end of the system, the particles move as a whole in the direction of the external field. But from the moment $\tau=8$ the dynamics becomes opposite, the system of particles, continuing to expand, shifts to the beginning against the direction of the external field.

It is important to note that, in the units under consideration, the average spontaneous emission amplitude of 10,000 oscillators is approximately equal to 0.01. On the other hand, the maximum amplitude of the induced emission of these oscillators, whose phases would be completely correlated, would reach unity.

Therefore, the amplitude of the initiating field is only twice the level of spontaneous emission ($E_0=0.02$). The achieved field amplitude in the system is approximately 0.5.

In other words, the energy density of the initiating field is four times greater than the corresponding spontaneous emission level of oscillators with a random phase distribution. The achieved level of radiation, in turn, is four times less than the maximum value of the energy density of all these oscillators, if their phases were completely correlated.

Acknowledgments

In conclusion, the authors express their gratitude to Prof. V.M. Kuklin for helpful discussions and constructive comments.

ORCID IDs

©Eugen V. Poklonskiy, <https://orcid.org/0000-0002-0310-1582>; ©Stanislav O. Totkal, <https://orcid.org/0000-0001-6112-8604>

REFERENCES

- [1] R.H. Dicke, "Coherence in Spontaneous Radiation Processes", *Physical Review*, **93**(1), 99-110 (1954), <https://doi.org/10.1103/PhysRev.93.99>
- [2] A.V. Kirichok, V.M. Kuklin, A.V. Mischin, and A.V. Pryimak, "Modelling of superradiation processes driven by an ultra-short bunch of charged particles moving through a plasma", *PAST*, **4**, 255-257 (2015), https://vant.kipt.kharkov.ua/ARTICLE/VANT_2015_4/article_2015_4_255.pdf
- [3] R.J. Briggs, *Electron-stream interaction with plasmas*, (Cambridge MIT Press, 1964), pp. 204.
- [4] V.U. Abramovich, and V.I. Shevchenko, "To the nonlinear theory of dissipative instability of a relativistic beam in plasma", *ZhETF*, **62**(4), 1386-1391 (1972), http://www.jetp.ras.ru/cgi-bin/dn/e_035_04_0730.pdf
- [5] A.N. Kondratenko, V.M. Kuklin, and V.I. Tkachenko, "On the anomalous level of beam energy loss during the development of dissipative beam instability", *Ukrainian Physical Journal*, **24**(4), 559-561 (1979).
- [6] A.V. Andreev, V.I. Emelyanov, and Yu.A. Il'inskiy, "Collective spontaneous radiation (Dicke superradiance)", *Soviet Physics Uspekhi*, **23**(8), 493 (1980), <https://iopscience.iop.org/article/10.1070/PU1980v023n08ABEH005024>
- [7] V.V. Zheleznyakov, and V.V. Kocharovskiy, "Polarization waves and superradiance in active media", *UFN*, **159**(2), 193-260 (1989), (in Russian)
- [8] V.M. Kuklin, D.N. Litvinov, S.M. Sevidov, and A.E. Sporov, "Simulation of synchronization of nonlinear oscillators by the external field", *East Eur. J. Phys.* **4**(1), 75-84 (2017), <https://doi.org/10.26565/2312-4334-2017-1-07>
- [9] V.M. Kuklin, D.N. Litvinov, and V.E. Sporov, "Superradiance of stationary oscillators", *PAST*, **4**(116), 217-220 (2018), https://vant.kipt.kharkov.ua/ARTICLE/VANT_2018_4/article_2018_4_217.pdf

- [10] V.M. Kuklin, “On the Nature of Coherents in the System of Oscillators”, PAST, 4(122), 91–95 (2019), https://vant.kipt.kharkov.ua/ARTICLE/VANT_2019_4/article_2019_4_91.pdf
- [11] V.M. Kuklin, D.N. Litvinov, and A.E. Sporov, “Superradiant emission regimes of the system of stationary oscillators”, PAST, 6, 101-104 (2017), https://vant.kipt.kharkov.ua/ARTICLE/VANT_2017_6/article_2017_6_101.pdf
- [12] V.M. Kuklin, D.N. Litvinov, and A.E. Sporov, “Dissipative generation regime of a system of stationary oscillators”, PAST, 6, 88-90 (2017), https://vant.kipt.kharkov.ua/ARTICLE/VANT_2017_6/article_2017_6_88.pdf
- [13] V.M. Kuklin, D.N. Litvinov, and V.E. Sporov, “The superradiance of bunch of rotating electrons”, PAST, 4(116), 221-224 (2018), https://vant.kipt.kharkov.ua/ARTICLE/VANT_2018_4/article_2018_4_221.pdf
- [14] V.M. Kuklin, and E.V. Poklonskiy, “Dissipative instabilities and superradiation regimes (classic models)”, PAST, 4(134), 138-143 (2021), https://vant.kipt.kharkov.ua/ARTICLE/VANT_2021_4/article_2021_4_138.pdf
- [15] V.M. Kuklin, and E.V. Poklonskiy “Energy exchange between the field and the active medium of the waveguide”, East Eur. J. Phys. 3, 46-53 (2019), <https://doi.org/10.26565/2312-4334-2019-3-06>
- [16] V.M. Kuklin, V.T. Lazurik, and E.V. Poklonskiy, “Semiclassic Models of the Dissipative Regime of Instability and Superradiation of a Quantum Radiator System”, East European Journal of Physics 2021, N2. P. 98-104. <https://doi.org/10.26565/2312-4334-2021-2-06>

НАДВИПРОМІНЮВАННЯ РУХОМИХ ОСЦИЛЯТОРІВ

Поклонський Є.В., Тоткал С.О.

*Харківський національний університет імені В.Н. Каразіна, Харків, Україна
Свободи пл. 4, Харків, Україна, 61022*

У роботі розглянуто розвиток процесу надвипромінювання осциляторів, що взаємодіють за допомогою електромагнітного поля між собою. Взаємодія осциляторів відбувається як з найближчими сусідами, так і з усіма іншими осциляторами в системі. При цьому враховано можливість поздовжнього руху осциляторів вздовж системи, зумовленого дією сили Лоренца. Показано, що незалежно від руху осциляторів, наприклад, через їхню різну масу, максимально досяжна амплітуда поля генерації змінюється мало. Однак, ефективність випромінювання залежить від того, як буде це поле розподілено в поздовжньому напрямку. У разі зсуву максимуму поля до торців системи ефективність випромінювання може помітно збільшуватися. Крім того, важливим є напрямок фазової швидкості зовнішнього ініціюючого поля, яке прискорює процес синхронізації фаз осциляторів. Це також здатне впливати на викид частинок за межі початкової області, причому тут виявляється важливим загальна кількість частинок, що виходять, і їх швидкість. Обговорюється як зміниться щільність осциляторів та розмір області, зайнятої осциляторами.

Ключові слова: надвипромінювання рухомих осциляторів, зсув максимуму поля в об'ємі, зміна густини осциляторів

7.379 % POWER CONVERSION EFFICIENCY OF A NUMERICALLY SIMULATED SOLID STATE DYE SENSITIZED SOLAR CELL WITH COPPER (I) THIOCYANATE AS A HOLE CONDUCTOR[†]

 Eli Danladi^{a,*}, Muhammad Kashif^b,  Thomas O. Daniel^c, Christopher U. Achem^d, Matthew Alpha^e, Michael Gyan^f

^aDepartment of Physics, Federal University of Health Sciences, OtuKpo, Benue State, Nigeria

^bSchool of Electrical Automation and Information Engineering, Tianjin University, Tianjin 300072, China

^cDepartment of Physics, Alex Ekwueme Federal University, Ndufu Alike, Ebonyi State, Nigeria

^dCentre for Satellite Technology Development-NASRDA, Abuja, Nigeria

^eDepartment of Physics, Nigerian Army University, Biu, Borno State, Nigeria

^fDepartment of Physics, University of Education, Winneba, Ghana

*Corresponding Author: Email: danladielibako@gmail.com, tel.: +2348063307256

Received May 27, 2022; accepted June 20, 2022

Sourcing for alternative to liquid electrolyte in dye sensitized solar cells (DSSCs) have been the subject of interest in the photovoltaic horizon. Herein, we reported by means of simulation, the performance of dye sensitized solar cell by replacing liquid electrolyte with a copper (I) thiocyanate (CuSCN) hole conductor. The study was carried out using Solar Capacitance Simulation Software (SCAPS) which is based on poisson and continuity equations. The simulation was done based on a n-i-p proposed architecture of FTO/TiO₂/N719/CuSCN/Pt. Result of the initial device gave a Power Conversion Efficiency (PCE), Fill Factor (FF), Short Circuit Current Density (Jsc) and Open Circuit Voltage (Voc) of 5.71 %, 78.32 %, 6.23 mAcm⁻², and 1.17 V. After optimizing input parameters to obtain 1×10⁹ cm⁻² for CuSCN/N719 interface defect density, 280 K for temperature, 1.0 μm for N719 dye thickness, 0.4 μm for TiO₂ thickness, Pt for metal back contact, and 0.2 μm for CuSCN thickness, the overall device performance of 7.379 % for PCE, 77.983 % for FF, 7.185 mAcm⁻² for Jsc and 1.317 V for Voc were obtained. When compared with the initial device, the optimized results showed an enhanced performance of ~ 1.29 times, 1.15 times, and 1.13 times in PCE, Jsc and Voc over the initial device. The results obtained are encouraging and the findings will serve as baseline to researchers involved in the fabrication of novel high-performance solid state DSSCs to realize its appealing nature for industry scalability.

Keywords: ssDSSC, Copper thiocyanate, Hole Conductor, SCAPS

PACS: 41.20.Cv; 61.43.Bn; 68.55.ag; 68.55.jd; 73.25.+i; 72.80.Tm; 74.62.Dh; 78.20.Bh; 89.30.Cc

INTRODUCTION

Issues linked to energy have drawn much research interest due to environmental impact and use of resources that cannot be replenished. Between 80 to 85 % of the global energy used today, comes from fossil fuels which its exploitation results to emission of dangerous pollutants such as nitrous oxide, hydrofluorocarbon, sulfur hexafluoride, carbon dioxide and volatile organic compounds, which has capacity to jeopardize future ecosystem. Photovoltaic has been seen as a promising renewable energy technology that has the ability of converting energy from the sun into electricity with enormous strength to solving problem connected to energy. Since after the report of O'Regan and Grätzel on efficient DSSC [1] based on nanostructured TiO₂ and iodide/tri-iodide (I⁻/I³⁻) redox specie, it has continued to gained attention of global researchers as a potential alternative to widely known silicon solar cell technology. This class of solar cell belongs to the third generation of photovoltaics and has the advantages of simpler production techniques, used of eco-friendly materials and cost effectiveness as compared with its counterpart [2,3].

The DSSC is made up of self-assembled mono-layer of dye in between the wide band gap, otherwise called the electron transport layer and the liquid mediator called the electrolyte [4,5]. However, liquid electrolyte is violent to the surrounding environment it operates which results to corrosive, photo-reactive, and highly volatile nature that affects the sealing status of the DSSCs and consequently, the effect of short-term performance and poor durability of the device is noticed [6]. Sourcing alternative to this liquid electrolyte have been the subject of interest in the photovoltaic horizon [7-9]. The solution to the aforementioned challenges is to replace the liquid electrolyte with solid state p-type semiconductor, this will take care of the leakage, heavy weight and architectural complexity.

The structure of a solid-state dye sensitized solar cell is depicted in Figure 1 [10], which shows its working principle. The dye absorbs photon energy, and then promote electron to the conduction band of the dye, and subsequently the electrons are transferred to the conduction band of the TiO₂. The dye that has lost electron regenerates through the process of hole injection from hole transport material. The electrons promoted to the TiO₂ conduction band flow through the network and are collected at the FTO and the holes within the hole transport material are collected at the counter electrode.

[†] Cite as: E. Danladi, M. Kashif, T.O. Daniel, C.U. Achem, M. Alpha, and M. Gyan, East Eur. J. Phys. 3, 19 (2022), <https://doi.org/10.26565/2312-4334-2022-3-03>

© E. Danladi, M. Kashif, T. O. Daniel, C.U. Achem, M. Alpha, M. Gyan, 2022

The solid-state semiconductor which are used in solid state dye solar cells and serves as replacement of liquid electrolytes evolved into three categories: organic, inorganic and carbonaceous. The three categories should have three main features which include: (1) their highest unoccupied molecular orbital and lowest unoccupied molecular orbital levels should be patterned in such a way as to match the highest occupied molecular orbital level of the dye and the conduction band of the TiO₂ to enhance the ability of charge transport [11], (2) the nature of the HTM must be amorphous, this is because TiO₂ pores filling is difficult with crystalline HTMs [11,12], (3) the mobility of the holes in the hole conductor should be high [13]. A quite number of p-type semiconductors have shown good ability to act as hole transport material in solar cell devices, which include, silicon carbide (SiC), copper iodide (CuI), Nickel oxide (NiO), copper thiocyanate (CuSCN), gallium nitride (GaN), 2,2'-7,7'-tetrakis (N,N-di-p-methoxyphenyl-amine) 9,9'-spirobifluorene (spiro-OMeTAD), poly(3,4-ethylenedioxythiophene):polystyrene sulfonate (PEDOT: PSS) to mention but a few [10,11,14,15].

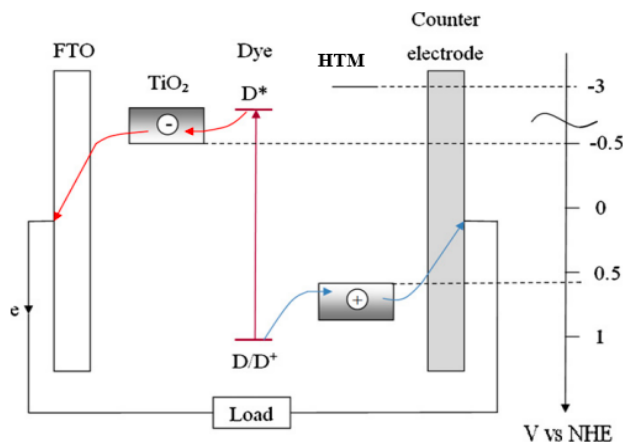


Figure 1. Schematic of a solid-state dye sensitized solar cell [10]

However, among the listed of them all, CuSCN has shown good prospect due to its display of extraordinary stability as a result of polymeric nature properties from the solid [15,16]. It was demonstrated by Perera and Tennakone [17], that it is often difficult for CuSCN to decompose into SCN⁻¹, and by means of stoichiometric, SCN⁻¹ does not result to surface trapping in CuSCN, which makes devices developed with CuSCN has minimal recombination and high stability [18].

In this paper, a simulation studies on dye sensitized solar cell was carried out by replacing liquid electrolyte with CuSCN inorganic salt as HTM. The results demonstrate that, CuSCN is an alternative to liquid based electrolyte and this is projected to serve as a baseline for researchers involved in fabrication and design of high efficient dye-based solar cells with durable properties.

SIMULATION USING SCAPS

We employed the use of Solar Cell Capacitance Simulator Software in one Dimension (SCAPS-1D) to model and simulate the solid state dye sensitized solar cells. The software basically works on two basic semiconductor equations, which include, the poisson equation and the continuity equation of electrons and holes under steady-state condition [19]. The SCAPS-1D was used under the air mass (AM 1.5G) at 100 mWm⁻² and temperature of 300 K to obtain the current-voltage (J-V) photovoltaic characteristics of ssDSSCs. The planar heterojunction n-i-p cell structure was employed in the study with architecture of FTO/TiO₂/N719/CuSCN/Pt as shown in Figure 2. The data used for the simulation were obtained from literatures and listed in Table 1 with sources duly acknowledged. The front and back contacts are fluorine tine oxide and platinum with work functions of 4.4 eV and 5.65 eV. The defect interface for the CuSCN/N719 are as shown in Table 2.

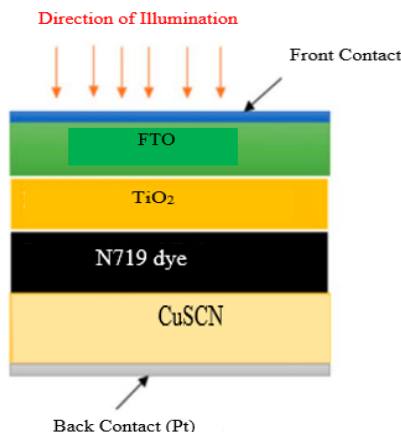


Figure 2. Device structure of the n-i-p solid state dye sensitized solar cell.

Table 1. Parameters used for simulation of perovskite solar cell structures using SCAPS-1D [11,18,20],

Parameters	FTO	TiO ₂	N719	CuSCN
Thickness (μm)	0.4	0.05	0.6	0.2
Band gap energy E_g (eV)	3.5	3.2	2.33	3.6
Electron affinity χ (eV)	4.0	4.2	3.9	1.7
Relative permittivity ϵ_r	9.0	10	30	10
Effective conduction band density N_c (cm^{-3})	2.2×10^{18}	2.2×10^{18}	2.4×10^{20}	1×10^{21}
Effective valance band density N_v (cm^{-3})	2.2×10^{18}	2.2×10^{18}	2.5×10^{20}	1×10^{21}
Electron mobility μ_n ($\text{cm}^2 \text{V}^{-1} \text{s}^{-1}$)	20	20	5.0	100
Hole mobility μ_p ($\text{cm}^2 \text{V}^{-1} \text{s}^{-1}$)	10	10	5.0	25
Donor concentration N_D (cm^{-3})	1×10^{19}	1×10^{17}	0	0
Acceptor concentration N_A (cm^{-3})	0	0	1×10^{17}	1×10^{17}
Defect density N_t (cm^{-3})	1×10^{15}	1×10^{13}	1×10^{15}	1×10^{22}

Table 2. Parameters of interface layer [11,18]

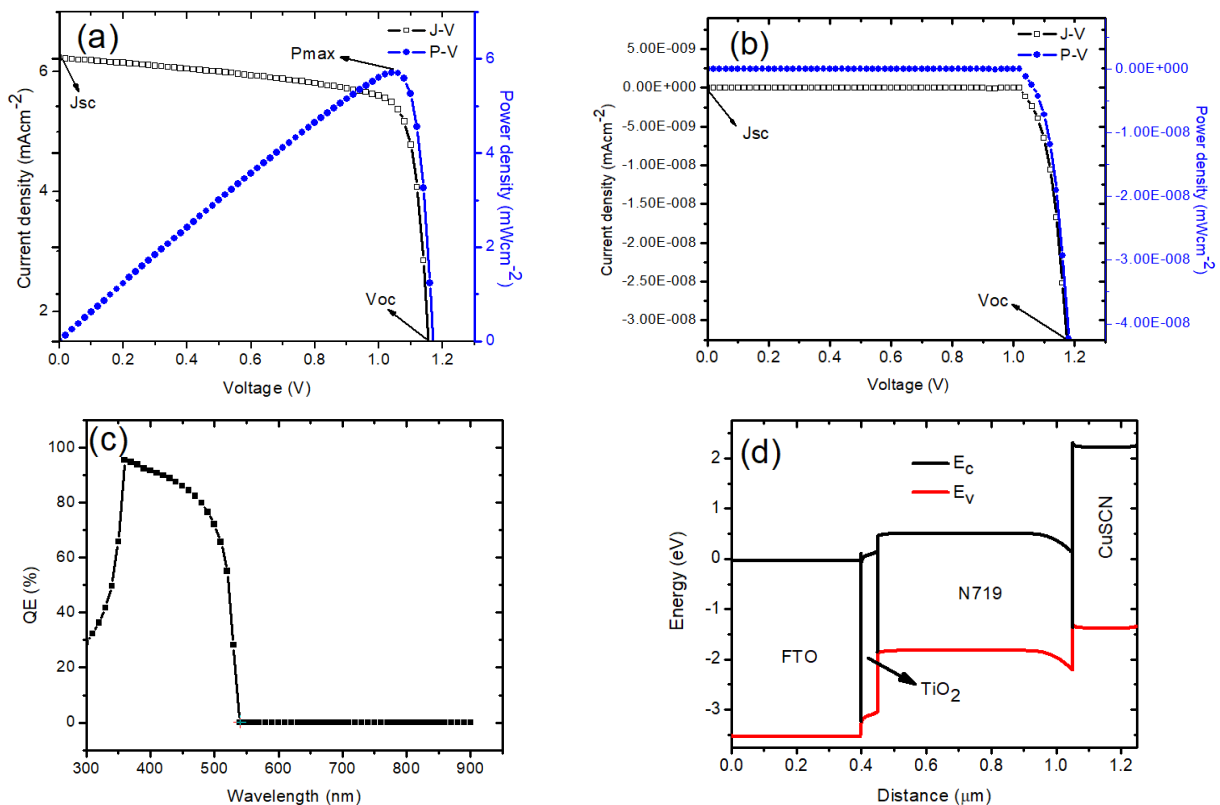
Parameters	CuSCN/N719 dye
Defect type	Neutral
Capture cross section for electrons (cm^2)	1×10^{-19}
Capture cross section for holes (cm^2)	1×10^{-19}
Energetic distribution	Single
Energy level with respect to E_v (eV)	0.1
Characteristic energy (eV)	0.650
Total density (cm^{-3})	1×10^{12}

RESULTS AND DISCUSSIONS

Current-voltage and Quantum Efficiency Characteristics of initial device

The current voltage plot demonstrates the characteristic pattern that is often used for determination of photovoltaic performance parameters of the power output of a solar device. The J-V plot of our simulated device under light illumination is as shown in Figure 3(a).

The studies under standard photovoltaic performance results to J_{sc} of 6.23 mAcm^{-2} , V_{oc} of 1.17 V, FF of 78.32 and PCE of 5.71 %. As shown in Figure 3(b), the J-V characteristics without illumination is a diodic behavior, where no current is flowing and demonstrates a rectifying characteristics.

**Figure 3.** (a) J-V & P-V curve of initial device under illumination, (b) J-V & P-V curve of initial device in the dark, (c) QE curve of the device with respect to wavelength and (d) Energy band diagram of the device

The Voc of the ssDSSC device is the voltage through which current flows in the circuit when the polarities of the device are not in touch. This is the favourable voltage generated by the ssDSSC device. The dependency relationship that exist between Voc, Jsc is shown in equation 1. The Jsc here is the current generated by the ssDSSC device under illumination when the device is short-circuited. The FF is the ratio between product of maximum current and voltage to the product of Voc and Jsc of the ssDSSCs as shown in equation 2. The quality of the simulated ssDSSC is described in terms of this parameter [20]. The PCE of the ssDSSC is obtained as the ratio of maximum power (P_{max}) and incident power (P_{in}) as expressed in equation 3.

$$V_{oc} = \frac{nK_B T}{q} \ln \left[\frac{J_{sc}}{J_o} + 1 \right] \quad (1)$$

$$FF = \frac{P_{max}}{J_{sc} \times V_{oc}} = \frac{J_{mp} \times V_{mp}}{J_{sc} \times V_{oc}} \quad (2)$$

$$PCE = \frac{P_{max}}{P_{in}} = \frac{V_{oc} \times J_{sc} \times FF}{P_{in}} \times 100\% \quad (3)$$

When we compare our simulated result with obtained experimental result reported by Premalal et. al [21], using same ETM, HTM and dye, there was improved performance in our result of ~ 1.81, ~ 1.88 and ~ 1.35 times in Voc, FF and PCE (see Table 3). Their ssDSSC device gave a record value of PCE=4.24 %, Jsc=15.76, Voc=0.647 and FF=41.60 %. The differences are due to low conductivity in CuSCN as a result of carbon paste as metal back contact as against the Pt back contact reported in our study. There was also an overlap behaviour of hole diffusion in the bulk CuSCN and charge transfer at the CuSCN/carbon interface which result to recombination at the TiO₂/CuSCN interface. At the CuSCN/Pt, charge transfer resistance is lowered and reactive surface area is extended [21]. Further comparison with ssDSSC simulated with ZnO as ETM, N719 as dye, CuSCN as HTM and Au as metal back contact gave photovoltaic parameters close to those reported in our studies [18] as shown in Table 3.

Table 3. Photovoltaic parameters obtained from simulation compared to experimental data

Parameters	Experimental [21]	Simulated [18]	Present Study
Jsc	15.760	8.563	6.23
Voc	0.647	0.885	1.17
FF	41.600	70.940	78.32
PCE	4.240	5.380	5.71

Quantum efficiency (QE) is one of the crucial characteristic of solar cell which is the ratio of the electron-hole pairs collected to the number of striking photons [11,22]. QE is seen as a function of wavelength in nm or photon energy in eV. Equation 4 expresses the relationship between QE and current density.

$$J_{sc} = q \int \phi(\lambda) QE(\lambda) d\lambda \quad (4)$$

Where, $\phi(\lambda)$ is the energy intensity per wavelength (λ) bandwidth unit. Figure 3(c), shows the quantum efficiency versus wavelength for the simulated ssDSSC device, which explains how photon energy is transformed into electricity as a function of wavelengths [23]. The curve was within the wavelength range of 300-900 nm. The QE of the ssDSSC increased from 30.42 % at 300 nm to a maximum of 96.2 % at 356 nm but gradually decreases to 0.16 % at a wavelength value of 540 nm. As seen from our study, it is worthy of note to know that energy losses as a result of exciton quenching is experienced beyond 540 nm. The device can absorb sufficient photon energy within visible region to be converted to electricity, however at longer wavelength, the QE decreases gradually. Consequently, at ~ 540 nm, ssDSSC device becomes weakly efficient to absorb photon energy due to limited ability to harvest photon energy at extended wavelength due to high rate of carrier recombination [18]. Figure 3(d) shows the energy band structure of the device. The interface conduction and valence band offset at the TiO₂/N719 and N719/CuSCN interfaces are $\Delta E_c=0.33$ eV, $\Delta E_v=1.22$ eV and $\Delta E_c=2.08$ eV, $\Delta E_v=0.81$ eV. The value of ΔE_c at the TiO₂/N719 interface prevents the flow of electrons from the TiO₂ layer to N719 dye to avoid recombination. While the value of ΔE_v at the N719/CuSCN interface denies the flow of holes to the metal-back contact to prevent their recombination at the CuSCN layer. These values obtained are crucial in determining high PCE by encouraging sufficient collection of charge carriers.

Effect of CuSCN/N719 defect

The interface defect density between the hole conductor CuSCN and the absorbing dye was varied from 10⁹ cm⁻² to 10¹³ cm⁻² while keeping other parameters constant during the simulation. The PCE, Jsc and Voc were significantly affected by increase in interface density. The PCE, Jsc and Voc decrease from 6.94 to 5.70 %, 6.87 to 6.22 mAcm⁻² and 1.31 to 1.17 V (see Table 4). Surprisingly, Voc remains constant above 10¹² cm⁻². Once such a threshold is attained,

further increase in interface defect density does not affect the V_{oc} because carrier generation occurs very close to that point and shows maximum carrier saturation. This is in agreement with previous report by Devi et al. [24], that is linked to high trapping sites and results to possible recombination with increase in defect density and also in accordance with reported literatures [18,25]. We can speculate from our result that, interface defect density has an inverse relationship with PV performance, which means that, increasing defect in the CuSCN/dye interface of ssDSSC results to reduction in diffusion length [18]. Figure 4(a), (b) and (c), show the relationship that exist between current and voltage, QE and wavelength and between power density and open circuit voltage. The QE rises steadily from 29.5 % at 300 nm to 99, 98, 97, 95 and 94 % with increase in interface defect density at 360 nm before it fell back with QE of 0.44 % at 540 nm. This exhibits good agreement in conformity to similar studies by Korir et al. [18]. Figure 4(c) expresses the maximum power ranging from 5.70 to 6.94 mWcm^{-2} .

Table 4. Photovoltaic parameters with varied CuSCN/dye defect interface

Interface defect	PCE	FF	Jsc	Voc
1×10^9	6.94	77.03	6.87	1.31
1×10^{10}	6.26	77.64	6.56	1.23
1×10^{11}	5.80	78.08	6.29	1.18
1×10^{12}	5.71	78.32	6.23	1.17
1×10^{13}	5.70	78.36	6.22	1.17

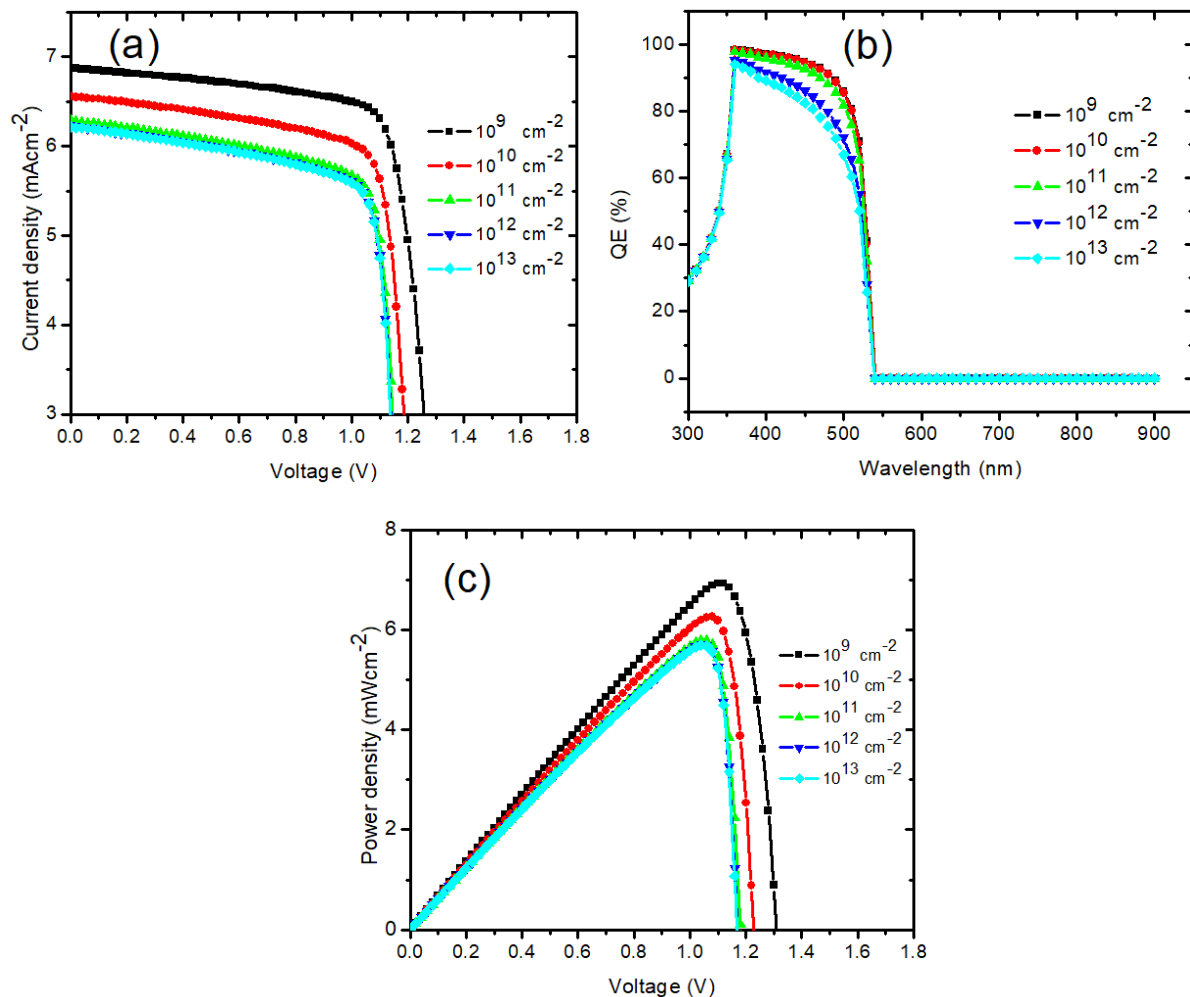


Figure 4. (a) J-V plots with varied CuSCN/dye defect density, (b) QE versus wavelength with varied CuSCN/dye defect density and (c) P-V plots with varied CuSCN/dye defect density

Effect of Temperature

The temperature with which a given solar cell operates is crucial in determining the device output performance [11,18]. The working temperature of the simulated ssDSSC device was varied from 270 K to 340 K with all other parameters constant. As depicted in Table 5, the photovoltaic performance of ssDSSC is affected by the temperature. Increasing the temperature from 270 K to 340 K results to dramatic decrease in PCE and V_{oc} . Similar trend was reported by other researchers [11,18,26-29]. This could be attributed to the fact that, at higher temperature, the electrons in the

device absorbs sufficient energy and quickly becomes unstable and subsequently result to recombination before they reach the depletion region and thereby prompt the reduced solar PCE [11,27]. The decrease in PV parameters with increasing temperature can be further explained thus: the band gap of semiconducting materials decreases when temperature is high and Voc has a direct relationship with bandgap, so Voc decreases with increasing temperature, as such, the efficiency also decreases simultaneously with increase in temperature [28,29]. Surprisingly, the fill factor and Jsc were increased with temperature increase which demonstrates an inverse relationship between the parameters. The Jsc gradually increase from 6.218 to 6.232 mAcm⁻², which is attributed to improved generation of charge carriers and reduced bandgap which results to excitonic quenching of carriers at the heterojunction barrier when the thermal activation energy increases [18,30,31]. Figure 5(a) shows the J-V characteristic curve with different temperature. The correlation between PCE and FF and between Jsc and Voc is depicted in Figures 5(b) and (c). Table 5 summarized the photovoltaic performance with varied temperature.

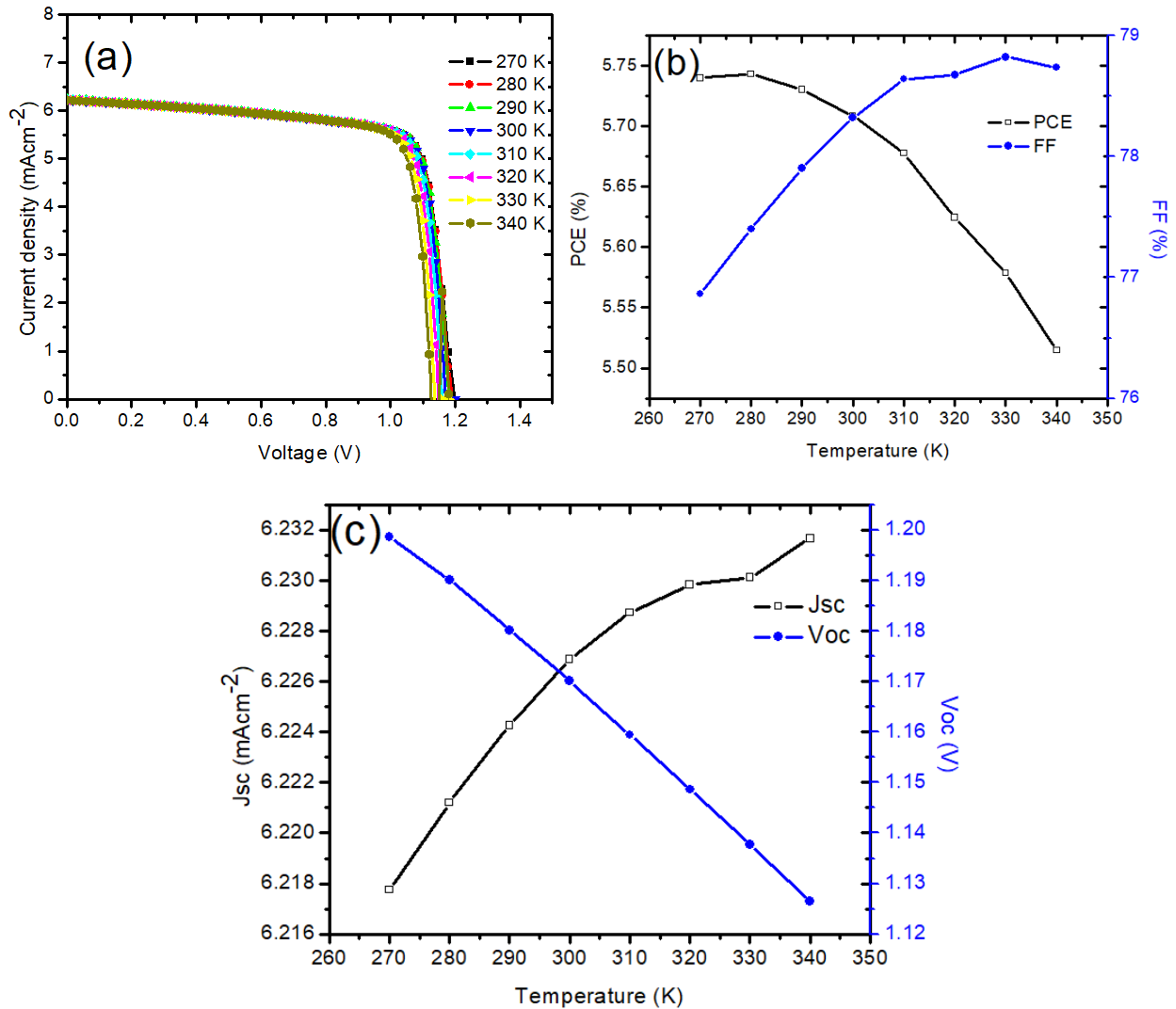


Figure 5. (a) J-V curve with varied temperature, (b) PCE and FF correlation with temperature and (c) Jsc and Voc correlation with temperature

Table 5. Photovoltaic parameters with varied temperature

Temp (K)	PCE	FF	Jsc	Voc
270	5.74	76.86	6.218	1.20
280	5.74	77.40	6.221	1.19
290	5.73	77.90	6.224	1.18
300	5.71	78.32	6.227	1.17
310	5.68	78.64	6.229	1.16
320	5.62	78.67	6.230	1.15
330	5.58	78.82	6.231	1.14
340	5.51	78.74	6.232	1.13

Effect of dye thickness

Photosensitizer is a crucial material in determining the metrics of ssDSSC. The dye used in this simulation study is a N719 dye. The dye thickness was varied from 0.2 μm to 1.0 μm (see Figure 6(a)).

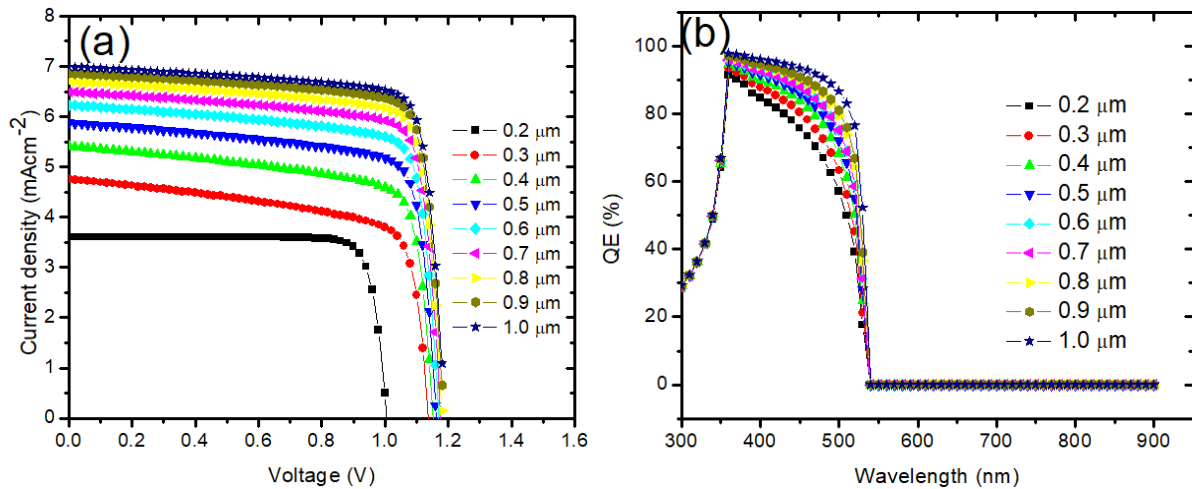


Figure 6. (a) J-V curve with varied N719 dye thickness, (b) QE versus wavelength with varied N719 dye thickness

The N719 dye molecule harvest the energy from the sun and convert it into electrical energy at the junction [18,31]. For the dye to meet its requirements in ssDSSC, it should be able to harvest light at the visible and near infrared region of electromagnetic spectrum [18,32,33]. The thickness of dye pigment has significant effect on metric parameters (PCE, FF, Jsc and Voc) of the solar cell device. Table 6 shows the dependency of PCE, FF, Jsc and Voc with N719 dye thickness.

Table 6. Photovoltaic parameters with varied N719 dye thickness

Thickness	PCE	FF	Jsc	Voc
0.2	3.076	68.367	3.601	1.117
0.3	3.805	71.285	4.757	1.138
0.4	4.634	74.361	5.407	1.153
0.5	5.252	76.835	5.879	1.163
0.6	5.710	78.319	6.230	1.170
0.7	6.062	79.372	6.493	1.176
0.8	6.344	80.180	6.697	1.181
0.9	6.566	80.716	6.858	1.186
1.0	6.743	81.082	6.987	1.190

All photovoltaic parameters increased drastically with increase in thickness of the N719 dye. The PCE was increased from 3.076 % to 6.743 %, the FF improved from 68.367 to 81.082 %, Jsc increased from 3.601 mAcm^{-2} to 6.987 mAcm^{-2} and Voc increased from 1.117 V to 1.190 V. The increase observed in the parameters was as a result of generation of many electron-hole (e-h) pairs due to sufficient dye adsorption on the surface of the TiO_2 nano material that promote electron into conduction band of the semiconductor linked to the device [18,33]. When the thickness is low, there is incomplete absorption of photons due to poor adsorption on the semiconductor surface, as a result, some of the unabsorbed surface act as recombination centres leading to electron transport resistance which consequently leads to poor device performance. Figure 6(b) shows the relationship between QE and wavelength. The QE increases gradually from 28.90 % at 300 to 97.93 % at 356 nm and starts decreasing to 1.03 % at 540 nm. The sweeping is within the visible region which is a satisfied condition for light harvesting material in our simulation. Figures 7(a-d), show the metric parameters dependence with thickness of the dye. The optimum performance was with device with 1.0 μm thickness, which demonstrates a PCE of 6.743 %, FF of 81.082 %, Jsc of 6.987 mAcm^{-2} and Voc of 1.190 V.

Effect of TiO_2 thickness

Several researchers have reported the influence of TiO_2 thickness on the performance of solar cells [11,34,35]. To show the influence of the TiO_2 thickness on PV parameters, we varied the thickness from 0.1 μm to 0.8 μm . Figure 8 shows the J-V curve of the simulation with different thickness. Figures 9(a-d) show the correlation between the performance parameters and the TiO_2 thickness. As shown in Table 7, the PCE increased from 5.705 to 5.743 % at thickness of 0.1 μm to 0.4 μm . Beyond 0.4 μm , the device performance degrades which can be explained thus: the thicker the TiO_2 , the higher the surface adsorption between the dye and the semiconductor and the more its photon absorption capability. Literature has reported a direct proportionality existing between dye adsorption of TiO_2 and the TiO_2 thickness

(i.e. the more the thickness of TiO₂, the more the bonding formation it has with dye) [36]. The optimized thickness is 0.4 μm which gave a PCE value of 5.743 %. The J_{sc} was also higher at the same thickness. The improved J_{sc} (6.121 mAcm⁻²) was due to enhanced dye anchorage with the thicker TiO₂. Beyond the 0.4 μm thickness of TiO₂, the PCE and J_{sc} decreases, which is attributed to lower transmittance that limit solar radiance on the dye and it is in agreement with previously reported document [37].

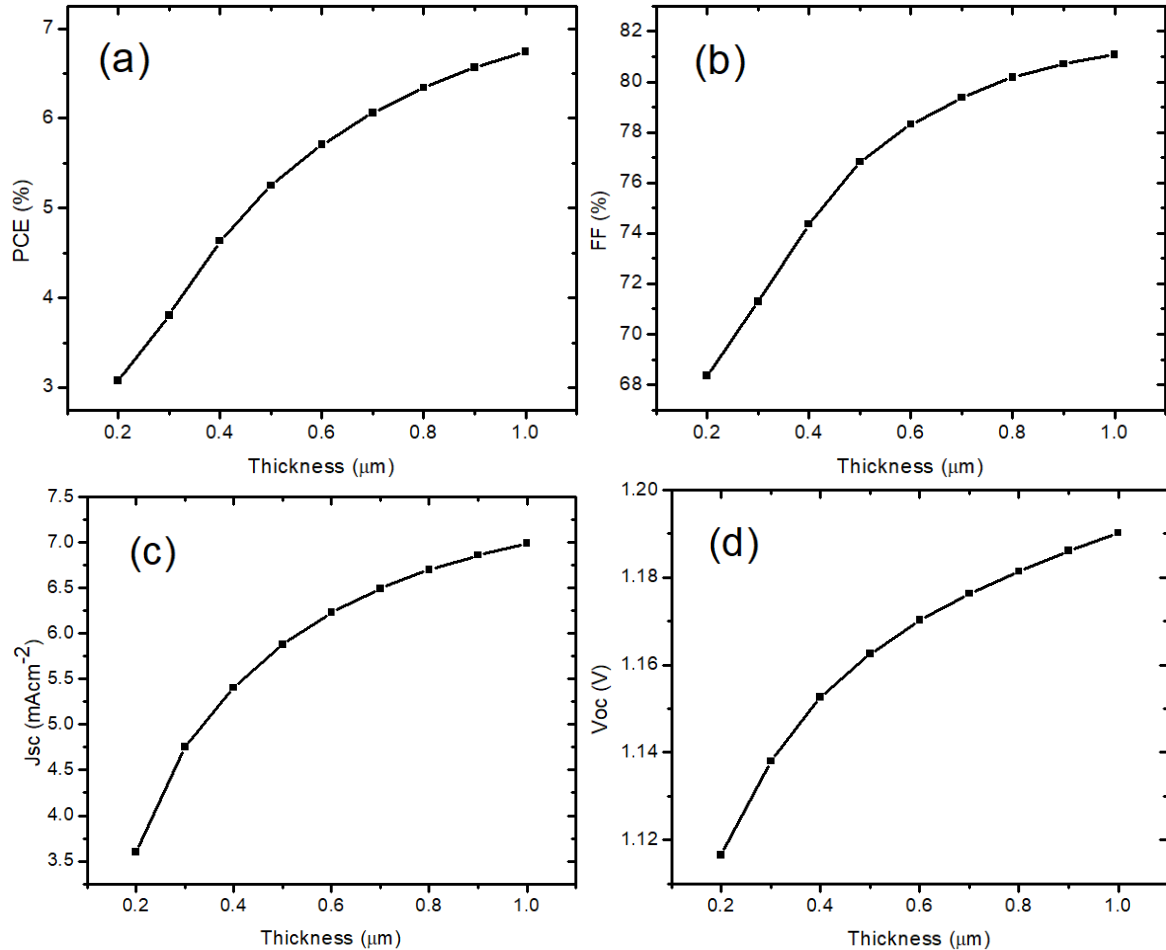


Figure 7. variation of (a) PCE, (b) FF, (c) J_{sc} and (d) Voc with thickness of N719 dye

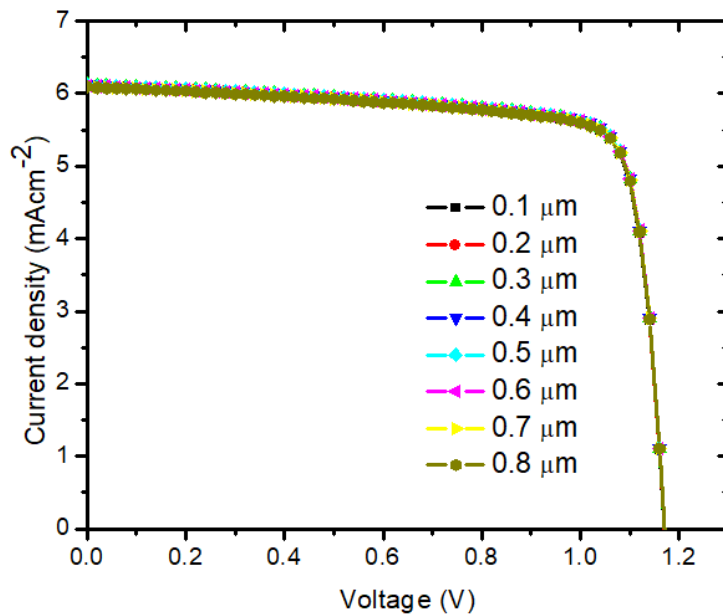


Figure 8. J-V curves with variation of thickness of TiO₂

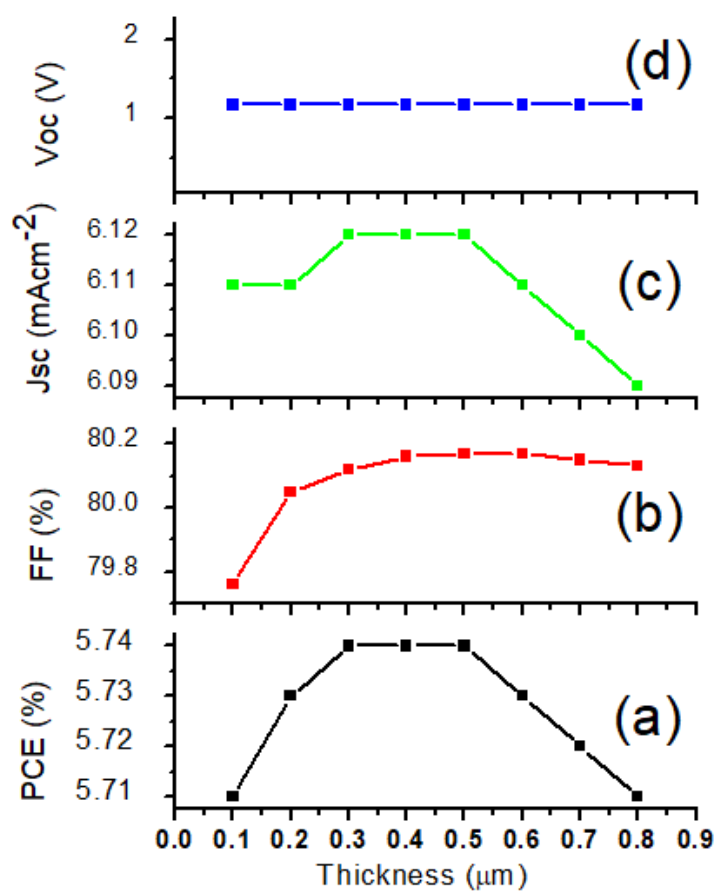


Figure 9. variation of (a) PCE, (b) FF, (c) Jsc and (d) Voc with thickness of TiO₂

Table 7. Photovoltaic parameters with varied TiO₂ thickness

Thickness	PCE	FF	Jsc	Voc
0.1	5.7054	79.7597	6.112232	1.170321
0.2	5.7273	80.0494	6.112714	1.170455
0.3	5.7392	80.1239	6.119313	1.170540
0.4	5.7433	80.1602	6.120635	1.170592
0.5	5.7412	80.1719	6.117325	1.170621
0.6	5.7340	80.1680	6.109958	1.170634
0.7	5.7228	80.1539	6.099061	1.170634
0.8	5.7082	80.1334	6.085118	1.170626

Effect of back contact

The photovoltaic parameters of ssDSSC is influenced by the type of metal contact used. Several metal back contacts have been reported in literatures [11,18, 30-38]. In our simulation, we made used of Ni, Au, Pd and Pt as the back contacts. Surprisingly, from our investigation, the metal back contact has no effect on the performance output of our device. This is because, by using CuSCN as hole conductor, the total internal resistances of the ssDSSCs remained unchanged as such there is no further carrier generation. The interfacial resistance at the CuSCN/metal back contact was unaffected which results to negligible ohmic contact. A report that shows negligible effect of metal contact on device was demonstrated by Behrouznejad et al. [38] where a HTM and HTM-free devices were developed. The impact was negligible in devices with HTM. Table 8 shows the comparison in the PV parameters.

Table 8. Photovoltaic parameters with different metal back contact

Parameter	PCE	FF	Jsc	Voc
Ni	5.71	78.32	6.23	1.17
Au	5.71	78.32	6.23	1.17
Pd	5.71	78.32	6.23	1.17
Pt	5.71	78.32	6.23	1.17

Figures 10(a) and (b) show the J-V and QE curves with different metal contact. Figure 11 shows the PV parameters with different back metal contact.

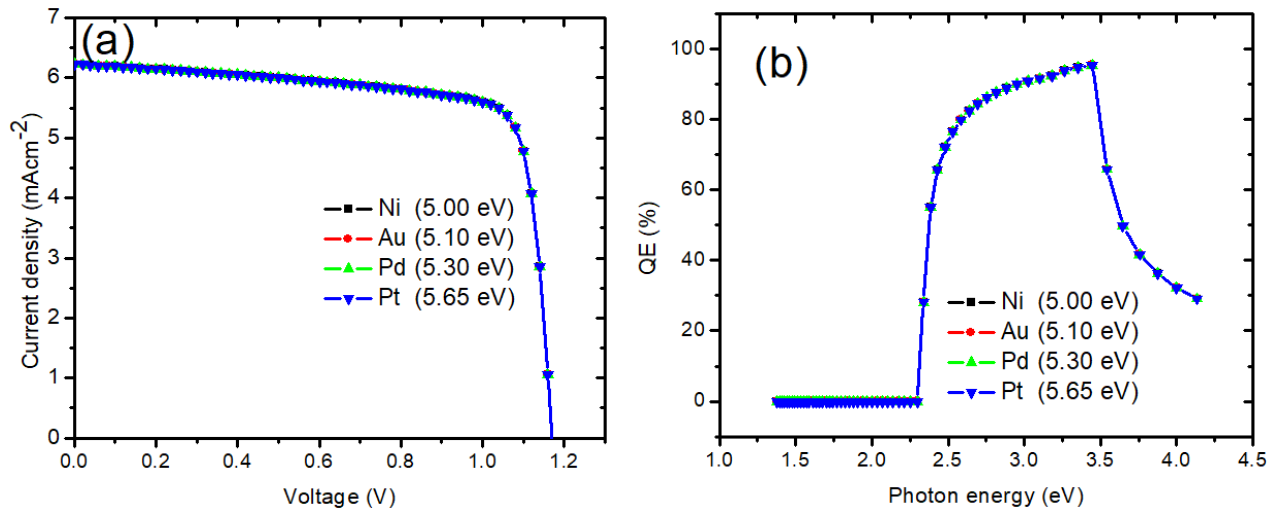


Figure 10. (a) J-V curves and (b) QE curves with different metal back contact

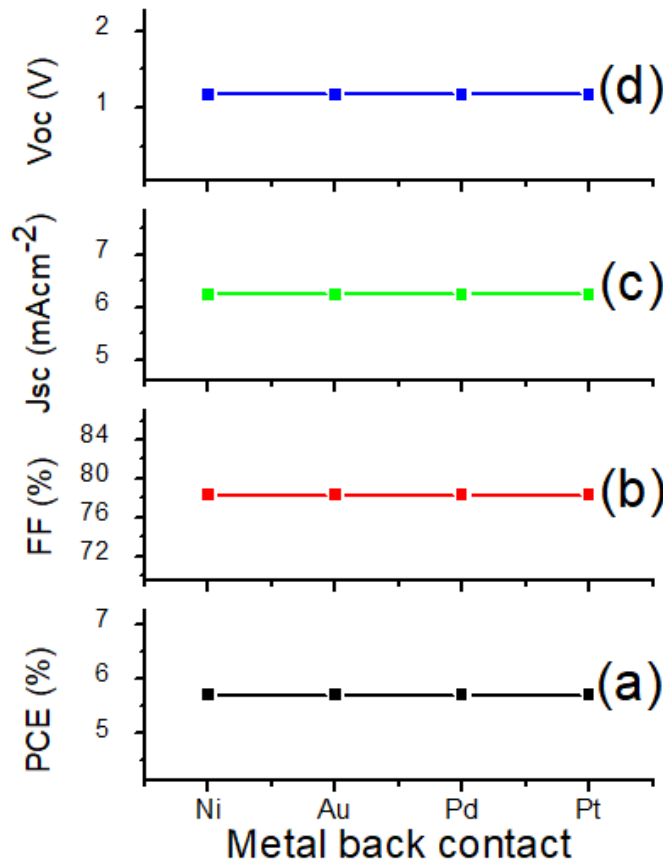


Figure 11. variation of (a) PCE, (b) FF, (c) Jsc and (d) Voc with different metal back contact

Effect of CuSCN thickness

The HTM is an important part of ssDSSCs which play a significant role in determining the performance of the overall device through photo-thermal stabilities [18]. The thickness of CuSCN was varied from 0.1 μm to 0.8 μm (see Figure 12) and the parameters; FF, PCE, Voc and Jsc were evaluated under standard photovoltaic conditions. The values of the parameters all remained unchanged throughout the simulation. The PCE = 5.71 %, FF = 78.32 %, Jsc = 6.23 mAcm⁻² and Voc = 1.17 V. The results obtained here show that, the CuSCN HTM is efficient at all thicknesses considered during the simulation and has the ability to effectively work in the proposed architecture in our simulation. Figures 13(a-d) show the relationship between the performance parameters and the CuSCN thickness.

Optimized device

The optimization was done by chosen the parameter that gave the optimum performance upon variation within a selected range. For the CuSCN/N719 interface defect density, an optimum value of $1 \times 10^9 \text{ cm}^{-2}$ was obtained, while 280 K was optimum temperature, $1.0 \mu\text{m}$ was optimum thickness for N719 dye, $0.4 \mu\text{m}$ was optimum value for TiO_2 thickness, Pt was still used as the back contact since the back contact is not affected in our simulation, and $0.2 \mu\text{m}$ for CuSCN thickness. After putting the optimized values, an overall device performance of 7.379 % for PCE, 77.983 % for FF, 7.185 mAcm^{-2} for J_{sc} and 1.317 V for V_{oc} were obtained. The optimized results showed an improved performance of $\sim 29.25 \%$, 15.36% , and 12.56% in PCE, J_{sc} and V_{oc} over the initial device.

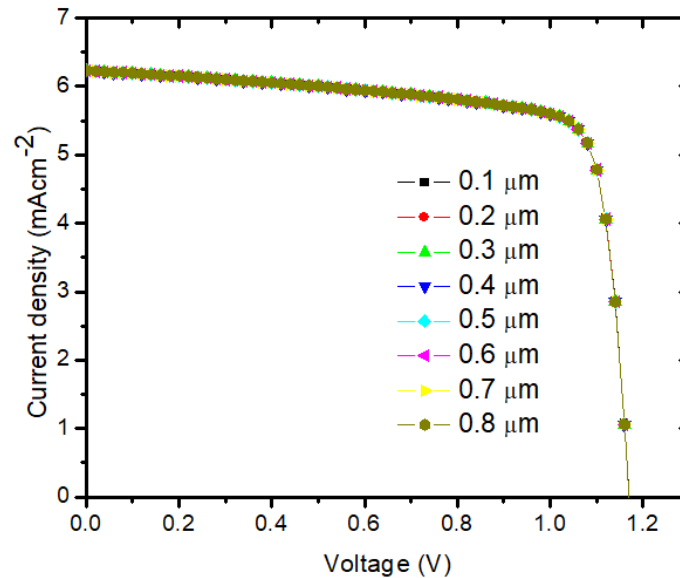


Figure 12. J-V curves with varied thickness of CuSCN

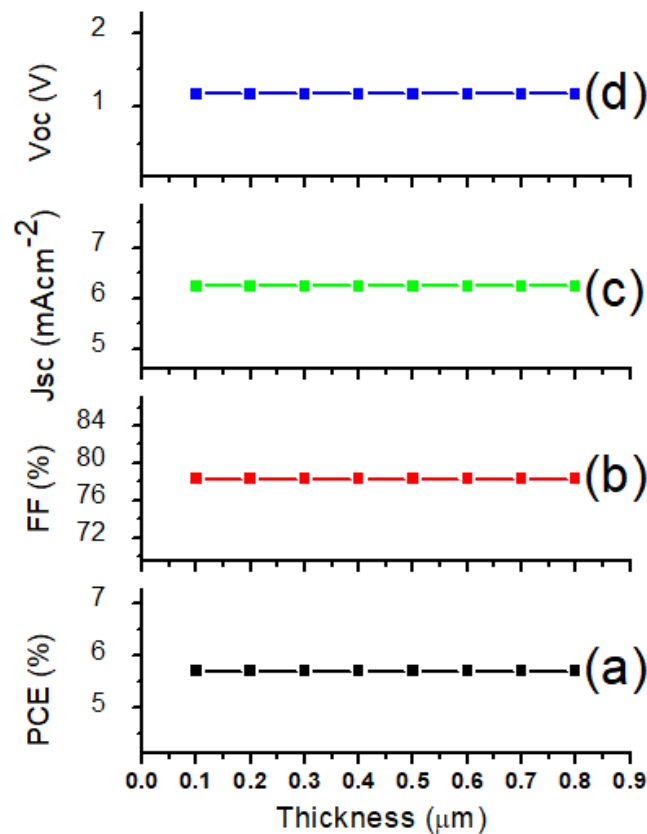


Figure 13. (a) PCE, (b) FF, (c) J_{sc} and (d) V_{oc} with different CuSCN thickness

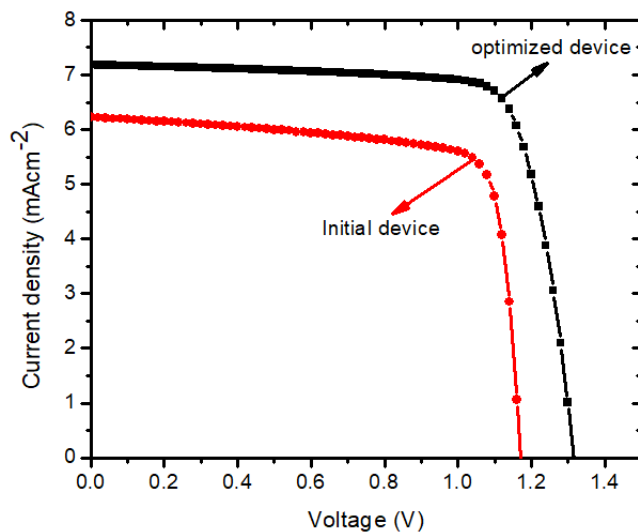


Figure 14. Combine J-V curves for the initial and optimized device

CONCLUSION

We reported the performance of a solid state dye sensitized solar cell based on CuSCN as a hole conductor using SCAPS-1D. The performance of the overall ssDSSC was achieved by optimizing the CuSCN/dye interface defect, operating temperature, CuSCN thickness, TiO₂ thickness and N719 dye thickness through data variation. The optimized device results to 7.379 % PCE, 77.983 % FF, 7.185 mAcm⁻² Jsc and 1.317 V Voc. This research suggests that, efficient stable and durable dye sensitized solar cells can be achieved by replacing liquid electrolyte with CuSCN hole conductor that is cost effective.

Acknowledgement

The authors would like to thank Professor Marc Burgelman, Department of Electronics and Information Systems, University of Gent for the development of the SCAPS software package and allowing its use.

Conflict of interest. Authors have declared that there was no conflict of interest.

Funding. This article did not receive any funding support.

ORCID IDs

©Eli Danladi, <https://orcid.org/0000-0001-5109-4690>; ©Thomas O. Daniel, <https://orcid.org/0000-0002-5176-9181>

REFERENCES

- [1] B. O'regan, and M. Grätzel, *Nature*, **353**, 737–740 (1991), <https://doi.org/10.1038/353737a0>
- [2] S. Sharma, K.K. Jain, and A. Sharma, *Materials Sciences and Applications*, **6**(12), 1145–1155 (2015), <https://doi.org/10.4236/msa.2015.612113>
- [3] V.R. Gómez, F.A. Mató, D.S. Jiménez, G.S. Rodríguez, A.Z. Lara, I.M. De Los Santos, and H.Y.S. Hernández, *Optical and Quantum Electronics*, **52**, 324 (2020), <https://doi.org/10.1007/s11082-020-02437-y>
- [4] A. Hagfeldt, G. Boschloo, L.C. Sun, L. Kloo, and H. Pettersson, *Chemical Reviews*, **110**, 6595–6663 (2010), <https://doi.org/10.1021/cr900356p>
- [5] M. Gratzel, *Accounts of Chemical Research*, **42**, 1788–1798 (2009), <https://doi.org/10.1021/ar900141y>
- [6] S. Yanagida, Y.H. Yu, and K. Manseki, *Accounts of Chemical Research*, **42**, 1827–1838 (2009), <https://doi.org/10.1021/ar900069p>
- [7] I. Chung, B. Lee, J. He, R.P.H. Chang, and M.G. Kanatzidis, *Nature*, **485**, 486–489 (2012), <https://doi.org/10.1038/nature11067>
- [8] M. Wang, N. Chamberland, L. Breau, J.E Moser, R.H. Baker, B. Marsan, S.M. Zakeeruddin, and M. Grätzel, *Nature Chemistry*, **2**, 385–389 (2010), <https://doi.org/10.1038/nchem.610>
- [9] A. Yella, H.W. Lee, H.N. Tsao, C. Yi, A.K. Chandiran, M.K. Nazeeruddin, E.W.G. Diao, C.Y. Yeh, S.M. Zakeeruddin, and M. Grätzel, *Science*, **334**, 629–634 (2011), <https://doi.org/10.1126/science.1209688>
- [10] K.H. Wong, K. Ananthanarayanan, S.R. Gajjala, and P. Balaya, *Materials Chemistry and Physics*, **125**, 553–557 (2011), <https://doi.org/10.1016/j.matchemphys.2010.10.017>
- [11] F. Jahantigh, and M.J. Saffkhani, *Applied Physics A*, **125**, 276 (2019), <https://doi.org/10.1007/s00339-019-2582-0>
- [12] L. Schmidt-Mende, S.M. Zakeeruddin, and M. Grätzel, *Applied Physics Letters*, **86**, 013504 (2005), <https://doi.org/10.1063/1.1844032>
- [13] W. Zhang, Y. Cheng, X. Yin, and B. Liu, *Macromolecular Chemistry and Physics*, **212**, 15–23 (2011), <https://doi.org/10.1002/macp.201000489>
- [14] F. Arith, O.V. Aliyaselvam, A.N.M. Mustafa, M.K. Nor, and O.A. Al-Ani, *International journal of renewable energy research*, **11**(2), 869–878 (2021), <https://www.ijrer.org/ijrer/index.php/ijrer/article/view/12046/pdf>
- [15] E.V.A. Premalal, G.R.R.A. Kumara, R.M.G. Rajapakse, M. Shimomura, K. Murakami, and A. Konno, *Chemical Communication*, **46**, 3360–3362 (2010), <https://doi.org/10.1039/B927336K>

- [16] R. Hehl, and G. Thiele, *Anorganische und Allgemeine Chemie*, **626**, 2167–2172 (2000), [https://doi.org/10.1002/1521-3749\(200010\)626:10%3C2167::AID-ZAAC2167%3E3.0.CO;2-7](https://doi.org/10.1002/1521-3749(200010)626:10%3C2167::AID-ZAAC2167%3E3.0.CO;2-7)
- [17] V. Perera, and K. Tennakone, *Solar Energy Materials and Solar Cells*, **79**(2), 249–255 (2003), [https://doi.org/10.1016/S0927-0248\(03\)00103-X](https://doi.org/10.1016/S0927-0248(03)00103-X)
- [18] B.K. Korir, J.K. Kibet, and S.M. Ngari, *Optical and Quantum Electronics*, **53**, 368 (2021), <https://doi.org/10.1007/s11082-021-03013-8>
- [19] M. Burgelman, J. Verschraegen, S. Degraeve, and P. Nollet, *Progress in Photovoltaics: Research and Applications*, **12**(2–3), 143–153 (2004), <https://doi.org/10.1002/pip.524>
- [20] D. Bartesaghi, I. del Carmen Pérez, J. Knierper, S. Roland, M. Turbiez, D. Neher, and L.J.A. Koster, *Nature Communications*, **6**(1), 1–10 (2015), <https://doi.org/10.1038/ncomms8083>
- [21] E.V.A. Premalal, N. Dematage, and A. Konno, *Chemistry Letters*, **41**, 510–512 (2012), <https://doi.org/10.1246/cl.2012.510>
- [22] A.M. Karmalawi, D.A. Rayan, and M.M. Rashad, *Optik*, **217**, 164931 (2020), <https://doi.org/10.1016/j.ijleo.2020.164931>
- [23] A.J. McEvoy, L. Castaner, T. Markvart, in: *Solar cells: materials, manufacture and operation*, (Academic Press, Amsterdam, 2013), pp. 3–25.
- [24] N. Devi, K.A. Parrey, A. Aziz, and S. Datta, *Journal of Vacuum Science & Technology B: Microelectronics and Nanometer Structures Processing, Measurement, and Phenomena*, **36**(4), 04G105 (2018), <https://doi.org/10.1116/1.5026163>
- [25] Y. Gan, X. Bi, Y. Liu, B. Qin, Q. Li, Q. Jiang, and P. Mo, *Energies*, **13**(22), 5907 (2020), <https://doi.org/10.3390/en13225907>
- [26] A.K. Daoudia, Y. El Hassouani, and A. Benami, *International Journal of Engineering and Technical Research*, **6**(2), 71–75 (2016), <https://www.academia.edu/download/54231833/IJETR042544.pdf>
- [27] U. Mehmood, A. Al-Ahmed, F.A. Al-Sulaiman, M.I. Malik, F. Shehzad, and A.U.H. Khan, *Renewable and Sustainable Energy Reviews*, **79**, 946 (2017), <https://doi.org/10.1016/j.rser.2017.05.114>
- [28] P. Roy, S. Tiwari, and A. Khare, *Results in Optics*, **4**, 100083 (2021), <https://doi.org/10.1016/j.rio.2021.100083>
- [29] S. Dubey, J.N. Sarvaija, and B. Seshadri, *Energy Procedia*, **33**, 311–321 (2013), <https://doi.org/10.1016/j.egypro.2013.05.072>
- [30] A. Shahriar, S. Hasnath, and M.A. Islam, *EDU Journal of Computer and Electrical Engineering*, **01**(01), 31–37 (2020), <https://doi.org/10.46603/ejcee.v1i1.21>
- [31] C. Xiang, X. Zhao, L. Tan, J. Ye, S. Wu, S. Zhang, and L. Sun, *Nano Energy*, **55**, 269–276 (2019), <https://doi.org/10.1016/j.nanoen.2018.10.077>
- [32] W. Cai, Z. Zhang, Y. Jin, Y. Lv, L. Wang, K. Chen, and X. Zhou, *Solar Energy*, **188**, 441–449 (2019), <https://doi.org/10.1016/j.solener.2019.05.081>
- [33] N.A. Bakr, A.K. Ali, S.M. Jassim, and K.I. Hasoon, *ZANCO Journal of Pure and Applied Sciences*, **29**(s4), s274–s280 (2017), <https://doi.org/10.21271/ZJPAS.29.s4.31>
- [34] J.M.K.W. Kumari, N. Sanjeevadarshini, M.A.K.L. Dissanayake, G.K.R. Senadeera, and C.A. Thotawatthage, *Ceylon Journal of Science*, **45**(1), 33–41 (2016), <http://dx.doi.org/10.4038/cjs.v45i1.7362>
- [35] D.L. Domtau, J. Simiyu, E.O. Ayieta, L.O. Nyakiti, B. Muthoka, and J.M. Mwabora, *Surface Review and Letters*, **24**(5), 1750065 (2017), <https://doi.org/10.1142/S0218625X17500652>
- [36] Z.S. Wang, H. Kawachi, T. Kashima, and H. Arakawa, *Coordination Chemistry Reviews*, **248**, 1381–1389 (2004), <https://doi.org/10.1016/j.ccr.2004.03.006>
- [37] M.C. Kao, H.Z. Chen, S.L. Young, C.Y. Kung, and C.C. Lin, *Thin Solid Films*, **517**, 5096–5099 (2009), <https://doi.org/10.1016/j.tsf.2009.03.102>
- [38] F. Behrouznejad, S. Shahbazi, N. Taghavinia, H.P. Wu, and E. W-G. Diau, *Journal of Materials Chemistry A*, **4**, 13488–13498 (2016), <https://doi.org/10.1039/C6TA05938D>

**7,379 % ЕФЕКТИВНІСТЬ ПЕРЕТВОРЕННЯ ЕНЕРГІЇ ЧИСЛЕННО ЗМОДЕЛЬОВАНОГО ТВЕРДОГО
СОНЯЧНОГО ЕЛЕМЕНТУ СЕНСИБІЛІЗОВАНОГО БАРВНИКОМ З ТІОЦІАНАТОМ МІДІ (I)
У ЯКОСТІ ДІРКОВОГО ПРОВІДНИКА**

Елі Данладі^a, Мухаммад Кашиф^b, Томас О. Даніель^c, Кристофер У. Ачем^d, Метью Альфа^e, Майкл Г'ян^f

^aФізичний факультет, Федеральний університет наук про здоров'я, Отужко, штат Бенуе, Нігерія

^bШкола електричної автоматизації та інформаційної інженерії, Тяньцзіньський університет, Тяньцзінь 300072, Китай

^cФізичний факультет, Федеральний університет Алекса Еквуме, Ндуфу Аліке, штат Ебоні, Нігерія

^dЦентр розвитку супутникових технологій NASRDA, Абуджа, Нігерія

^eФізичний факультет, Нігерійський армійський університет, Біу, штат Борно, Нігерія

^fФізичний факультет, Освітній університет, Віннеба, Гана

Предметом дослідження був пошук альтернативи рідкому електроліту в сонячних елементах, сенсibilізованих барвником (DSSC), щодо фотоелектричних властивостей. Тут шляхом моделювання ми повідомили про продуктивність сонячного елемента, сенсibilізованого барвником, замінивши рідкий електроліт на дірковий провідник з мідного (I) тiоціанату (CuSCN). Дослідження проводилося за допомогою програмного забезпечення для моделювання сонячної ємності (SCAPS), яке базується на рівняннях Пуассона та безперервності. Моделювання проводилося на основі запропонованої n-i-p архітектури FTO/TiO₂/N719/CuSCN/Pt. Результат початкового пристрою дав ефективність перетворення потужності (PCE) - 78,32 %, коефіцієнт заповнення (FF) - 5,71 %, щільність струму короткого замикання (J_{sc}) - 6,23 мАсм⁻², і напругу холостого ходу (V_{oc}) - 1,17 В. Після оптимізації вхідних параметрів для отримання 1×109 см⁻² для щільності дефектів інтерфейсу CuSCN/N719, 280 К для температури, 1,0 мкм для товщини барвника N719, 0,4 мкм для товщини TiO₂, Pt для зворотного контакту металу та 0,2 мкм для товщини CuSCN, було отримано загальну продуктивність пристрою 7,379 % для PCE, 77,983 % для FF, 7,185 мАсм⁻² для J_{sc} та 1,317 V для V_{oc}. У порівнянні з початковим пристроєм, оптимізовані результати показали покращену продуктивність приблизно в 1,29 рази, 1,15 рази та 1,13 рази в PCE, J_{sc} і V_{oc} порівняно з початковим пристроєм. Отримані результати є обнадійливими, і одержані дані можуть послужити базою для дослідників, які беруть участь у виготовленні нових високопродуктивних твердотільних DSSC, щоб зрозуміти їхню привабливість для масштабованості в галузі.

Ключові слова: ssDSSC, тiоціанат міді, дірковий провідник, SCAPS

THE STUDY OF ELECTRONIC STATES OF NI AND ScI MOLECULES WITH SCREENED KRATZER POTENTIAL[†]

Etido P. Inyang^a, Effiong O. Obisung^b

^aDepartment of Physics, National Open University of Nigeria, Jabi, Abuja, Nigeria

^bDepartment of Physics, University of Calabar, Calabar, Nigeria

Corresponding author E-mail: etidophysics@gmail.com, einyang@noun.edu.ng

Received June 7, 2022; revised August 10, 2022; accepted August 14, 2022

In this study, the analytical solutions of the Schrödinger equation with the screened Kratzer potential model is solved using the well-known Nikiforov-Uvarov method. The energy spectrum and the normalized wave function with the Greene-Aldrich approximation to the centrifugal term are obtained. The energy spectrum is used to generate eigenvalues for $X^3\Sigma^-$ state of NI and $X^1\Sigma^+$ state of ScI molecules respectively. The calculated results agree excellently with the experimental data. This research finds application in chemistry, industry, molecular physics and studies on magnetocaloric effect for several molecules. Our findings also demonstrate that the approximation scheme is well suited for this potential.

Keywords: Schrödinger equation; Nikiforov-Uvarov method; screened Kratzer Potential; molecules

PACS: 31.15.-p

1. Introduction

The study of diatomic molecules and their positive ions with the Schrödinger equation (SE) over the years have attracted the interest of both experimental and theoretical scientist because of its importance in chemistry and physics [1,2]. This is because solutions of the SE contain information about the system [3]. The solutions of the SE with different diatomic potential functions have been investigated by many authors [4-6]. Also, to obtain the SE solutions different methods have been employed such as the Asymptotic iteration method (AIM) [7], Laplace transformation method [8], supersymmetric quantum mechanics (SUSYQM) [9], the Nikiforov-Uvarov (NU) method [10-15], the Nikiforov-Uvarov-Functional Analysis (NUFA) method [16], the series expansion method (SEM) [17,18], the analytical exact iterative method (AEIM) [19], the WKB approximation method [20,21] and so on.

Recently, many authors have devoted interest in investigating bound states energy of countless diatomic molecules (DMs) with a single potential function and a combined potential function [22-24]. For instance, Inyang et al. [25] used Eckart and Hellmann potential function to study some selected DMs. Also, Obogo et al. [26], investigated some selected DMs through the solution of SE with a combined potential using the NU method. Furthermore, Edet and Ikot [27] studied some DMs with Deng-Fan plus Eckart potentials. Apart from the above studies, the energies for cesium molecule, sodium dimer, nitrogen dimer, hydrogen molecules, and potassium with the improved Rosen-Morse, Morse, Tietz-Hua oscillator, and improved Poschl-Teller oscillator potentials have been calculated and the results for each molecule was seen to agree with the experimental data [28-31]. Motivated by the success of their reports, we seek to obtain the energies for $X^3\Sigma^-$ state of NI and $X^1\Sigma^+$ state of ScI molecules.

The screened Kratzer potential (SKP), proposed by Ikot et al. [32] is a molecular potential, which finds application in molecular physics and many authors have employed in literature [33-35].

The aim of this study is to obtain the solutions to the SE with the SKP and apply it to calculate the energy eigenvalues for $X^3\Sigma^-$ state of NI and $X^1\Sigma^+$ state of ScI. The SKP is of the form [32]:

$$V(p) = -\frac{A_2 e^{-\vartheta p}}{p} + \frac{A_3 e^{-\vartheta p}}{p^2}, \quad (1)$$

where ϑ is the screening parameter. The letter $A_2 \equiv 2D_e r_e$ and $A_3 \equiv D_e r_e^2$, here D_e is dissociation energy, p is radial distance and r_e is the equilibrium bond length.

2. The solutions of the SE with SKP

In this research, the NU method is adopted and the details of the NU can be found in Ref. [14].

The SE characterized by a given potential $V(p)$ reads [36]

$$\left(-\frac{\hbar^2}{2\mu} \nabla^2 + V(p) \right) \Psi_{nl}(p) = E_{nl} \Psi_{nl}(p), \quad (2)$$

[†] Cite as: E.P. Inyang, and E.O. Obisung, East Eur. J. Phys. 3, 32 (2022), <https://doi.org/10.26565/2312-4334-2022-3-04>

© E.P. Inyang, E.O. Obisung, 2022

where $\Psi_{nl}(p)$ is the Eigen functions, E_{nl} is the energy, μ is the reduced mass, \hbar is the reduced Planck's constant and p is radial distance.

Substituting Eq. (1) into Eq. (2) gives Eq. (3),

$$\frac{d^2\Psi_{nl}(p)}{dp^2} + \left[\frac{2\mu E_{nl}}{\hbar^2} + \frac{2\mu Z_2 e^{-\rho p}}{\hbar^2 p} - \frac{2\mu Z_3 e^{-\rho p}}{\hbar^2 p^2} - \frac{l(l+1)}{p^2} \right] \Psi_{nl}(p) = 0. \quad (3)$$

Equation (3), is solved with the approximation scheme (AS) proposed by Greene-Aldrich [37] to deal with the centrifugal barrier. This AS is a good approximation to the centrifugal barrier which is valid for $\rho \ll 1$, and its reads [38]

$$\frac{1}{p^2} \approx \frac{\rho^2}{(1 - e^{-\rho p})^2}. \quad (4)$$

Plugging Eq. (4) into Eq. (3), Eq. (5) is:

$$\frac{d^2\psi_{nl}(p)}{dp^2} + \left[\frac{2\mu E_{nl}}{\hbar^2} + \frac{2\mu A_2 \rho e^{-\rho p}}{\hbar^2 (1 - e^{-\rho p})} - \frac{2\mu A_3 \rho^2 e^{-\rho p}}{\hbar^2 (1 - e^{-\rho p})^2} - \frac{\rho^2 l(l+1)}{(1 - e^{-\rho p})^2} \right] \psi_{nl}(p) = 0. \quad (5)$$

We set

$$y = e^{-\rho p}. \quad (6)$$

Differentiating Eq. (6), we have Eq. (7) as,

$$\frac{d^2\Psi(p)}{dp^2} = \rho^2 y^2 \frac{d^2\Psi(y)}{dy^2} + \rho^2 y \frac{d\Psi(y)}{dy} \quad (7)$$

Putting Eqs. (6) and (7) into Eq. (5) and after some simplifications, we have:

$$\frac{d^2\Psi(y)}{dy^2} + \frac{1-y}{y(1-y)} \frac{d\Psi(y)}{dy} + \frac{1}{y^2(1-y)^2} \left[-(\varepsilon + \eta_0)y^2 + (2\varepsilon + \eta_0 - \eta_1)y - (\varepsilon + \gamma) \right] \Psi(y) = 0, \quad (8)$$

where

$$-\varepsilon = \frac{2\mu E_{nl}}{\rho^2 \hbar^2}, \quad \eta_0 = \frac{2\mu A_2}{\rho \hbar^2}, \quad \eta_1 = \frac{2\mu A_3}{\hbar^2}, \quad \gamma = l(l+1) \quad (9)$$

Linking Eq. (8) and Eq. (1) of Ref. [14], we have:

$$\left. \begin{aligned} \tilde{\tau}(y) &= 1-y; \quad \sigma(y) = y(1-y); \quad \sigma'(y) = 1-2y, \quad \sigma''(y) = -2; \\ \tilde{\sigma}(y) &= -(\varepsilon + \eta_0)y^2 + (2\varepsilon + \eta_0 - \eta_1)y - (\varepsilon + \gamma) \end{aligned} \right\} \quad (10)$$

Inserting Eq. (10) into Eq. (11) of Ref. [14], gives:

$$\pi(y) = -\frac{y}{2} \pm \sqrt{(B_1 - K)y^2 + (K + B_2)y + B_3}, \quad (11)$$

where

$$B_1 = \left(\frac{1}{4} + \varepsilon + \eta_0 \right), \quad B_2 = -(2\varepsilon - \eta_0 - \eta_1), \quad B_3 = (\varepsilon + \gamma) \quad (12)$$

We take the discriminant of Eq. (11) under the square root sign and solve for K . Here, for bound state, the negative root is taken as:

$$K = -(B_2 + 2B_3) - 2\sqrt{B_3}\sqrt{B_3 + B_2 + B_1}. \tag{13}$$

Substituting Eq. (13) into Eq. (11), Eq. (14) is gotten as,

$$\pi(y) = -\frac{y}{2} - \left[(\sqrt{B_3} + \sqrt{B_3 + B_2 + B_1})y - \sqrt{B_3} \right], \tag{14}$$

Using Eq. (10) and Eq. (13), we obtain $\tau(y)$ and $\tau'(y)$ as follows:

$$\tau(y) = 1 - 2y - 2\sqrt{B_3}y - 2\sqrt{B_3 + B_2 + B_1}y + 2\sqrt{B_3}, \tag{15}$$

$$\tau'(y) = -2 \left[1 + \sqrt{B_3} + \sqrt{B_3 + B_2 + B_1} \right], \tag{16}$$

where $\tau'(y)$ is the first derivative of $\tau(y)$. Referring to Eq. (10) and Eq. (13) of Ref. [14], we have λ_n and λ as follows:

$$\lambda_n = n^2 + \left[1 + 2\sqrt{B_3} + 2\sqrt{B_3 + B_2 + B_1} \right] n, \quad (n = 0, 1, 2, \dots), \tag{17}$$

$$\lambda = -\frac{1}{2} - \sqrt{B_3} - \sqrt{B_3 + B_2 + B_1} - (B_2 + 2B_3) - 2\sqrt{B_3}\sqrt{B_3 + B_2 + B_1}, \tag{18}$$

When linking Eqs. (17) and (18) and substituting Eq. (9), the energy equation for the SKP is gotten as:

$$E_{nl} = \frac{\mathcal{G}^2 \hbar^2 l(l+1)}{2\mu} - \frac{\mathcal{G}^2 \hbar^2}{8\mu} \left[\frac{\left(n + \frac{1}{2} + \sqrt{\left(l + \frac{1}{2} \right)^2 + \frac{2\mu D_e r_e^2}{\hbar^2}} \right)^2 + \frac{4\mu D_e r_e}{\hbar^2 \mathcal{G}} + l(l+1)}{n + \frac{1}{2} + \sqrt{\left(l + \frac{1}{2} \right)^2 + \frac{2\mu D_e r_e^2}{\hbar^2}}} \right]^2. \tag{19}$$

The wave function $\phi(y)$ and weight function $\rho(y)$ is obtain by inserting the values of $\sigma(y)$, $\pi(y)$, and $\tau(y)$ given in Eqs. (10), (14) and (15), respectively, into Eq. (3) and Eq. (9) of Ref. [14] as follows:

$$\phi(y) = y^{\sqrt{B_3}} (1-y)^{\left(\frac{1}{2} + \sqrt{B_3 + B_2 + B_1} \right)}, \tag{20}$$

$$\rho(y) = y^{2\sqrt{B_3}} (1-y)^{2\sqrt{B_3 + B_2 + B_1}}. \tag{21}$$

Putting Eqs. (10) and (21), into Eq. (2) of Ref. [14], the Rodrigues relation is written as

$$y_n = B_n y^{-2\sqrt{B_3}} (1-y)^{-2\sqrt{B_3 + B_2 + B_1}} \frac{d^n}{dy^n} \left[y^{n+2\sqrt{B_3}} (1-y)^{n+2\sqrt{B_3 + B_2 + B_1}} \right], \tag{22}$$

where B_n is the Jacobi polynomial. Hence,

$$\psi_{nl}(y) = N_{nl} y^{\sqrt{B_3}} (1-y)^{\left(\frac{1}{2} + \sqrt{B_3 + B_2 + B_1} \right)} P_n^{(2\sqrt{B_3}, 2\sqrt{B_3 + B_2 + B_1})}(1-2y), \tag{23}$$

where N_{nl} is the normalization constant, with the condition, we have:

$$\frac{N_{nl}^2}{\mathcal{G}} \int_{-1}^1 \left(\frac{1-y}{2} \right)^{2\sqrt{B_3}} \left(\frac{1+x}{2} \right)^\sigma \left[A_n^{(2\sqrt{B_3}, 2\sigma-1)}(x) \right]^2 dx = 1, \tag{24}$$

where

$$\left. \begin{aligned} X &= 1 + 2\sqrt{B_3 + B_2 + B_1} \\ X - 1 &= 2\sqrt{B_3 + B_2 + B_1} \end{aligned} \right\} \quad (25)$$

Linking Eq. (26) with Eq. (37) of Ref. [39], we obtain:

$$\int_{-1}^1 \left(\frac{1-A}{2}\right)^u \left(\frac{1+x}{2}\right)^v \left(A_n^{(2u,2v-1)}(a)\right)^2 dp = \frac{2\Gamma(u+n+1)\Gamma(v+n+1)}{n!u\Gamma(u+v+n+1)}. \quad (26)$$

Hereafter, the normalization constant is

$$N_{nl} = \left[\frac{n!2\sqrt{B_3} \vartheta \Gamma(2\sqrt{B_3} + 2\sqrt{B_3 + B_2 + B_1} + n + 2)}{2\Gamma(2\sqrt{B_3} + n + 1)\Gamma(2\sqrt{B_3 + B_2 + B_1} + n + 2)} \right]^{\frac{1}{2}}. \quad (24)$$

3. PERCENTAGE DEVIATION AND ERROR

The absolute percentage deviation is calculated using Eq. (28)

$$\sigma = \frac{100}{M} \sum \left| \frac{T_v - T_{RRR}}{T_{RRR}} \right|, \quad (28)$$

where T_{RRR} is the experimental data, T_v is the present results and M is the number of experimental data [40].

The percentage error is computed with Eq. (29)

$$err_p = \frac{\sum RD}{T_{RRR}} \times 100\% \quad (29)$$

4. RESULTS AND DISCUSSION

The energies for $X^1\Sigma^+$ state of ScI and $X^3\Sigma^-$ state of NI using Eq. (19), as well as the relative deviation (RD) of the calculated results and the experimental data are given in Table 2. The experimental data is taken from [41] as shown in Table 1. We note that the energies become larger as the quantum state increases for the two molecules, the RD for $X^3\Sigma^-$ state of NI are higher compared to the RD for $X^1\Sigma^+$ state of ScI. We deduce that the ScI is more fitted for the calculation compared to NI. Using Eq. (28), the percentage deviation (PD) for the molecules is calculated. We note that the PD for ScI is 0.015% while that of NI is 0.021%. Also, with Eq. (29), we determine the percentage error (PE) of the present results to the experimental data, the PE of the calculated result is computed and the results show that for ScI we have 0.12% while that of the NI is 0.21%. In Fig. 1, we plotted the energy spectra with the principal quantum number for the selected molecules. It was observed that as the principal quantum number increases the energy spectra of the molecules increases linearly.

Table 1. Molecular constants for electronic states of NI and ScI [41]

Molecule	μ	State	ω_e (cm^{-1})	D_e (cm^{-1})	ϑ_e (cm^{-1})	r_e (\AA)
NI	12.6114.	$X^3\Sigma^-$	604.70	0.3460	0.0031700	1.9653
ScI	33.1961	$X^1\Sigma^+$	277.18	0.7467	0.0002834	2.6078

Table 2. Comparison of the calculated energies (cm^{-1}) for $X^1\Sigma^+$ state of ScI and $X^3\Sigma^-$ state of NI with the experimental data

n	Present work	ScI [41]	Relative deviation (RD)	Present work	NI [41]	Relative deviation (RD)
0	138.4120	138.3	0.1120	301.2234	301.1	0.1234
1	414.7977	413.9	0.8976	897.0135	896.6	0.9135
2	688.1130	687.7	0.4130	1482.6617	1482.3	0.6617
3	960.1402	959.9	0.2402	2060.5594	2058.8	1.7594
4	1231.1101	1230.4	0.7101	2625.9124	2625.9	0.9124
5	1500.6044	1499.3	1.3044	3185.1171	3183.6	1.5171
6	1767.1278	1766.5	0.6278	3732.8788	3731.9	0.9788

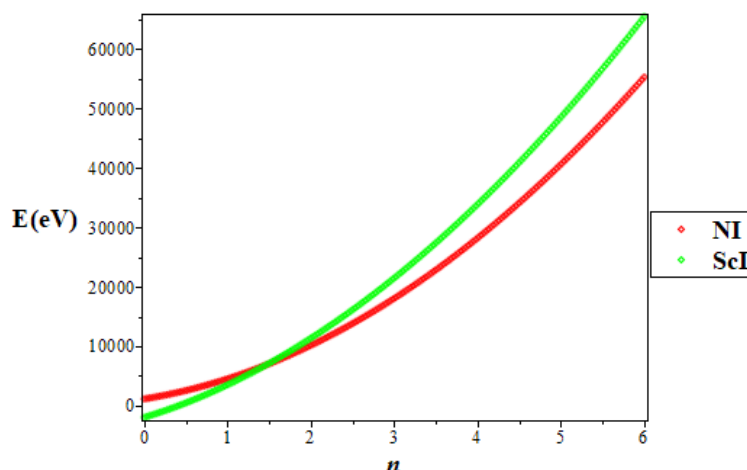


Figure 1. Variation of Energy spectra with principal quantum a number for the selected diatomic molecules

CONCLUSION

In this research, the SE with the SKP is solved using the NU method. The energy spectrum and the wave function were obtained with the Greene-Aldrich approximation to the centrifugal barrier. We then applied the energy spectrum to calculate the energies of ScI and NI molecules. The results agreed excellently with the experimental data of the two molecules. The PD shows that the SKP is fitted in the calculation of ScI than NI since the PD in ScI is lesser than that of NI molecule. This research finds application in chemistry, industry, molecular physics and studies on magnetocaloric effect for several molecules. Our findings also demonstrate that the approximation scheme is well suited for this potential.

Funding. N/A

Conflicts of interest/Competing interests. The authors declare no competing interests.

Authors' contributions. Dr. Etido P. Inyang suggested the point research and the writing of the full manuscript and Dr. Effiong O. Obisung proofread the manuscript.

ORCID ID

 **Etido P. Inyang**, <https://orcid.org/0000-0002-5031-3297>

REFERENCES

- [1] E.P. Inyang, E.P. Inyang, J. Kamiliyus, J.E. Ntibi, and E.S. William, "Diatomic molecules and mass spectrum of Heavy Quarkonium system with Kratzer-screened Coulomb potential (KSCP) through the solutions of the Schrodinger equation", *European Journal of Applied Physics*, **3**, 55 (2021), <https://doi.org/10.24018/ejphysics.2021.3.2.61>
- [2] R. Horchani, H. Jelassil, A.N. Ikot, and U.S. Okorie, "Rotation vibration spectrum of potassium molecules via the improved generalized Poschl-Teller oscillator, International", *Journal of Quantum Chemistry*, **121**(7), e26558 (2020), <https://doi.org/10.1002/qua.26558>
- [3] E. Omugbe, O.E. Osafire, I.B. Okon, E.P. Inyang, E.S. William, and A. Jahanshir, "Any *l*-state energy of the spinless Salpeter equation under the Cornell potential by the WKB Approximation method: An Application to mass spectra of mesons", *Few-Body Systems*, **63**, 7 (2022), <https://doi.org/10.1007/s00601-021-01705-1>
- [4] A.N. Ikot, C.O. Edet, P.O. Amadi, U.S. Okorie, G.J. Rampho, and H.Y. Abdullah, "Thermodynamic function for diatomic molecules with modified Kratzer plus screened Coulomb potential", *Indian Journal Physics*, **159**, 11 (2020),
- [5] E.P. Inyang, E.P. Inyang, I.O. Akpan, J.E. Ntibi, and E.S. William, "Masses and thermodynamic properties of a Quarkonium system", *Canadian Journal Physics*, **99**, 990 (2021), <https://doi.org/10.1139/cjp-2020-0578>
- [6] E.P. Inyang, E.S. William, E. Omugbe, E.P. Inyang, E.A. Ibanga, F. Ayedun, I.O. Akpan, and J.E. Ntibi, "Application of Eckart-Hellmann potential to study selected diatomic molecules using Nikiforov-Uvarov-Functional analysis method", *Revista Mexicana de Fisica*, **68**, 1 (2022), <https://doi.org/10.31349/RevMexFis.68.020401>
- [7] C.O. Edet, S. Mahmoud, E.P. Inyang, N. Ali, S.A. Aljumid, R. Endut, A.N. Ikot, and M. Asjad, "Non-Relativistic Treatment of the 2D Electron System Interacting via Varshni-Shukla Potential Using the Asymptotic Iteration Method", *Mathematics*, **10**, 2824 (2022), <https://doi.org/10.3390/math10152824>
- [8] M. Abu-Shady, and E.M. Khokha, "Heavy-Light mesons in the non-relativistic Quark model using Laplace Transformation method with the Generalized Cornell potential", *Advances in high energy Physics*, **12**, 345 (2018), <https://doi.org/10.1155/2018/7032041>
- [9] M. Abu-Shady, and A.N. Ikot, Analytic solution of multi-dimensional Schrödinger equation in hot and dense QCD media using the SUSYQM method, *The European Physical Journal Plus*, **134**, 7 (2019), <https://doi.org/10.1140/epjp/i2019-12685-y>
- [10] E.P. Inyang, E.S. William, and J.A. Obu, "Eigensolutions of the N-dimensional Schrödinger equation' interacting with Varshni-Hulthen potential model", *Revista Mexicana De Fisica*, **67**, 193 (2021), <https://doi.org/10.31349/RevMexFis.67.193>
- [11] C.O. Edet, P.O. Okoi, A.S. Yusuf, P.O. Ushie, and P.O. Amadi, "Bound state solutions of the generalized shifted Hulthen potential", *Indian Journal of physics*, **95**, 471 (2021), <https://doi.org/10.1007/s12648-019-01650-0>

- [12] I.O. Akpan, E.P. Inyang, E.P. Inyang, and E.S. William, "Approximate solutions of the Schrödinger equation with Hulthen-Hellmann Potentials for a Quarkonium system", *Revista Mexica De Fisica*, **67**, 482 (2021), <https://doi.org/10.31349/RevMexFis.67.482>
- [13] E.S. William, E.P. Inyang, and E.A. Thompson, Arbitrary l -solutions of the Schrödinger equation interacting with Hulthén-Hellmann potential model, *Revista Mexicana Fisica*, **66**, 730 (2020), <https://doi.org/10.31349/RevMexFis.66.730>
- [14] S.K. Nikiforov, and V.B. Uvarov, *Special functions of Mathematical Physics*, (Birkhauser, Basel, 1988)
- [15] E.P. Inyang, E.P. Inyang, J.E. Ntibi, E.E. Ibekwe, and E.S. William, "Approximate solutions of D-dimensional Klein-Gordon equation with Yukawa potential via Nikiforov-Uvarov method", *Indian Journal of Physics*, **7** (2021), <https://doi.org/10.1007/s12648-020-01933-x>
- [16] A.N. Ikot, U.S. Okorie, P.O. Amadi, C.O. Edet, G.J. Rampho, and R. Sever, "The Nikiforov-Uvarov – Functional Analysis (NUFA) Method: A new approach for solving exponential-Type potentials", *Few-Body System*, **62**, 9 (2021), <https://doi.org/10.1007/s00601-021-01593-5>
- [17] E.P. Inyang, P.C. Iwuji, J.E. Ntibi, E.S. William, and E.A. Ibanga, "Solutions of the Schrodinger equation with Hulthen –screened Kratzer potential: Application to diatomic molecules", *East Eur. J. Physics*, **1**, 12 (2022), <https://periodicals.karazin.ua/ejpp/article/view/18409/16804>
- [18] E.E. Ibekwe, U.S. Okorie, J.B. Emah, E.P. Inyang, and S.A. Ekong, "Mass spectrum of heavy quarkonium for screened Kratzer potential (SKP) using series expansion method", *European Physics Journal Plus*, **87**, 136 (2021), <https://doi.org/10.1140/epjp/s13360-021-01090-y>
- [19] E.M. Khokha, M. Abushady, and T.A. Abdel-Karim, "Quarkonium masses in the N-dimensional space using the Analytical Exact Iteration method", *International Journal of Theoretical and Applied Mathematics*, **2**, 86 (2016), <https://article.sciencepublishinggroup.com/pdf/10.11648.j.ijtam.20160202.19.pdf>
- [20] E. Omugbe, O.E. Osafire, I.B. Okon, E.S. Eyube, E.P. Inyang, U.S. Okorie, A. Jahanshir, and C.A. Onate, "Non-relativistic bound state solutions with α -deformed Kratzer-type potential using the super-symmetric WKB method: application to theoretic-information measures", *European Physical Journal D*, **76**, 72 (2022), <https://doi.org/10.1140/epjd/s10053-022-00395-6>
- [21] E. Omugbe, O.E. Osafire, E.P. Inyang, and A. Jahanshir, "Bound state solutions of the hyper-radial Klein-Gordon equation under the Deng-Fan potential by WKB and SWKB methods", *Physica Scripta*, **96**, 125408 (2021), <https://doi.org/10.1088/1402-4896/ac38d4>
- [22] E.P. Inyang, E.S. William, J.E. Ntibi, J.A. Obu, P.C. Iwuji, and E.P. Inyang, "Approximate solutions of the Schrodinger equation with Hulthen plus screened Kratzer potential using the Nikiforov-Uvarov-Functional analysis method: An Application to diatomic molecules", *Canadian Journal of Physics*, (2022), <https://doi.org/10.1139/cjcp-2022-0030>
- [23] P. Nwabuzor, C. Edet, A. Ndemikot, U. Okorie, M. Ramantswana, R. Horchani, A. Abdel-Aty, and G. Rampho, "Analyzing the effects of Topological defect (TD) on the Energy Spectra and Thermal Properties of LiH, TiC and I₂ Diatomic molecules", *Entropy*, **23**, 1060 (2021), <https://doi.org/10.3390/e23081060>
- [24] A.N. Ikot, W. Azogor, U.S. Okorie, F.E. Bazuaye, M.C. Onjeaj, C.A. Onate, and E.O. Chukwuocha, "Exact and Poisson Summation thermodynamic properties for diatomic molecules with shifted Tietz potential", *Indian Journal of Physics*, **93**, 1171 (2019), <https://doi.org/10.1007/s12648-019-01375-0>
- [25] E.P. Inyang, E.S. William, J.O. Obu, B.I. Ita, E.P. Inyang, and I.O. Akpan, "Energy spectra and expectation values of selected diatomic molecules through the solutions of Klein-Gordon equation with Eckart-Hellmann potential model", *Molecular Physics*, **119**, e1956615 (2021), <https://doi.org/10.1080/00268976.2021.1956615>
- [26] U.P. Obogo, O.E. Ubi, C.O. Edet, and A.N. Ikot, "Effect of the deformation parameter on the nonrelativistic energy spectra of the q-deformed Hulthen-quadratic exponential-type potential", *Ecletica Quimica Journal*, **46**, 73 (2021), <https://doi.org/10.26850/1678-4618eqj.v46.4.2021.p60-73>
- [27] C.O. Edet, and A.N. Ikot, "Superstatistics of Diatomic molecules with the shifted Deng-Fan potential model", *Biointerface Research in Applied Chemistry*, **12**, 4139 (2022), <https://doi.org/10.33263/BRIAC123.41264139>
- [28] J.Y. Liu, X-T. Hu, and C-S. Jia, "Molecular energies of the improved Rosen-Morse potential energy model", *Canadian Journal of Chemistry*, **95**, 40 (2014), <https://doi.org/10.1139/cjc-2013-0396>
- [29] C.A. Onate, and T.A. Akanbi, "Solutions of the Schrodinger equation with improved Rosen Morse potential for nitrogen molecule and sodium dimer", *Results in Physics*, **22**, 103961 (2021), <https://doi.org/10.1016/j.rinp.2021.103961>
- [30] C.A. Onate, T.A. Akanbi, and I.B. Okon, "Ro-vibrational energies of cesium dimer and lithium dimer with molecular attractive potential", *Scientific Reports*, **11**(1), 6198 (2021), <https://doi.org/10.1038/s41598-021-85761-x>
- [31] C.A. Onate, M.C. Onyeaju, E. Omugbe, I.B. Okon, and O.E. Osafire, "Bound state solutions and thermal properties of the modified Tietz-Hua potential", *Scientific Reports*, **11**, 2129 (2021), <https://doi.org/10.1038/s41598-021-81428-9>
- [32] A.N. Ikot, U.S. Okorie, R. Sever, and G.J. Rampho, "Eigensolution, expectation values and thermodynamic properties of the screened Kratzer potential", *European Physical Journal Plus*, **134**, 386 (2019), <https://doi.org/10.1140/epjp/i2019-12783-x>
- [33] A.N. Ikot, C.O. Edet, P.O. Amadi, U.S. Okorie, G.J. Rampho, and H.Y. Abdullah, "Thermodynamic properties of Aharanov-Bohm (AB) and magnetic fields with screened Kratzer potential", *European Physical Journal D*, **74**, 159 (2020), <https://doi.org/10.1140/epjd/e2020-10084-9>
- [34] A.N. Ikot, U.S. Okorie, A.T. Ngiangia, C.A. Onate, C.O. Edet, I.O. Akpan, and P.O. Amadi, "Bound state solutions of the Schrodinger equation with energy-dependent molecular Kratzer potential via asymptotic iteration method", *Ecletica Quimica Journal*, **45**, 65-77 (2020), <https://doi.org/10.26850/1678-4618eqj.v45.1.2020.p65-77>
- [35] C.O. Edet, A.N. Ikot, M.C. Onyeaju, U.S. Okorie, G.J. Rampho, M.L. Lekala, and S. Kaya, "Thermo-magnetic properties of the screened Kratzer potential with spatially varying mass under the influence of Aharanov-Bohm (AB) and position-dependent magnetic fields", *Physica E: Low-dimensional System and nanostructures*, **131**, 114710 (2021), <https://doi.org/10.1016/j.physe.2021.114710>
- [36] E.P. Inyang, E.P. Inyang, E.S. William, and E.E. Ibekwe, "Study on the applicability of Varshni potential to predict the mass-spectra of the Quark-Antiquark systems in a non-relativistic framework", *Jordan Journal of Physics*, **14**(4), 339-345 (2021), <https://doi.org/10.47011/14.4.8>
- [37] R.L. Greene, and C. Aldrich, "Variational wave functions for a screened Coulomb potential", *Physical Review A*, **14**, 2363 (1976), <https://doi.org/10.1103/PhysRevA.14.2363>

- [38] E.S. William, E.P. Inyang, I.O. Akpan, J.A. Obu, A.N. Nwachukwu, and E.P. Inyang, “Ro-vibrational energies and expectation values of selected diatomic molecules via Varshni plus modified Kratzer potential model”, Indian Journal of Physics, (2022) <https://doi.org/10.1007/s12648-022-02308-0>
- [39] O. Ebomwonyi, C.A. Onate, M.C. Onyeaju, and A.N. Ikot, “Any l -states solutions of the Schrodinger equation interacting with Hellmann-generalized Morse potential model”, Karbala International Journal Modern Science, **3**, 59 (2017), <https://doi.org/10.1016/j.kijoms.2017.03.001>
- [40] E.P. Inyang, P.C. Iwuji, J.E. Ntibi, E. Omugbe, E.A. Ibanga, and E.S. William “Quark-antiquark study with inversely quadratic Yukawa potential using Nikiforov-Uvarov-Functional analysis method”, East Eur. J. Phys. **2**, 43-51 (2022), <https://periodicals.karazin.ua/eejp/article/view/18535/16839>
- [41] R.R. Reddy, Y.N. Ahammed, B.S. Devi, P.A. Azeem, K.R. Gopal, and T.V.R. Rao, “Potential energy curves, dissociation energies and Franck Condon factors for NI and ScI molecules”, Journal of Quantum Spectroscopy and Radiation Transfer, **74**, 125 (2002), [https://doi.org/10.1016/S0022-4073\(01\)00184-4](https://doi.org/10.1016/S0022-4073(01)00184-4)

ДОСЛІДЖЕННЯ ЕЛЕКТРОННИХ СТАНІВ МОЛЕКУЛ NI ТА ScI З ЕКРАНОВАНИМ ПОТЕНЦІАЛОМ КРАТЦЕРА

Етідо П. Ін'янг^а, Ефйонг О. Обісунг^б

^аФізичний факультет, Національний відкритий університет Нігерії, Джабі, Абуджа, Нігерія

^бФізичний факультет, Калабарський університет, Калабар, Нігерія

У цьому дослідженні за допомогою відомого методу Нікіфорова-Уварова аналітично розв'язується рівняння Шредінгера з екранованою потенціальною моделлю Кратцера. Отримано енергетичний спектр і нормовану хвильову функцію з наближенням Гріна-Олдріча для відцентрового члена. Енергетичний спектр використовується для генерації власних значень для $X^3\Sigma^-$ стану NI та $X^1\Sigma^+$ стану молекул ScI відповідно. Розрахункові результати добре узгоджуються з експериментальними даними. Це дослідження знайшло застосування в хімії, промисловості, молекулярній фізиці та дослідженнях магнітокалоричного ефекту для кількох молекул. Наші результати також демонструють, що схема апроксимації добре підходить для цього потенціалу.

Ключові слова: рівняння Шредінгера; метод Нікіфорова-Уварова; екранований потенціал Кратцера; молекули

ENTANGLED COHERENT STATES IN TELEPORTATION[†]

Shivani A. Kumar*, Shefali Kanwar, Pramila Shukla

Amity Institute of Applied Sciences, Amity University, Noida, India

*Corresponding Author: shivani_v11@rediffmail.com

Received June 7, 2022; revised June 13, 2022; accepted June 22, 2022

In the present paper, we will review the methods to produce superposition of entangled coherent state using polarizing beam splitter and Kerr non linearity. These coherent states have many attractive features and can be used in various schemes. Entanglement, refers to the superposition of a multiparticle system and explains a new type of correlations between any two subsystems of the quantum system, which is not existing in the classical physics. The present paper deals with the use of these states in quantum teleportation, entanglement diversion and entanglement swapping schemes. Entanglement diversion and entanglement-swapping refers to a scheme which may entangle those particles which had never interacted before. In the swapping scheme, two pairs of entangled state are taken. One particle from each pair is subjected to a Bell-state-measurement. This would result in projection of the other two outgoing particles in an entangled pair. Quantum Teleportation of two mode and three modes states is also studied with perfect fidelity. Minimum assured fidelity which is defined as the minimum of the fidelity for any unknown quantum information of the states is also discussed. It is also shown how the success rate of teleportation of a superposition of odd and even coherent states can be increased from 50% to almost 100%. The scheme suggested by van Enk and Hirota was modified by Prakash, Chandra, Prakash and Shivani in 2007. We find that an almost teleportation, diversion and swapping is possible by simply separating vacuum state from the even state. The present paper also deals with study of effect of decoherence and noise on these states and the effect of noise on fidelity and minimum assured fidelity. It is also discussed that these schemes can also be applied to the process of entanglement diversion and entanglement swapping.

Keywords: Entanglement, teleportation, fidelity, coherent state

PACS: 03.67. Hk, 03.65. Ud, 03.67. Lx

INTRODUCTION

The most important feature of the quantum optics is the study of the effects of the interaction between atoms and laser fields, and most of the issues with a specific set of quantum states for the description of the area, as well as the atoms [1,2]. They are referred to as coherent-states, and it can be used in the problem of the sub-areas of interaction. These states are commonly referred to as the Glauber states [3-5], and in honor of that, the American scientist who is, for the first time, we realized that in their good use for the description of optical phenomena. These proposals are currently being intensively studied and applied to the quantum-optical problems. The explicit form of states in question is,

$$|\alpha\rangle = \sum_{n=0}^{\infty} e^{-\frac{1}{2}|\alpha|^2} \frac{\alpha^n}{\sqrt{n!}} |n\rangle \quad (1)$$

where the Fock-states $|n\rangle$ is eigen-state of the number operator $N = a^\dagger a$, i.e., $N|n\rangle = n|n\rangle$ and $\alpha = \alpha_r + i\alpha_i$ is complex number.

Sudarshan [7] and Glauber also provided a diagonal representation independently for the density operator of the radiation in point of coherent-states. Coherent-state is a pure state and also it is not a non-diagonal state. Superposition which includes the superposition of any two or more than two coherent-states are non-classical. Numerous possibilities for generation of the non-classical-state of the electromagnetic field has also been presented [8, 9].

However, whenever we are considering the class of the states including the superposition of any two coherent-states of an equal amplitude and are separated by phase of 180° , i.e. states takes the form

$$|\psi\rangle = \frac{1}{\sqrt{N_z}} \left[|\beta\rangle \pm e^{i\theta} |-\beta\rangle \right] \quad (2)$$

Here, the normalization constant N_z is given as,

$$N_z = 2 + 2e^{-2|\beta|^2} \cos\theta, \quad (3)$$

For large $|\beta|$, states $|\beta\rangle$ and $|-\beta\rangle$ are very much macroscopically distinguishable. The and superposition state of the form in equation (2) is termed as the Schrodinger's-cat-states [10]. One of very initial treatments for producing this superposition of the states were given by scientists Yurke & Stoler who demonstrated generation of a coherent-superposition of the state of the form

[†] Cite as: S.A. Kumar, S. Kanwar, and P. Shukla, East Eur. J. Phys. 3, 39 (2022), <https://doi.org/10.26565/2312-4334-2022-3-05>

© S.A. Kumar, S. Kanwar, P. Shukla, 2022

$$|\psi\rangle = \frac{1}{\sqrt{2}} \left[|\alpha\rangle + e^{i\pi/2} |-\alpha\rangle \right], \tag{4}$$

using a Kerr nonlinearity.

Tara et al. [11] showed generation of Schrodinger-macroscopic-quantum superposed states in an optical Kerr non-linear medium. The authors also presented a scheme for generation of superposed squeezed-coherent-states. In 1996, C.C. Gerry presented a scheme to generate Schrodinger-cat-states as well as the entangled-coherent-states by dispersive interaction inside a trapped ion. The author demonstrated that the entangled-coherent-states may be produced which are a general form of Schrodinger-cat-state giving some very strong correlations between different output modes.

In 1999, a famous researcher Gerry [12,13] presented a scheme to produce Schrodinger-cat-states. Recently, Kim & Paternostro [12] also presented a method to generate superposed coherent-states with the help of small Kerr-non linearity effect and single photon or even two entangled-twin-photons. However, both of the above-mentioned authors in the references [11] and [12,13] had used cross Kerr nonlinearity whose evolution operator is shown as $\hat{U}_{CK} = \exp(-i\chi \hat{n}_a \hat{n}_b)$. This may affect the phase of the system which depends on the photon-numbers of the output two modes a & b. Here, \hat{n}_b is termed as photon-number operator for the output mode b. If the mode a is in the coherent-state of its amplitude α & the mode b is in the single photon state, then using the action of the cross Kerr-nonlinearity,

$$\hat{U}_{CK} |\alpha\rangle_a |n\rangle_b = |\alpha e^{in_b \chi t}\rangle_a |n\rangle_b, \tag{5}$$

here, the Fock state $|n\rangle_b$ remains unaffected with interaction. However, the coherent state $|\alpha\rangle_a$ takes a phase shift which is directly proportional to the photon-number n_b in the state $|n\rangle_b$.

Recently Hari Prakash and coauthors [14,15] presented a method for generating a general superposition of the coherent-states $|\alpha\rangle$ and $|-\alpha\rangle$ taking the action of Kerr effect into account. Their method involved two beams in coherent-states, a single photon-beam and some linear optical devices such as polarization beam-splitter & mirrors. The authors showed that, if a single photon beam is obtained in the output mode in a desired polarization state which is defined by the angles θ & ϕ , then this results in a definite superposed coherent-states $|\alpha\rangle$ and $|-\alpha\rangle$. If any photon is obtained in any orthogonal state of polarization, this results in a superposition which is different from desired one.

These macroscopic superposition of coherent-states have been shown to possess various important non-classical properties. For example, a Schrodinger cat state of the form

$$|\psi\rangle = c_1 |\alpha e^{i\theta}\rangle + c_2 |\alpha e^{-i\theta}\rangle \tag{6}$$

is known to lead a squeezed state, normal 2nd order squeezing, higher-order squeezing & sub-poissonian statistics and other non-classical properties of the field.

Entanglement

Entanglement, is a simple name given for the superposition of a multiparticle system. It is one of a most important aspects of quantum mechanics. It explains a new type of correlations between any two subsystem of the quantum system, which is not existing in the classical physics. This word is the translation of a German word "Verschränktheit". It is first noted by Schrödinger in his paper. Both the words have notation of the word "contortedness", which demonstrates the efforts of understanding such correlations in classical terms. However, from this point of view of the Quantum Theory, such correlations very straightforward.

An entangled, composite quantum system is divided into separate sub-systems, which are closely related to each other, even if they're far away from each other and do not interact with each other. If a measurement is carried out in one of the sub-systems, it has an effect on the results of the measurements carried out in the other sub-system. This feature is in a contradiction with local realism, i.e., the statement that the quantum states of spatially-separated, non-interacting particles are independent of each other. This phenomenon has been discussed by Einstein-Podolsky-Rosen (EPR) in 1935, in their initial paper. Their paper was the attempt to explain that quantum mechanics is an incomplete mechanics. EPR explained as the starting point premises of "reality" and a "no-action-at-a-distance". It is many times termed as locality. In their paper, "local realism" is explained as a dual premise, in which both the realism as well as the locality is assumed. In this reply Schrodinger introduced the concept of entangled quantum states, pointing to entanglement as a signature of states not compatible with classic notions, such as local realism. Schrodinger's reply is best known for his discussion of paradox of macroscopically-entangled state, a "cat" in a quantum superposition of "alive" or "dead" states.

COMPUTATIONAL DETAILS

In the present paper, we have studied various aspects of entanglement such as teleportation, entanglement diversion and entanglement swapping. The success of teleportation is measured by calculating fidelity. This paper focusses on fidelity also.

Quantum Teleportation

Another important application of quantum entanglement, in correlation with quantum information processing, is termed as “**quantum teleportation**”. In teleportation, an unknown quantum state is being transferred from one location to another, which are widely separated. Quantum teleportation involves transferring complete information of one quantum state from one location to another location with aid of long-range E-P-R correlations in an entangled-state. This state is shared between the two parties which are known as the sender and the receiver. At first, the sender makes some measurements with the information states and her/his shared part of the entangled state. In this process, the information state disappears at the sender’s end and instantaneously appears at the receiver’s end. This is obtained when the receiver makes some unitary transformation which depends on some result of the sender’s measurement which is received through some classical channel. The process of teleportation somewhat resembles with the teleportation which had read in the science fiction (Shaktimaan) where one person or an object disappears at the sender’s place while an exact replica of the same person reappears at some other place. However, this replica is not generated instantaneously and that for making replica a classical information is required.

Suppose transfer of an unknown qubit of some quantum information is required from one party, whom we call as **Alex**, to another party called as **Bobby**. Alex and Bobby do not directly exchange any quantum system by any means carrying any information. This means that they do not share any quantum channel which is common for both the parties. Alex can try to find some qubit so as to obtain the classical information, which she will convey to Bobby via some classical channel. Based on the information received from Alex, Bobby will then try to reconstruct the original state again. Bennett and coauthors [16] proposed **teleportation** which allows Alex and Bobby to transfer a quantum state perfectly from one point to another provided that both the parties share one-half part of an entangled pair of particles. Now Alex would find the unknown qubit of her part of the entangled pair in a particular basis. She then conveys the outcome of her measurement results to Bobby. After that, Bobby collects necessary information to again reconstruct the original state from his share of the entangled pair.

Fidelity

The efficiency of teleportation is determined by measuring **fidelity**. The fidelity of the teleportation is defined by overlap of the input information state with the (normalized) output teleported state. It also gives a measure of the quality of the teleported state. By determining the overlap between the input information state $|\psi\rangle$ and the teleported output state, ρ , i.e.

$$F = \langle \psi | \rho | \psi \rangle \quad (7)$$

If the output state is exactly same as the input information state, then the fidelity of the teleportation is equal to unity.

Fidelity is state dependent, i.e., the fidelity of the reconstructed state depends both on the quality of the teleporter and on the class of input states from which the unknown state is picked. However, some authors have defined the fidelity as

$$F = \text{Tr} \left[\rho_{out} | \varphi \rangle \langle \varphi | \right] \quad (8)$$

When ρ_{out} is an exact replica of $|\varphi\rangle$, then $F = 1$, and when ρ_{out} is an imprecise copy of $|\varphi\rangle$, then $F < 1$. Finally when ρ_{out} is completely orthogonal to the state $|\varphi\rangle$, the fidelity is zero and the teleportation is not possible. If $|I\rangle$ represents the information state, to be teleported, and $|T\rangle$ represents the teleported copy of the initial information state that Bobby has in his hand after application of the unitary transformation, then fidelity of the teleported state is calculated by using, $\rho_{out} = |T\rangle\langle T|$ which gives,

$$F = \langle T | I \rangle \langle I | T \rangle. \quad (9)$$

In a paper van Enk and Hirota [17] gave a scheme to teleport one bit of quantum information contained in a superposition of even and odd coherent-states. They used entangled-coherent-states, a beam splitter and two-phase shifters. X. Wang [18,19] also presented a scheme of teleportation of 1 bit of information contained in bipartite superposed entangled coherent state using a tripartite entangled coherent state, similar to the scheme of van Enk and Hirota. N. Ba An [20] presented a scheme to teleport a single particle state using a four-partite state, a beam-splitter and two phase-shifters.

Recently quantum teleportation has been demonstrated experimentally using parametric down conversion in interferometric Bell state analyzers. Quantum teleportation of states with continuous degree of freedom has been demonstrated both experimentally and theoretically. Teleportation of continuous variables can be described in two different ways, one in terms of Wigner functions, the other in terms of discrete basis states. Also, the efficiency of teleportation of discrete and continuous observable was tested directly with the help of Mach Zehnder interferometer. These entangled-coherent-states play a very important role in teleportation. However, Fan and Lu An. [21-23] have used the terminology “coherent entangled states” which is completely different from “entangled coherent state”.

Entanglement Diversion

Another field in which entanglement plays a very important role is *entanglement diversion* which was originally presented by C. Xin-Hua and coauthors [24]. He involved three remote parties, Alex, Bobby and Charlie. Out of these three parties, Alex is connected to Bobby and Charlie both by sharing an entangled state involving two modes. Here, the diversion scheme connects Bobby and Charlie which were not connected by sharing any entangled two mode state.

In recent years, however, entanglement has aroused much interest in the quantum information processing such as quantum computation, quantum dense coding and quantum cryptography quantum-telecloning, entanglement-purification and quantum-error-corrections.

Entanglement Swapping

A similar concept is *entanglement-swapping*. This is a scheme which may entangle those particles which had never interacted before. In the swapping scheme, two pairs of entangled state are taken. One particle from each pair is subjected to a Bell-state-measurement. This would result in projection of the other two outgoing particles in an entangled pair. This scheme was first demonstrated by Zukowski and his coauthors [25]. In their scheme, the authors used two parametric-down-converters, each of which emitted a photon pair. This resulted in entangling the other two initially independent photons by coincident registration of idlers. the first experimental realization of entanglement swapping was reported by Pan et al. [26, 27] and others.. The scheme was generalized to multiparticle system by Zeilinger et al. [28,29] and some other authors, and Bose et al. [30]. Entanglement swapping scheme for multi-qudit system was first given by Bose and his coauthors, and for continuous variables, it has been shown experimentally. It has also been demonstrated that in any two partially entangled states, entanglement swapping yields the weaker entanglement of the two.

A scheme of teleporting a superposed coherent-states $|\alpha\rangle$ and $|\alpha\rangle$ with the help of beam-splitter and two phase-shifters was done. The authors obtained an near perfect teleportation for an appreciable mean photon-numbers. They also calculated the minimum of the average fidelity and showed that for $|\alpha|^2 = 5$, the minimum of the average fidelity is 0.9999. At the end they conclude that, the scheme leads to a near perfect successful teleportation for some appreciable photons. The authors wrote coherent state $|\alpha\rangle$ in terms of the even and the odd coherent state [31-39],

$$|_{EVEN / ODD, \alpha}\rangle = \frac{|\alpha\rangle \pm |-\alpha\rangle}{\sqrt{2(1 \pm x^2)}}, \quad x \equiv e^{-|\alpha|^2} \tag{10}$$

The authors separated $|_{EVEN, \alpha}\rangle$ as the superposition of vacuum state $|0\rangle$ and the non-zero -even photon state $|_{NZE, \alpha}\rangle$ [75-84] and wrote

$$|\pm\alpha\rangle = \sqrt{x} |0\rangle + 2^{-1/2} (1-x) |_{NZE, \alpha}\rangle \pm [(1/2)(1-x^2)]^{1/2} |_{ODD, \alpha}\rangle, \tag{11}$$

where

$$|_{NZE, \alpha}\rangle = (|\alpha\rangle + |-\alpha\rangle - 2\sqrt{x}|0\rangle) / \sqrt{2(1-x)}. \tag{12}$$

A scheme of teleporting bipartite entangled-coherent-states including tripartite entangled-coherent-states, beam-splitters and phase-shifters was also presented. We concluded that a near-to-perfect teleportation may be obtained when an appreciable mean-number of photons were present in the output. Here also we find the minimum of the average fidelity and showed that it is 0.9999 even if $|\alpha|^2 = 5$. Thus, an almost perfect teleportation can be achieved even if mean number of photons is quite low. We again discuss the impact of the noise (decoherence) on the fidelity in the scheme of the teleportation in this context.

Another scheme of teleporting a superposition of the even and the odd coherent-states involving a 4-partite entangled-coherent-states, and linear devices such as beam- splitters and phase-shifters. This scheme, was dealt with a system comprising four partners: Alex, Bobby, Charlie and David. We calculated a near-to- perfect teleportation if an appreciable mean-number of photons were found. Here also we calculated the minimum of the average-fidelity (MAF) and find that it is 0.9999 for $|\alpha|^2 = 5$.

Entanglement-diversion is discussed between two entangled-coherent-states. This is a scheme in which the entanglement of entangled-coherent-states is diverted. In this diversion scheme, there are any three distant partners named as: Alex, Bobby and Charlie. Alex and Bobby are connected with each other by sharing a quantum channel $|\Phi\rangle_{13}$ of the state in mode 1 which is with Alex and the state in mode 3 which is with Bobby. Alex and Charlie are also connected with each other by sharing another quantum channel $|\Phi\rangle_{24}$ of the state in the mode 2 which is with Alex and the state in the mode 4 which is with Charlie. These connected partners may take the help of entangled-states of the shared quantum channel. It may be used to teleport the quantum channel between them. Through entanglement-diversion-scheme, Bobby

and Charlie will also develop a very direct connection between them. The authors, find that a near-to-perfect diversion may be achieved if an appreciable mean-number of photons are present.

Entanglement-swapping between two imperfectly entangled-coherent-states. Our proposal involves a beam-splitter and optical instruments like two-phase-shifters. A near-to-perfect swapping may be possible for an appreciable mean number of photons.

RESULT AND DISCUSSION

Superposition of an entangled-coherent-states can be produced using the process of Kerr-nonlinearity. These coherent-states play a very vital role in the quantum teleportation of entangled coherent state, whether it is single particle system or a multiparticle system. They also can be used to produce the scheme of entanglement diversion and entanglement-swapping schemes. By separating non zero even state from vacuum state, an almost perfect teleportation, diversion or swapping can be achieved which can be verified by calculating the fidelity of the final achieved state.

Acknowledgement

The authors are extremely grateful to Amity University, Noida.

ORCID IDs

Shivani A. Kumar, <https://orcid.org/0000-0003-0200-9570>; Shefali Kanwar, <https://orcid.org/0000-0002-8869-2165>
Pramila Shukla, <https://orcid.org/0000-0002-7786-6510>

REFERENCES

- [1] P. Shukla, S.A. Kumar, and S. Kanwar, "Interaction of Light with matter: nonclassical phenomenon", *Physics and Chemistry of Solid State*, **23**(1), 5-15, 2022, <https://doi.org/10.15330/pcss.23.1.5-15>
- [2] E. Schrodinger, "An undulatory theory of the mechanics of atoms and molecules", *Phys. Rev.* **28**, 1049-1054 (1926), <https://doi.org/10.1103/PhysRev.28.1049>
- [3] R.J. Glauber, "The Quantum Theory of Optical Coherence", *Phys. Rev.* **130**, 2529-2536 (1963), <https://doi.org/10.1103/PhysRev.130.2529>
- [4] R.J. Glauber, "Coherent and Incoherent States of the Radiation Field", *Phys. Rev.* **131**, 2766-2772 (1963), <https://doi.org/10.1103/PhysRev.131.2766>
- [5] R.J. Glauber, *In Quantum Optics and Electronics*, edited by C. De Witt, A. Blandin and C. Cohen-Tanaudiji, (Gordon and Breach, New York, 1965)
- [6] V. Fock, „Verallgemeinerung und Lösung der Diracschen statistischen Gleichung“, *Z. Phys.* **49**, 339-351 (1928), <https://doi.org/10.1007/BF01337923>
- [7] E.C.G. Sudarshan, "Equivalence of Semiclassical and Quantum Mechanical Descriptions of Statistical Light Beams", *Phys. Rev. Lett.* **10**, 277-286 (1963), <https://doi.org/10.1103/PhysRevLett.10.277>
- [8] D. Stoler, B.E.A. Saleh, and M.C. Teich, "Binomial States of the Quantized Radiation Field", *Opt. Acta*, **32**, 345 (1985), <https://doi.org/10.1364/JOSAB.4.000185>;
- [9] B. Yurke, and D. Stoler, "Generating Quantum Mechanical Superpositions of Macroscopically Distinguishable States via Amplitude Dispersion", *Phys. Rev. Lett.* **57**, 13-18 (1986), <https://doi.org/10.1103/PhysRevLett.57.13>
- [10] C.C. Gerry, "Generation of Schrodinger cats and entangled-coherent-states in the motion of a trapped ion by a dispersive interaction", *Phys. Rev. A*, **55**, 2479-2487 (1996), <https://doi.org/10.1103/PhysRevA.55.2478>
- [11] K. Tara, G.S. Agarwal, and S. Chaturvedi, "Production of Schrodinger macroscopic quantum superposition states in a Kerr medium", *Phys. Rev. A*, **47**, 5024-5031 (1993), <https://doi.org/10.1103/PhysRevA.47.5024>
- [12] C.C. Gerry, "Generation of optical macroscopic quantum superposition states via state reduction with a Mach-Zehnder interferometer containing a Kerr medium", *Phys. Rev. A*, **59**, 4095-4103 (1999), <https://doi.org/10.1103/PhysRevA.59.4095>
- [13] M.S. Kim, and M. Paternostro, "Generation of a coherent superposition state on demand", <https://arxiv.org/abs/quant-ph/0510057>
- [14] S.A. Kumar, H. Prakash, N. Chandra, and R. Prakash, "Production of Superposition of Coherent-states Using Kerr Non-Linearity", *Springer Proceedings in Physics*, **256**, 117-126, (2020), https://doi.org/10.1007/978-981-15-8625-5_13
- [15] Shivani. A. Kumar, "Quantum teleportation of a tripartite entangled coherent state", *Modern Physics Letters A*, **36** (31), 2150217-2150227, 2021, <https://doi.org/10.1142/S0217732321502175>
- [16] C.H. Bennett, G. Brassard, C. Crepeau, R. Jozsa, A. Peres, and W.K. Wootters, "Teleporting an Unknown Quantum State via Dual Classical and Einstein-Podolsky-Rosen Channels", *Phys. Rev. Lett.* **70**, 1895 (1993), <https://doi.org/10.1103/PhysRevLett.70.1895>
- [17] S.J. van Enk, and O. Hirota, "Entangled-coherent-states: Teleportation and decoherence", *Phys. Rev. A*, **64**, 022313 (2001), <https://doi.org/10.1103/PhysRevA.64.022313>
- [18] X. Wang, "Quantum teleportation of entangled-coherent-states, *Phys. Rev. A*", **64**, 022302 (2001), <https://doi.org/10.1103/PhysRevA.64.022302>
- [19] Parakh, A. "Quantum teleportation with one classical bit", *Scientific Reports*, **12**(1) 3392, (2022), <https://doi.org/10.1038/s41598-022-06853-w>
- [20] N.B. An, "Teleportation of coherent-state superpositions within a network", *Phys. Rev. A*, **68**, 022321-022329 (2003), <https://doi.org/10.1103/PhysRevA.68.022321>
- [21] H.Y. Fan, and H.L. An, "New two-mode coherent-entangled state and its application", *J. Phys. A*, **37**, 10993-10997 (2004), <https://doi.org/10.1088/0305-4470/37/45/017>
- [22] M. Swathi, and B. Rudra, "An efficient approach for quantum entanglement purification", *International Journal of Quantum Information*, **20**(4), 225004, (2022), <https://doi.org/doi:10.1142/S0219749922500046>

- [23] S. Banerjee, A. Patel, and P. Panigrahi, "Minimum distance of the boundary of the set of PPT states from the maximally mixed state using the geometry of the positive semidefinite cone", *Quantum Inf. Process* **18**, 296 (2019). <https://doi.org/10.1007/s11128-019-2411-6>
- [24] C.X. Hua, G.J. Rong, N.J. Jun, and J.J. Ping, "Entanglement diversion and quantum teleportation of entangled-coherent-states", *Chinese Physics*, **15**, 488 (2006), <https://doi.org/10.1088/1009-1963/15/3/006>
- [25] M. Zukowski, A. Zeilinger, M.A. Horne, and A.K. Ekert, "Event-Ready-Detectors" Bell Experiment via Entanglement swapping *Phys. Rev. Lett.* **71**, 4287-4295 (1993), <https://doi.org/10.1103/PhysRevLett.71.4287>
- [26] J.W. Pan, D. Bouwmeester, H. Weinfurter, and A. Zeilinger, "Experimental Entanglement Swapping: Entangling Photons That Never Interacted", *Phys. Rev. Lett.* **80**, 3891-3899 (1998), <https://journals.aps.org/prl/abstract/10.1103/PhysRevLett.80.3891>
- [27] K.G. Paulson, and P.K. Panigrahi, "Tripartite non-maximally-entangled mixed states as a resource for optimally controlled quantum teleportation fidelity", *Physical Review A*, **100**(5), 052325 (2019), <https://doi.org/10.1103/PhysRevA.100.052325>
- [28] A. Zeilinger, M.A. Horne, H. Weinfurter, and M. Zukowski, "Three-Particle Entanglement from Two Entangled Pairs", *Phys. Rev. Lett.* **78**, 3031-3038 (1997), <https://doi.org/10.1103/PhysRevLett.78.3031>
- [29] J. I. de Vicente, C. Spee, D. Sauerwein, and B. Kraus, "Entanglement manipulation of multipartite pure states with finite rounds of classical communication", *Phys. Rev. A* **95**, 012323 (2017), <https://doi.org/10.1103/PhysRevA.95.012323>
- [30] S. Bose, V. Vedral, and P.L. Knight, "Multiparticle generalization of entanglement swapping", *Phys. Rev. A*, **57**, 822-831 (1998), <https://doi.org/10.1103/PhysRevA.57.822>
- [31] S. Bose, V. Vedral, and P.L. Knight, "Purification via entanglement swapping and conserved entanglement", *Phys. Rev. A*, **60**, 194-201 (1999), <https://doi.org/10.1103/PhysRevA.60.194>
- [32] H. Prakash, N. Chandra, R. Prakash, and Shivani, "Improving the teleportation of entangled-coherent-states", *Phys. Rev. A*, **75**, 044305-044315 (2007), <https://doi.org/10.1103/PhysRevA.75.044305>
- [33] H. Prakash, N. Chandra, R. Prakash, and Shivani, "Effect of decoherence on fidelity in teleportation using entangled-coherent-states", *Journal of Physics B: Atomic, Molecular and Optical Physics*, **40**(8), 1613-1626 (2007), <https://doi.org/10.1088/0953-4075/40/8/012>
- [34] H. Prakash, N. Chandra, R. Prakash, and Shivani, "Effect of decoherence on fidelity in teleportation of entangled-coherent-states", *International Journal of Quantum Information*, **6**(5), 1077-1092 (2008), <https://doi.org/10.1142/S0219749908004213>
- [35] H. Prakash, N. Chandra, R. Prakash, and S.A. Kumar, "Entanglement diversion between two pairs of entangled-coherent-states", *International Journal of Modern Physics B*, **23**(4), 585-595 (2009), <https://doi.org/10.1142/S0217979209049930>
- [36] H. Prakash, N. Chandra, R. Prakash, and Shivani, "Swapping between two pairs of nonorthogonal entangled-coherent-states", *International Journal of Modern Physics B*, **23**(8), 2083-2092 (2009), <https://doi.org/10.1142/S0217979209052042>
- [37] H. Prakash, N. Chandra, R. Prakash, and Shivani, "Almost perfect teleportation using 4-partite entangled states", *International Journal of Modern Physics B*, **24**(17), 3383-3394 (2010), <https://doi.org/10.1142/S0217979210053367>
- [38] H. Prakash, N. Chandra, R. Prakash, and S.A. Kumar, "Improving the entanglement diversion between two pairs of entangled-coherent-states", *International Journal of Modern Physics B*, **24**(17), 3331-3339 (2010), <https://doi.org/10.1142/S0217979210053331>
- [39] S.A. Kumar, in: *International Conference on Fibre Optics and Photonics*, OSA Technical Digest (online) (Optica Publishing Group, 2012), paper WPo.8, <https://opg.optica.org/abstract.cfm?URI=Photonics-2012-WPo.8>
- [40] S.A. Kumar, H. Prakash, N. Chandra, R. Prakash, "Noise in swapping between two pairs of non-orthogonal entangled-coherent-states", *Modern Physics Letters B*, **27**(3), 1350017 (2013), <https://doi.org/10.1142/S0217984913500176>

ЗПЛУТАНІ КОГЕРЕНТНІ СТАНИ В ТЕЛЕПОРТАЦІЇ

Шивані А. Кумар, Шефалі Канвар, Праміла Шукла

Інститут прикладних наук Аміті, Університет Аміті, Нойда, Індія

У цій роботі ми розглянемо методи створення суперпозиції зплутаного когерентного стану з використанням поляризаційного розділювача пучка та нелінійності Керра. Ці когерентні стани мають багато привабливих рис і можуть бути використані в різних схемах. Зплутаність відноситься до суперпозиції багаточасткової системи і пояснює новий тип кореляцій між будь-якими двома підсистемами квантової системи, який не існує в класичній фізиці. У цій роботі йдеться про використання цих станів у квантовій телепортації, схемах відхилення зплутаності та заміна заплутування. Відхилення зплутаності та заміна заплутування відносяться до схеми, яка може зплутати ті частки, які ніколи раніше не взаємодіяли. У схемі зплутаності йдеться про дві пари зплутаного стану. Одна частка з кожної пари піддається виміру стану Белла. Це може призвести до відбиття у зплутаній парі двох інших часток, які виходять, Квантова телепортація дво-режимних і трьох-режимних станів також вивчається з ідеальною точністю. Також обговорюється мінімальна гарантована точність, яка визначається як мінімум точності для будь-якої невідомої квантової інформації про стани. Також показано, як рівень швидкості телепортації суперпозиції парних і непарних когерентних станів може бути збільшена з 50% до майже 100%. Схема, запропонована ван Енком і Хіртою, була модифікована Пракашем, Чандрою, Пракашем і Шивані у 2007 році. Ми виявили, що майже повна телепортація, відхилення та заміна можуть бути здійснені шляхом простого відокремлення стану вакууму від парного стану. У цій роботі також йдеться про вплив декогерентності та шуму на ці стани, а також про вплив шуму на точність та мінімальну гарантовану точність. Також обговорюється, що ці схеми також можуть бути застосовані до процесу відхилення зплутаності та заміни заплутування.

Ключові слова: зплутаність, телепортація, точність, когерентний стан

PRESSURE OF ELECTROMAGNETIC RADIATION ON A THIN LINEAR VIBRATOR IN A WAVEGUIDE[†]

Mykola G. Kokodii*, Victor O. Katrich, Sergey L. Berdnik, Mykhail V. Nesterenko,
Vyacheslav O. Maslov, Ivan O. Priz

V.N. Karazin Kharkiv National University, 4, Svobody Sq., 61022, Kharkiv, Ukraine

**Corresponding Author: kokodiyng@gmail.com*

Received June 22, 2022; revised June 30, 2022; accepted July 10, 2022

The problem of electromagnetic wave pressure on a thin conductive vibrator located in a rectangular waveguide is solved. Wave H_{10} falls on the vibrator. The vibrator is located perpendicular to the wide wall of the waveguide. The current in the vibrator arising under the action of the electric field of the wave is calculated. The current distribution along the vibrator is almost uniform. The current in the microwave range depends little on the vibrator conductivity. Two components of the magnetic field - longitudinal and transverse exist in the H_{10} wave. When these components interact with the current in the vibrator, forces arise, acting on the vibrator across the waveguide and along it. The magnitude of the longitudinal force is greatest when the vibrator is located in the middle of a wide wall. It is almost 2 times greater than the force acting on the vibrator in free space at the same average radiation intensity. When the vibrator length is close to half the radiation wavelength, the force is maximum. The transverse force is determined by the interaction of the current in the vibrator with the longitudinal component of the magnetic field in the waveguide. It is maximum when the vibrator is located at the distance of $\frac{1}{4}$ of the length of the wide wall from its middle. If the length of the vibrator is less than half the wavelength of the radiation, the force is directed towards the axis of the waveguide, otherwise - in the opposite direction. The possibility of using microwave radiation pressure to create micromachines and to control the position of the vibrator in space has been evaluated. This requires a radiation power of several watts.

Keywords: electromagnetic wave, conducting vibrator, radiation pressure, waveguide, longitudinal force, transverse force.

PACS: 78.70.Gq; 84.40.-x; 84.90.+a

The pressure of electromagnetic radiation is one of the fundamental physical phenomena. Its use is an actual direction of modern optics, laser physics and electrodynamics.

The ability to control the movement of bodies using the pressure of light or other electromagnetic radiation was recognized as possible after the experiments of P.N. Lebedev, in which he measured the pressure of light on solids and gases. For a long time, it seemed that the smallness of the light pressure, in the words of J. Poynting "...excludes it from consideration in earthly affairs". The situation has changed with the appearance of lasers. This is due to the possibility of sharp focusing of the laser beam, when the diameter of the focal spot is comparable with the dimensions of the light wavelength.

A. Ashkin, 2018 Nobel Prize winner, proved that the light pressure produced by a laser beam is sufficient to capture, hold in a given place, levitate and move micron-sized particles [1]. The existence of a transverse force was also proved, which pulls the particle into the center of the beam. Based on these works, devices were subsequently developed to control the position and movement of microparticles – "laser tweezers" [2-4]. Technical applications of the ponderomotive action of microwave and optical radiation in metrology and the design of ponderomotive microwave power meters are described in the monograph [5].

Currently applied not only the pressure of the wave on the object, but also the occurrence of a torque in the case of waves polarized in a circle. It was shown in [6] that the laser beam can rotate the microparticles.

In the microwave range, the operation of objects with the help of radiation pressure meets with great difficulties. This is due to the fact that the diameter of the focal spot is comparable to the wavelength. In the microwave region, this size is about 1 cm. Objects of this size are difficult to hold by radiation pressure. And small part of the beam energy falls on small objects in the microwave beam, and therefore the mechanical action on them is weak. So, in order to obtain fields, the magnitude of which is sufficient to operation objects, very large radiation powers are needed.

But in this range, thin vibrator wires can be used as targets. It was shown in [7-9] that the scattering, absorption and pressure of electromagnetic radiation on conducting fibers, the diameter of which is much smaller than the wavelength, are very large. Figure 1 shows the dependences of scattering (dashed line), absorption (thin solid line), and radiation pressure (thick solid line) on the thickness of the nickel wire at a radiation wavelength of 10 cm. The abscissa axis shows the values of the wire diameter in micrometers, the ordinate axis shows the values of the scattering efficiency factors Q_{sca} , absorption Q_{abs} , and radiation pressure Q_{pr} . These parameters are often used to characterize the interaction between electromagnetic radiation and objects [10, 11].

The force with which radiation presses on an object is determined by the formula:

[†] **Cite as:** M.G. Kokodii, V.O. Katrich, S.L. Berdnik, M.V. Nesterenko, V.O. Maslov, and I.O. Priz, East Eur. J. Phys. 3, 45 (2022), <https://doi.org/10.26565/2312-4334-2022-3-06>

© M.G. Kokodii, V.O. Katrich, S.L. Berdnik, M.V. Nesterenko, V.O. Maslov, I.O. Priz, 2022

$$F_{pr} = \frac{P}{c} Q_{pr} .$$

Here P is the power of the radiation that hit the object, c is the speed of light in the environment, Q_{pr} is the radiation pressure efficiency factor.

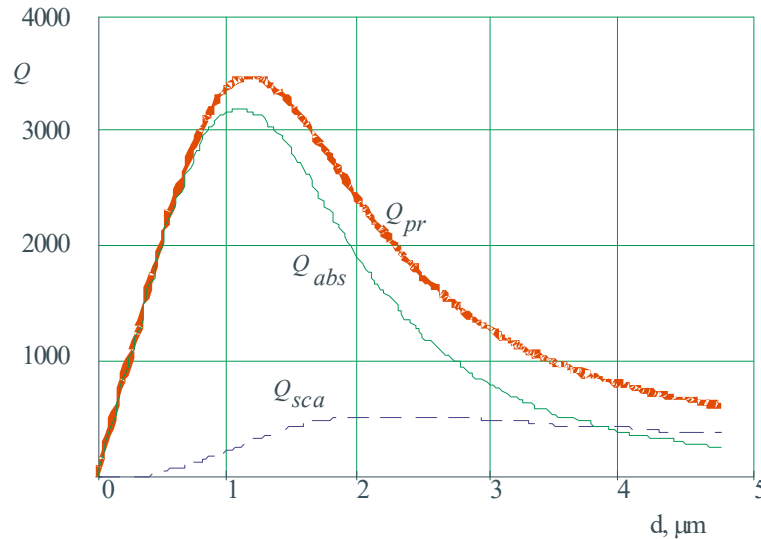


Figure 1. Efficiency factors of scattering, absorption, and radiation pressure on a thin metal wire

For a fully absorbent surface $Q_{pr} = 1$, for an absolutely reflective surface $Q_{pr} = 2$. Figure 1 shows that for a metal wire with a diameter of about 1 μm , the radiation pressure efficiency factor can reach very large values – up to several thousand. This can be used to levitate or move such objects in space.

Some new effects are observed in the interaction of electromagnetic radiation with vibrators of finite length. The pressure of a plane electromagnetic wave on a thin metal vibrator in free space was theoretically studied in [12]. When the length of the vibrator is close to half the wavelength of the radiation, resonance is observed, and the radiation pressure on this vibrator increases compared to the pressure on an infinitely long conductor. Radiation pressure efficiency factor increases with decreasing vibrator diameter.

The paper [13] describes an experiment on measuring the pressure of radiation with a wavelength of 8 mm on thin copper vibrators located in free space.

A vibrator in free space is subjected to a longitudinal force in the direction of propagation of the incident wave. If the vibrator is located in the waveguide, the configuration of the electric and magnetic fields near it is more complex than in free space. The direction and magnitude of the forces acting on it are different. Therefore, it is of interest to study such a case.

LINEAR VIBRATOR IN A RECTANGULAR WAVEGUIDE

The geometry of the problem is shown in Figure 2. A vibrator with a length of $2L$ is located in a rectangular waveguide perpendicular to the wide wall. The wave type is H10, a and b are the lengths of the wide and narrow walls. The electric field vector in the H10 wave is parallel to the vibrator axis, the magnetic field lines are perpendicular to it.

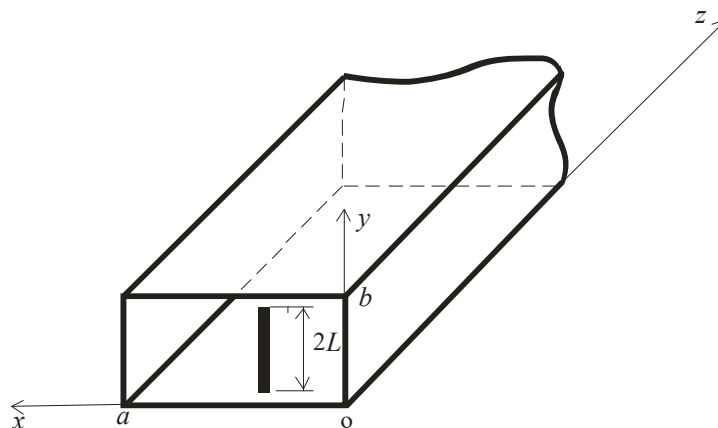


Figure 2. Vibrator in the waveguide

The fields in the waveguide are described by the following expressions:

$$\begin{aligned}
E_y &= E_0 \sin\left(\frac{\pi x}{a}\right) \exp(-ik_1 z), \\
H_x &= -\frac{E_0}{Z_c} \sin\left(\frac{\pi x}{a}\right) \exp(-ik_1 z), \quad H_z = i \frac{\lambda_w E_0}{\lambda_{kp} Z_c} \cos\left(\frac{\pi x}{a}\right) \exp(-ik_1 z). \\
k_1 &= \frac{2\pi}{\lambda}, \quad \lambda_w = \frac{\lambda}{\sqrt{1 - \left(\frac{\lambda}{\lambda_{kp}}\right)^2}}, \quad Z_c = \frac{Z_0}{\sqrt{1 - \left(\frac{\lambda}{\lambda_{kp}}\right)^2}}, \quad \lambda_c = 2a.
\end{aligned} \tag{1}$$

Here λ_w is the wavelength in the waveguide, λ_c is the critical wavelength.

The power of the wave propagating in the waveguide:

$$P_0 = \frac{1}{2} \operatorname{Re} \int_{S_0} E_y H_x^* dS = \frac{E_0^2}{4Z_c} ab. \tag{2}$$

Integration is performed over the cross-sectional area of the waveguide

The radiation intensity distribution along the x coordinate (wide wall of the waveguide) is as follows

$$I(x) = \frac{2P_0}{ab} \sin^2 \frac{\pi x}{a}. \tag{3}$$

The strength of the electric field in the middle of a wide wall is:

$$E_0 = \sqrt{\frac{4P_0 Z_c}{ab}}. \tag{4}$$

Along a narrow wall (the coordinate y) the intensity of the wave does not change.

Two magnetic field components, H_x and H_z , exist in the waveguide with the H_{10} wave. Therefore, there are two components of the force acting on the vibrator – F_z and F_x .

In a waveguide with a wave H_{10} :

$$\vec{F} = (\vec{J} \times \vec{B}) \cdot 2L = 2L\mu_0 \begin{vmatrix} \vec{i} & \vec{j} & \vec{k} \\ 0 & J_y & 0 \\ H_x & 0 & H_z \end{vmatrix} = 2L\mu_0 (\vec{i} J_y H_z - \vec{k} J_y H_x).$$

Force directed along the z-axis (longitudinal force):

$$F_z = -\frac{\mu_0}{2} \int_{-L}^L \operatorname{Re} \{ J_y(s) \cdot H_x^* \} ds, \tag{5}$$

Force directed along the x-axis (transverse force):

$$F_x = \frac{\mu_0}{2} \int_{-L}^L \operatorname{Re} \{ J_y(s) \cdot H_z^* \} ds \tag{6}$$

Electric current in the vibrator

The current in the vibrator is determined by the strength of the electric field in the wave incident on it, regardless of whether it is a plane wave in free space or an H_{10} wave in a waveguide. Therefore, to calculate the wave pressure on the vibrator in the waveguide, we will use the method of calculating the magnitude of the current in the vibrator, described in [12].

The current is determined by the following expression:

$$J(x, s) = \alpha \frac{i\omega E}{kk} \left\{ 1 - \cos \tilde{k}(s+L) - \frac{\sin \tilde{k}(s+L) + \alpha P^s(s)}{\sin 2\tilde{k}L + \alpha P^s(L)} (1 - \cos 2\tilde{k}L) \right\} \sin\left(\frac{\pi x}{a}\right). \tag{7}$$

It differs from the same expression in the work [12] by the factor $\sin(\pi x/a)$, which takes into account the change in the electric field strength along the wide wall of the waveguide.

Here:

$$P^s(s) = \int_{-L}^L \left[\frac{e^{-ikR(s', -L)}}{R(s', -L)} + \frac{e^{-ikR(s', L)}}{R(s', L)} \right] \sin \tilde{k}(s-s') ds',$$

$\alpha = \frac{1}{2 \ln \left[\frac{r}{r/(2L)} \right]}$ is the small parameter ($\alpha \ll 1$),

E is the electric field of the incident wave at the location of the vibrator,

$$R(s', s) = \sqrt{(s' - s)^2 + r^2},$$

$$\tilde{k}^2(s) = k_1^2 \left[1 + i\alpha\omega\varepsilon_1 z_i(s)/k_1^2 \right] = k_1^2 \left[1 + i2\alpha\bar{Z}_s(s)/(\mu_1 k r) \right]$$

$z_i(s)$ is the linear resistance, Ohm/m,

$$\bar{Z}_s(s) = 2\pi r z_i(s)/Z_0, \quad z_i = \frac{Z}{2\pi r}, \quad Z = \sqrt{\frac{\pi c \mu_0}{\sigma \lambda}} (1+i),$$

$Z_0 = \sqrt{\frac{\mu_0}{\varepsilon_0}} = 377$ Ohm is the wave impedance of free space, $k_1 = k\sqrt{\varepsilon_1\mu_1}$, $k = \frac{2\pi}{\lambda_w}$, ε_1 and μ_1 are the relative dielectric and magnetic permeability of the environment, λ_w is the wavelength in the waveguide, ω is the circular frequency. Values E , k , Z are taken for the medium in the waveguide, $\varepsilon_1 = 1$, $\mu_1 = 1$.

Expression (7) is valid for vibrators with a length less than λ . It is written in the Gaussian unit system.

Calculations were performed for the case when radiation with a frequency of 37.5 GHz propagates in a rectangular waveguide (the wavelength in free space is 8 mm). A thin copper vibrator is located in the waveguide perpendicular to the wide wall.

The standard size of the cross section of such waveguide is:

$$a = 7.2 \text{ mm}, b = 3.4 \text{ mm}.$$

The wavelength in the waveguide is 9.62 mm. Therefore, assuming that the largest length of the vibrator is 3 mm, we can evaluate its properties for the largest relative length $2L/\lambda_w = 0.312$.

In calculations, the transverse dimensions of the waveguide were taken as follows:

$$a = 7.2 \text{ mm}, b = 10 \text{ mm}.$$

Higher types of waves can arise in such waveguide. But if you take measures against the occurrence of these waves, then you can evaluate the effect of the main type of wave on a vibrator with a relative length of up to $2L/\lambda_w = 1$.

Figure 3 shows the distribution real and imaginary parts of the current along the vibrator by power 1 W. A copper vibrator with a diameter of 100 μm and a length of 3 mm is located perpendicular to the wide wall. The current value in amperes is shown for the case when the vibrator is located in the middle of a wide wall, at the maximum electric field.

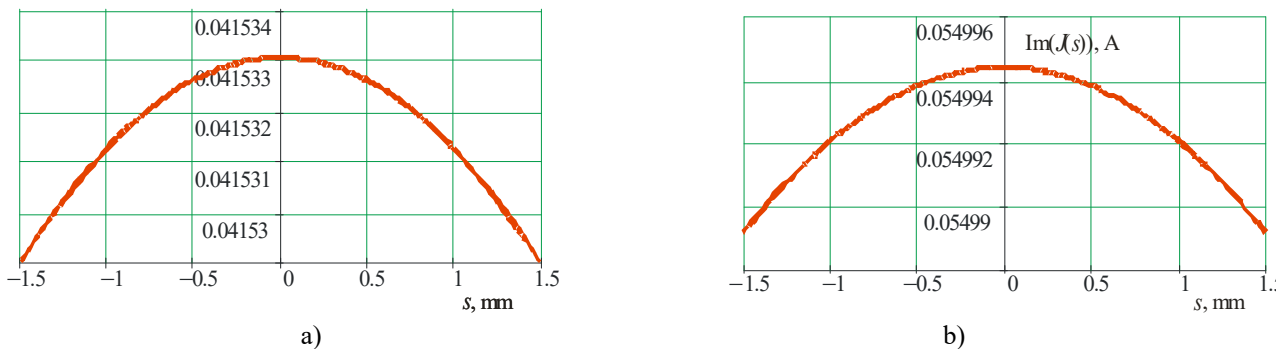


Figure 3. The vibrator current
a – real part, b – imaginary part

The current distribution is uneven, with a maximum in the center. But the current changes are very small - in the sixth place after the decimal point. The average value of the current along the length of the vibrator is

$$J_{cp} = 0.042 + 0.055i \text{ A}$$

This current almost 2 times less than the current in the same vibrator and the same electric field in free space, where it is equal

$$J_{cp} = 0.071 + 0.052i \text{ A}$$

Figure 4 shows the dependences of the real and imaginary parts of the current in the vibrator on its length. The real part of the current has a maximum when the length of the vibrator is close to half the wavelength of the radiation. The imaginary part changes sign near the point $2L/\lambda_w = 0.5$. The resistance of a short vibrator is inductive, while that of a long vibrator is capacitive.

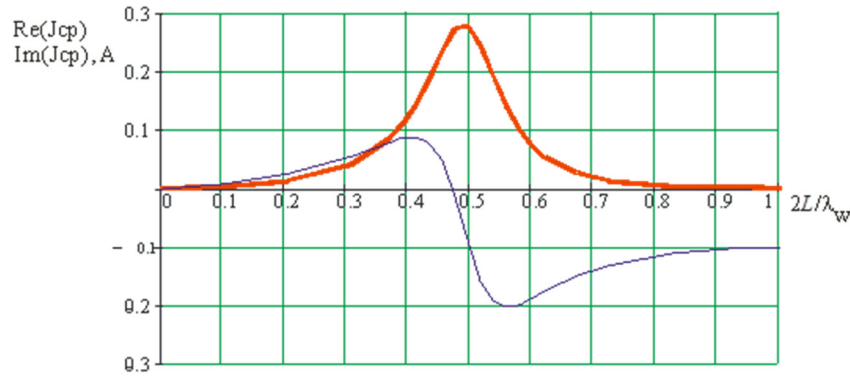


Figure 4. Dependence of the current in the vibrator on its length

Table 1 shows the current values in vibrators made of materials with different conductivity. Conductivity determines the value of the surface resistance Z , the thickness of the skin layer δ and current J .

Table 1. The dependence of the current in the vibrator on the conductivity of the material

Material	$\sigma, 1/(\text{Ohm}\cdot\text{m})$	$Z, \text{Ohm/square}$	$\delta, \mu\text{m}$	J, A
Copper	$5.88 \cdot 10^7$	$0.050 (1+i)$	0.34	$0.071+0.052i$
Nickel	$1.45 \cdot 10^7$	$0.103 (1+i)$	0.68	$0.077+0.057i$
Platinum	$9.52 \cdot 10^6$	$0.125 (1+i)$	0.84	$0.078+0.057i$
Graphite	$1.4 \cdot 10^5$	$1.028 (1+i)$	6.95	$0.080+0.053i$

It can be seen that the current is almost independent of conductivity, which differ by more than 400 times. This is explained by the fact that with a decrease in conductivity, the surface resistance increases, which makes it difficult for the current to flow. But the thickness of the skin layer increases, which facilitates its flow.

Longitudinal force acting on the vibrator

Substitution in formula (5) of expressions for current $J(s)$ and the components of the magnetic field H_x gives the following expression for the longitudinal component of the force acting on the vibrator:

$$F_z(x) = \frac{E_0 \lambda}{2c \lambda_w} \sin\left(\frac{\pi x}{a}\right) \int_{-L}^L \text{Re}\{J(s)\} ds . \tag{8}$$

The form of the formula is almost the same as for the force acting on the vibrator in free space [12]. The difference is in the presence of factors showing that the force depends on the x -coordinate and on the wavelength.

The current changes along the vibrator are very small. Therefore, the average value of the current can be used, so that formula (8) becomes:

$$F_z(x) = \frac{E_0 L \lambda}{c \lambda_w} \sin\left(\frac{\pi x}{a}\right) \text{Re}\{J_{cp}\} \tag{9}$$

Figure 5 shows the dependence of the force acting on the vibrator on its position in the waveguide. The calculations were made for a copper vibrator with diameter of 100 μm and length of 3 mm, located in waveguide with cross section of $7.2 \times 3.4 \text{ mm}^2$. The radiation wavelength in free space is 8 mm, the radiation power is 1 W.

Radiation pressure is the greatest when the vibrator is located in the middle of the wide wall of the waveguide, where the electric field strength is maximum, and it drops to zero near the narrow walls. The dependence of the force on the x coordinate is close to the $\sin^2 x$ function. The force is directed in the positive direction of the z -axis, in the direction of wave propagation.

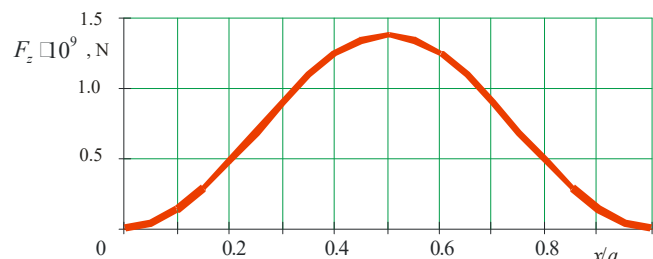


Figure 5. Dependence of the longitudinal force acting on the vibrator on its position in the waveguide

Figure 6 shows a graph of the efficiency factor of the radiation pressure on the vibrator as a function of its length. The vibrator is copper, its diameter is 100 μm . Curve 1 is shown for a vibrator in a waveguide with an H_{10} wave, which is located perpendicular to the wide wall in its middle, curve 2 is for the same vibrator in free space. Parameter $2L/\lambda_w$

plotted along the abscissa axis. In this parameter λ_w is the wavelength in the waveguide for curve 1, the wavelength in free space for curve 2. It is remarkable that the efficiency factor of the radiation pressure on the vibrator in the waveguide can be 2 times greater than on the vibrator in free space, and reach a value of 123. But for this, it is necessary that its length be approximately half the wavelength in the waveguide. Thus, at a radiation frequency of 37.5 GHz (the wavelength in free space is 8 mm, in the waveguide – 9.62 mm), the length of the vibrator should be 4.7 mm. This means that the length of the narrow wall of the waveguide must be at least 5 mm instead of the standard value of 3.4 mm.

The arrow on the abscissa shows the radiation pressure efficiency factor for a vibrator 3 mm long, which can be placed in a standard waveguide $7.2 \times 3.4 \text{ mm}^2$. It is equal to 18.2. This is much less than the maximum possible value. Therefore, it is advisable to use waveguides with non-standard cross-sectional dimensions, with a large vertical wall b to effectively use the radiation pressure.

The positions of the maxima of the radiation pressure efficiency factors on curves 1 and 2 do not coincide. For a vibrator in free space the maximum is at $2L/\lambda_w = 0.48$, for a vibrator in a waveguide it's located at $2L/\lambda_w = 0.49$.

The radiation pressure efficiency factor increases without limit, tending to infinity as the vibrator diameter decreases. However, this does not mean that the force acting on the vibrator increases, since the power of the radiation that hit the vibrator decreases in this case. The force acting on the vibrator decreases with a decrease in its diameter [12].

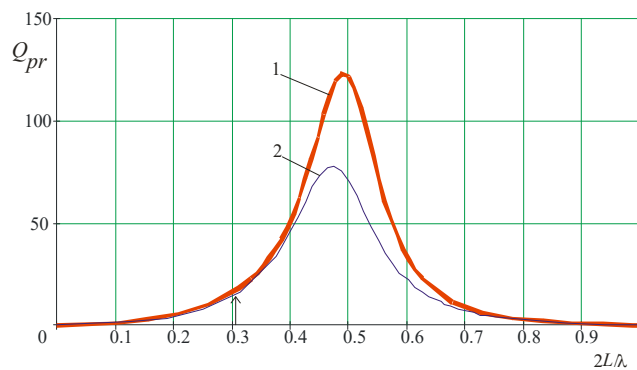


Figure 6. Dependence of the radiation pressure efficiency factor on the vibrator on its length
1 - vibrator in the waveguide, 2 - vibrator in free space

Transverse force acting on the vibrator

We use formula (6) in this case. Substituting into it the expression for the H_z component from formula (1), we obtain:

$$F_x(x) = \frac{E_0}{2c} \frac{\lambda}{\lambda_{kp}} \cos\left(\frac{\pi x}{a}\right) \int_{-L}^L \text{Im}\{J(s)\} ds. \tag{10}$$

Taking into account the small change in the current value along the vibrator, we can write:

$$F_x(x) = \frac{E_0 L}{c} \frac{\lambda}{\lambda_{kp}} \cos\left(\frac{\pi x}{a}\right) \text{Im}\{J_{cp}\}. \tag{11}$$

The results of calculations using this formula are shown in Figure 7. The transverse force is zero in the middle of the waveguide and near its walls. The force maxima are located at $x = a/4$ and $x = 3a/4$. The force is always directed towards the middle of the waveguide, i.e. the vibrator is drawn into the region of maximum field intensity.

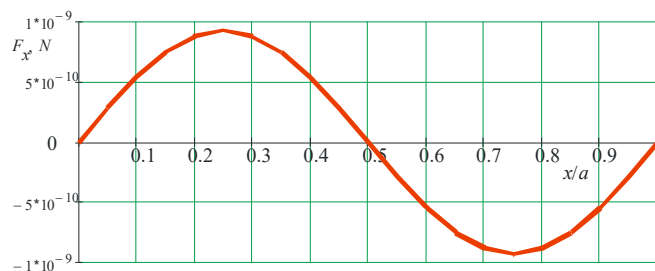


Figure 7. Dependence of the transverse force acting on the vibrator, on its position in the waveguide

Figure 8 shows the dependence of the transverse force on the length of the vibrator. The vibrator is located at the maximum of the magnetic field ($x = a/4$). The maximum force is located at $2L/\lambda_w = 0.41$. This value does not match

either the value for the longitudinal force in free space ($2L/\lambda_w = 0.48$), nor with the value for the longitudinal force in the waveguide ($2L/\lambda_w = 0.49$), although it does not differ much from them.

The force changes sign at $2L/\lambda_w = 0.475$: the longer vibrator is pushed out of the region of high field intensity. The maximum of buoyancy force is located at $2L/\lambda_w = 0.56$. It is approximately 3 times greater than the maximum of the positive force. Further, the force decreases in magnitude, but it does not reach zero at $2L/\lambda_w = 1$, as in the case of the longitudinal force.

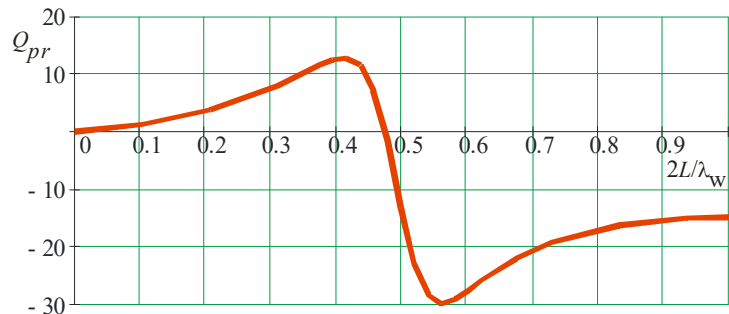


Figure 8. Dependence of the transverse force acting on the vibrator in the waveguide, on its length

Forces acting on the vibrator in waveguides of various sections

The forces acting on the vibrator in a waveguide with a cross section of $7.2 \times 3.4 \text{ mm}^2$ were calculated above. It is of interest to estimate the forces acting on a vibrator located in a waveguide with a different cross section at the same radiation power for wavelengths corresponding to the waveguide cross section. There are two factors here:

1. The radiation pressure efficiency factor Q_{pr} increases by increasing in the wavelength and the same vibrator diameter so the force acting on the vibrator increases [12].
2. At the same radiation power in a waveguide with a larger cross section, the radiation energy density decreases, so the force acting on the vibrator decreases.

We assume that the vibrator is made of copper, has a diameter of $100 \mu\text{m}$ and a length equal to the length of the short wall of the waveguide. Let's find the magnitude of the forces:

1. longitudinal force F_z acting on a vibrator located in the middle of a wide wall at the maximum radiation intensity;
2. transverse force F_x acting on a vibrator located at the maximum of the magnetic field H_z (for $x = a/4$ or $x = 3a/4$).

The power of radiation in the waveguide is equal $P_0 = 1 \text{ W}$. The results of calculations are shown in Table 2.

Table 2. Forces acting on a vibrator in a waveguide

Cross section of waveguide, mm^2	Wavelength, cm	Longitudinal force $F_z \cdot 10^{10}$, N	Transverse force $F_x \cdot 10^{10}$, N
7.2×3.4	0.8	26.8	9.59
23×10	3	6.68	6.55
28×12	3.5	6.74	6.14
	5	2.38	8.77
58×25	5.45	26.1	6.91
	10	2.00	6.91
	10.7	1.69	8.75
72×34	10	4.35	6.31

The forces in all waveguides are approximately the same, despite the large difference in the sizes of the latter. This is explained by the presence of counteracting factors mentioned above.

On the possibility of manipulations with targets in the form of thin vibrators in the microwave range

Let us evaluate the possibility of manipulations on thin vibrators using microwave radiation pressure: their displacement in space and levitation. Let us consider the case when the target is a copper vibrator, its diameter is $100 \mu\text{m}$ and a length of 3 mm . It is located in the waveguide with cross section of $7.2 \times 3.4 \text{ mm}^2$. Power of radiation is 1 W . Table 2 shows, that the longitudinal force acting on the vibrator is equal $26.8 \cdot 10^{-10} \text{ N}$, the transverse force is $9.59 \cdot 10^{-10} \text{ N}$.

The mass of this vibrator is $m = 1.65 \cdot 10^{-7} \text{ kg}$. The acceleration of the target is:

$$a = \frac{F}{m} = 0.0163 \text{ m/s}^2.$$

The target will move a distance of about 8 mm in 1 s , when it moves by this acceleration. This is quite a noticeable distance. It can be seen that microwave radiation pressure can be used to move millimeter-sized wire targets.

The radiation power required to keep such a target on the weight (levitation) can be estimated from the expression for the ponderomotive force






$$F = \frac{P}{c} Q_{pr}.$$

Force required for levitation is equal $F = mg = 1.62 \cdot 10^{-6}$ N. This is the weight of the target. The radiation pressure efficiency factor on a vibrator 3 mm long is $Q_{pr} = 18.2$. The power required for levitation is approximately 27 watts. This is a high power, but quite achievable in modern microwave technology.

CONCLUSION

1. A thin wire vibrator in the waveguide experiences radiation pressure.
2. There is a longitudinal component of the ponderomotive force directed towards the propagation of the wave and a transverse component directed towards the middle of the waveguide cross section.
3. The forces depend little on the conductivity of the vibrator material and the size of the waveguide cross section.
4. The magnitudes of the ponderomotive forces acting on thin metal vibrators are sufficient to control their position and move in space. Microwave radiation can be used to move such objects in space and keep them in a given place, similar to how it is done in the optical range using lasers.

ORCID IDs

-  Victor O. Katrich, <https://orcid.org/0000-0001-5429-6124>;
  Vyacheslav O. Maslov, <https://orcid.org/0000-0001-7743-7006>
 Mykola G. Kokodii, <https://orcid.org/0000-0003-1325-4563>;
  Sergey L. Berdnik, <https://orcid.org/0000-0002-0037-6935>
 Mikhail V. Nesterenko, <https://orcid.org/0000-0002-1297-9119>.

REFERENCES

- [1] A. Ashkin, Pressure of laser radiation, *Uspekhi fizicheskikh nauk*. **110**, 101-116 (1973).
- [2] S. Kawata, and T. Sugiura, "Movement of micrometer-sized particles in the evanescent field of a laser beam", *Opt. Lett.* **17**, 772 (1992). <https://doi.org/10.1364/OL.17.000772>
- [3] A. Pralle, M. Prummer, E.-L. Florin, E.H.K. Stelzer, and J.K.H. Hörber, "Three-Dimensional High-Resolution Particle Tracking for Optical Tweezers by Forward Scattered Light", *Microscopy research and technique*. **44**, 378 (1999). [https://doi.org/10.1002/\(SICI\)1097-0029\(19990301\)44:5%3C378::AID-JEMT10%3E3.0.CO;2-Z](https://doi.org/10.1002/(SICI)1097-0029(19990301)44:5%3C378::AID-JEMT10%3E3.0.CO;2-Z)
- [4] R.M. Simmons, J.T. Finer, S. Chu, and J.A. Spudich, "Quantitative measurements of force and displacement using an optical trap", *Biophysical Journal*. **70**, 1813 (1996). [https://doi.org/10.1016/S0006-3495\(96\)79746-1](https://doi.org/10.1016/S0006-3495(96)79746-1)
- [5] R.A. Valitov editor, *Ponderomotive action of electromagnetic field (theory and application)*, (Moscow, Sov. Radio, 1975). pp. 232 p. (in Russian).
- [6] V.G. Volostnikov, S.P. Kotova, N.N. Losevsky, and M.A. Rakhmatulin, "Manipulation of micro-objects using beams with non-zero orbital momentum", *Quantum Electronics*, **32**, 565 (2002). <https://doi.org/10.1070/QE2002v032n07ABEH002248>
- [7] V.M. Kuz'michev, N.G. Kokodiy, B.V. Safronov, and V.P. Balkasin, "Values of the absorption efficiency factor of a thin metal cylinder in the microwave band", *Journal of Communication Technology and Electronics*, **48**, 1240 (2003).
- [8] A. Akhmeteli, N. Kokodiy, B. Safronov, I. Priz, and A. Tarasevitch, "Efficient non-resonant absorption of electromagnetic radiation in thin cylindrical targets: Experimental evidence", *Proc. of SPIE*, **10185**, 101850I (2017). <https://www.scopus.com/record/display.uri?eid=2-s2.0-85022326725&origin=resultslist>
- [9] N.G. Kokodii, M.V. Kaydash, and V.A. Timaniuk, "Interaction of electromagnetic radiation with a thin metal wire in the case of a glancing incident wave", *Journal of Communication Technology and Electronics*, **62**, 205 (2017). <https://elibrary.ru/item.asp?id=28918056>
- [10] H.C. van de Hulst. *Light Scattering by Small Particles*. (NY, London, 1957). 536 p.
- [11] M. Kerker, *The scattering of light and other electromagnetic radiation*. (Academic Press, NY and London, 1969). pp. 671.
- [12] M.G. Kokodii, S.L. Berdnik, V.O. Katrich, M.V. Nesterenko, and M.V. Kaydash, Pressure of electromagnetic radiation on a linear vibrator, *East European Journal of Physics*, **4**, 172 (2021). <https://doi.org/10.26565/2312-4334-2021-4-23>
- [13] M. Kokodii, S. Berdnik, V. Katrich, M. Nesterenko, I. Priz, A. Natarova, V. Maslov, and K. Muntian, Measurement of microwave radiation pressure on thin metal fibers, *Ukrainian Metrological Journal*, **4**, 45 (2021), <https://doi.org/10.24027/2306-7039.4.2021.250413>

ТИСК ЕЛЕКТРОМАГНІТНОГО ВИПРОМІНЮВАННЯ НА ТОНКИЙ ЛІНІЙНИЙ ВІБРАТОР В ХВИЛЕВОДІ

М.Г. Кокодій, В.О. Катрич, С.Л. Бердник, М.В. Нестеренко, В.О. Маслов, І.О. Приз

Харківський національний університет імені В. Н. Каразіна, пл. Свободи, 4, 61022, Харків, Україна

Розв'язано задачу тиску електромагнітної хвилі на тонкий провідниковий вібратор у хвилеводі з модою H_{10} . Вібратор розташований перпендикулярно до широкої стінки хвилеводу. Розраховано силу струму у вібраторі, який виникає під дією електричного поля хвилі. Розподіл струму вздовж вібратора майже рівномірний. Струм у мікрохвильовому діапазоні мало залежить від провідності вібратора. У хвилі H_{10} існують дві складові магнітного поля - поздовжня і поперечна. При взаємодії цих компонентів зі струмом у виникають сили, які діють на вібратор поперек хвилеводу і вздовж нього. Величина поздовжньої сили найбільша, коли вібратор розташований посередині широкої стіни. Вона майже в 2 рази перевищує силу, яка діє на вібратор у вільному просторі при тій же середній інтенсивності випромінювання. Коли довжина вібратора близька до половини довжини хвилі випромінювання, сила максимальна. Поперечна сила виникає при взаємодії струму у вібраторі з поздовжньою складовою магнітного поля в хвилеводі. Вона максимальна, коли вібратор розташований на відстані $\frac{1}{4}$ довжини широкої стіни від її середини. Якщо довжина вібратора менше половини довжини хвилі випромінювання, сила спрямована в бік осі хвилеводу, інакше - у протилежний бік. Оцінена можливість використання тиску мікрохвильового випромінювання для створення мікромашин і управління положенням вібратора в просторі. Для цього потрібна потужність випромінювання в кілька ват.

Ключові слова: електромагнітна хвиля, провідниковий вібратор, тиск випромінювання, хвилевод, поздовжня сила, поперечна сила.